Succinate:Ubiquinone Oxidoreductase from *Paracoccus denitrificans* and Particulate Methane Monooxygenase from *Methylococcus capsulatus* (Bath): Experimental and Theoretical EPR Studies of the Metal Cofactors

Thesis by

Shao-Ching Hung

In Partial Fulfillment of the Requirements

For the Degree of

Doctor of Philosophy

California Institute of Technology

Pasadena, CA

2001

(Submitted September 1, 2000)

Acknowledgements

During my stay at Caltech, there are so many people to whom I owe thanks for their continued support and encouragement. Foremost among them is my advisor, **Sunney I. Chan**, without whose insights and intuition into biophysical chemistry, academic guidance, and encouragement, much of this thesis would not yet have reached completion. He also provided me a free environment to grow to be independent and made this learning experience here unforgettable.

I am grateful to the previous Chan group members, **Reggie Waldeck**, **Hung-Kay "Bruce" Lee**, and **Michael Stowell**, who worked on the SQR project, for their efforts, thoughts, and discussion on the project. For the pMMO project, **Sean Elliott** and **Hoa Nguyen**, who have worked on the project before me, are thanked for their contributions of ideas and many hours of hard labor they devoted to gain understanding to this problem. I also must acknowledge the support from the current Chan group members: **Tim Cheng**, **Kirk Hanson**, **Brian Schultz**, and **David Zhang**. Brian has been intellectually supportive for most of the projects that I have worked on. I must not forget to thank **Steve Yu** at Academia Sinica in Taiwan for his help and ideas in pMMO project. **Sigfried Musser**, **Silvia Cavagnero**, **Ron Rock**, and **Ruth Ann Bertsch** are all former group members from whom I have learned a lot in my early years in the Chan group.

The pulsed EPR experiments were conducted in collaboration with **David Britt**'s research group at UC Davis. I would like to thank **David Britt**, **Christ Grant** and **Jeff Peloquin** for their efforts on the pulsed EPR project. There are other collaborators to whom I would like to express my gratitude: **Doug Rees** and **Tina Iverson** for SQR

project, and **Huieh Min Chan**, **Wei Wang** for the spin-labeling project (not in the thesis). It has been a pleasure to collaborate with such talented people.

Besides work, friendship has been the most important thing in my life. Many friends have aided me in spirit during the past five years. **Hui-Ming Hung** and **Meina Xu** have been great roommates and friends through thick and thin. **Chuan-Cheng Chen** and **Hsi-I Yang** have been a constant source of support and inspiration. And for showing me not only the importance of glycoproteins but also the continuous encouragement through e-mail, I have to thank **Jennifer Liu**. **Eric Wei-Guang Diau** and his family are thanked for their love and gracious hospitality. **Ching-Tzu Chen** and **Rachel Chu** have made my last two years here more enjoyable by bring me troubles and sharing music while my old friends have all gone. **Chao-Ping Hsu**, **Peilin Chen**, **Catherine Kao**, **Richard P. Chang**, **Albert Wang**, and many other Taiwanese students have helped me during my early years here.

Finally, I would like to thank my family and my fiancé's family for their love and understanding. And of course, my fiancé, Tzu-Chi, deserves special thanks for sharing my highs and lows and providing moral support when needed.

Abstract

This thesis summarizes the application of conventional and modern electron paramagnetic resonance (EPR) techniques to establish proximity relationships between paramagnetic metal centers in metalloproteins and between metal centers and magnetic ligand nuclei in two important and timely membrane proteins: succinate:ubiquinone oxidoreductase (SQR) from *Paracoccus denitrificans* and particulate methane monooxygenase (pMMO) from *Methylococcus capsulatus*. Such proximity relationships are thought to be critical to the biological function and the associated biochemistry mediated by the metal centers in these proteins. A mechanistic understanding of biological function relies heavily on structure-function relationships and the knowledge of how molecular structure and electronic properties of the metal centers influence the reactivity in metalloenzymes. EPR spectroscopy has proven to be one of the most powerful techniques towards obtaining information about interactions between metal centers as well as defining ligand structures. SQR is an electron transport enzyme wherein the substrates, organic and metallic cofactors are held relatively far apart. Here, the proximity relationships of the metallic cofactors were studied through their weak spin-spin interactions by means of EPR power saturation and electron spin-lattice (T_1) measurements, when the enzyme was poised at designated reduction levels. Analysis of the electron T_1 measurements for the S-3 center when the *b*-heme is paramagnetic led to a detailed analysis of the dipolar interactions and distance determination between two interacting metal centers. Studies of ligand environment of the metal centers by electron spin echo envelope modulation (ESEEM) spectroscopy resulted in the identication of peptide nitrogens as coupled nuclei in the environment of the S-1 and S-3 centers.

Finally, an EPR model was developed to describe the ferromagnetically coupled trinuclear copper clusters in pMMO when the enzyme is oxidized. The Cu(II) ions in these clusters appear to be strongly exchange coupled, and the EPR is consistent with equilateral triangular arrangements of type 2 copper ions. These results offer the first glimpse of the magneto-structural correlations for a trinuclear copper cluster of this type, which, until the work on pMMO, has had no precedent in the metalloprotein literature. Such trinuclear copper clusters are even rare in synthetic models.

Table of Contents

Abbreviations and Nomenclature

A. m.	*Arum maculatum*
b-heme	Cytochrome *b*
cyt *c*	Cytochrome *c*
ENDOR	Electron-Nuclear Double Resonance
EPR	Electron Paramagnetic Resonance
ESE	Electron Spin Echo
ESEEM	Electron Spin Echo Envelop Modulation
EXAFS	Extended X-Ray Absorption Fine Structure
FAD	Flavin Adenine Dinucleotide
FP	Flavoprotein
FRD	Fumarate Reductase (Quinol:Fumarate Oxidoreductase)
FT	Fourier Transform
IP	Iron-sulfur Protein
P. d.	*Paracoccus denitrificans*
pMMO	Particulate Methane Monooxygenase
$Q_{2(6)(10)}$	Ubiquinone-2(6)(10)
QH_2	(Ubi)quinol
QFR	Quinol:Fumarate Oxidoreductase
QP	Quinone Polypeptides
SDH	Succinate Dehydrogenase
SDS-PAGE	Sodium Dodecyl Sulfate – Polyacrylamide Gel Electrophoresis
sMMO	Soluble Methane Monooxygenase
SQR	Succinate:Ubiquinone Oxidoreductase (Succinate:Ubiquinone Reductase)
S-1	2Fe-2S cluster
S-2	4Fe-4S cluster
S-3	3Fe-4S cluster
T_1	Electron Spin-lattice Relaxation Time Constant
T_2	Electron Spin-spin Relaxation Time Constant
TCA	Trichloro Acetic Acid
UQ	Ubiquinone-(10)
UQH_2	Ubiquinol
XAS	X-ray Absorption Spectroscopy

Chapter 1:

Introduction

Metal Ions in Proteins

In biological systems, transition metals play important roles both structurally and functionally. One of the characteristics of the transition elements is their ability to exist in multiple oxidation states. Therefore, they can participate readily in a multitude of functions, including electron transfer and oxidation/reduction of substrates. The electron-transfer reactions are responsible for biochemical energy transduction, maintenance of proton gradients, synthesis of cellular metabolites, and the initiation of chemical catalysis. Additionally, the transition elements are invariably present in biological systems as coordination complexes, with ligands ranging from cellular components such as H_2O, small organic molecules and porphyrins, to the side chains of amino acids. Often times, these complexes include open coordination sites, or ligand structures with labile sites. These features lead to versatile chemistry associated with the transition metals, including the binding of small molecule for signaling, ligand/substrate transfer reactions, and redox chemistry. As might be expected, the ligand structure/geometry modulates the redox potential of the metal center and the reactivity of the metal site.

Electron transfer metalloproteins — Electron transfer reactions occur in living organisms over a wide range of reduction potentials. In fact, different metal ions with different redox properties are available to living organisms. Iron and copper are among the most important metal ions used in redox metalloproteins. Iron is found in two main classes of electron transfer proteins, cytochromes and iron-sulfur proteins. Cytochromes all contain iron bound to a porphyrin (heme iron), and these are classified according to

the types of heme-protein linkage, the presence and absence of axial ligands, and the nature of the axial ligand(s). Cytochromes containing heme centers with both axial positions coordinated, as in cytochrome *c* and cytochrome b_5, are usually involved in electron transfer.[1] Iron-sulfur proteins are poly-metallic systems in which the iron ions contain cysteine sulfurs and inorganic sulfide ions as ligands, and they can assume variable oxidation states.[2] These systems are classified according to the number of iron atoms and the number and type of sulfur atoms in the "cluster." Several types of iron-sulfur clusters have been distinguished: $[Fe(S\text{-}cys)_4]^{1-/2-}$ (Fe-0S), $[Fe_2S_2(S\text{-}cys)_4]^{2-/3-}$ (2Fe-2S), $[Fe_3S_4(S\text{-}cys)_4]^{2-/3-}$ (3Fe-4S), and $[Fe_4S_4(S\text{-}cys)_4]^{2-/3-}$ or $[Fe_4S_4(S\text{-}cys)_4]^{1-/2-}$ (4Fe-4S). The class of [4Fe-4S] ferredoxins are usually further subdivided into low- and high-potential ferredoxins, with $[Fe_4S_4(S\text{-}cys)_4]^{1-/2-}$ and $[Fe_4S_4(S\text{-}cys)_4]^{2-/3-}$ as the associated redox couples, respectively.[3,4] Cytochromes and iron-sulfur clusters exhibit a wide range of redox potentials in biological systems. It is generally believed that the redox properties of the heme iron in cytochromes and the iron(s) in iron-sulfur clusters in proteins are modulated by the details of the coordination sphere and the protein matrix.[5,6] Because there is usually minimal structural reorganization about the iron center in six-coordinated hemes and the iron atoms in iron-sulfur clusters, the reorganization energy for electron input/output is typically low and electron input and output involving these iron centers is facile.

Copper is also found in many metalloproteins with different functions. When involved in electron transfer processes, it is found almost exclusively in the form of blue copper sites (type 1 copper).[7,8] Unlike the normal copper center (type 2 copper), which exhibits normal tetragonal geometry of cupric complexes, type 1 copper center has a

distorted tetrahedral structure with a thiolate sulfur of cysteine, a thioether sulfur of methionine, and two fairly normal histidine N as ligands to the copper ion. The intense blue color arises from a S(cys) → Cu(II) charge transfer transition at 600 nm.[9] Because all blue proteins share essentially the same coordination sphere, their redox potentials span a range of slightly over 150 mV.[7] The blue copper site is unique in that the coordination geometry remains essentially unaltered between Cu(II) and Cu(I). This feature of the blue copper site ensures a low reorganization energy for electron input or electron output between the Cu(II) and Cu(I) states. Over the years, detailed experimental characterization and theoretical description of the ground state of the blue copper center have provided fundamental insight into the electronic structure of the site and the role of this electron structure on the long-range electron transfer reactivity exhibited by the blue copper proteins.[9]

Metalloenzymes — Metalloenzymes are metal-containing proteins that partake in chemical catalysis. The metal center in a metalloenzyme does not necessarily have to undergo redox transition as part of the catalytic reaction. Examples of such a metal site or metalloenzyme include the zinc ion in carbonic anhydrase[10] or carboxypeptidase.[11] The zinc ion in these enzymes activates a bound nucleophile (substrate) to facilitate certain bond cleavage, bond arrangements, or hydrolysis of the substrate. However, the transition metal at the active site often combines the capability to exist in multiple oxidation states with the ability to coordinate certain nucleophiles. In these systems, one oxidation state of the transition metal is inert to the nucleophile of interest, whereas the other is active in promoting chemical catalysis. A multitude of Fe- and Cu- containing

proteins rely on its propensity toward facile one- or two- electron changes to mediate redox-catalysis. In the case of iron, either heme iron or non-heme iron (mono- or di-nuclear) has been found at the active site. Examples include the heme center in cytochrome P450[12] or the heme a_3 site in cytochrome *c* oxidase[13,14] and the non-heme dinuclear oxo-iron cluster in soluble methane monooxygenase[15] and ribonucleotide reductase.[16]

The copper centers at the active sites of copper proteins have historically been divided into three classes: type 1 or blue copper (involved mainly in electron transfer), type 2 or normal copper, and type 3 or coupled binuclear-copper centers.[9] In recent years, this list has been expanded to include the dithiolato-bridged mixed valent Cu(I)-Cu(II) center found in cytochrome c oxidase (Cu_A)[17,18] and nitrous oxide reductase (Cu_Z);[19] and the trinuclear copper clusters (comprised of a type 2 and a type 3 center) found in ascorbate oxidase and laccase.[20-22] More recently, a ferromagnetically coupled trinuclear copper cluster has been proposed to be involved at the active site of the pMMO.[23,24] Type 2 copper centers are found in Cu/Zn superoxide dismutase and in various oxidases and monooxygenase,[25] where the reduced copper sites react with dioxygen to either reduce it to hydroperoxide or activate it for the hydroxylation of substrate. The dioxygen binding site of cytochrome c oxidase comprises a Cu_B-$heme_A$ coupled site wherein the Cu_B is a type 2 copper center.[26] Hemocyanin and tyrosinase contain a coupled binuclear, type 3 copper center. Both enzymes bind dioxygen, but tyrosinase, as a monooxygenase, activates this ligand for hydroxylation of phenolic substrates.[27] Laccase, ascorbate oxidase, and ceruloplasmin consist of a combination of type 1, type 2, and an antiferromagnetically coupled type 3 centers. As mentioned

earlier, the type 2 and type 3 centers form a trinuclear copper cluster in these enzymes, as now proven by crystallography.[22,28] These oxidases couple the four one-electron oxidations of substrate(s) to the four electron reduction of dioxygen to water. The trinuclear copper cluster(s) of pMMO is thought to contain a somewhat different type of trinuclear copper cluster involved in the activation of dioxygen and hydroxylation of methane.[23,24]

The Metalloenzymes of This Thesis

In this thesis, we focus on two membrane proteins: succinate:ubiquinone oxidoreductase (SQR) from *Paracoccus denitrificans* and the particulate methane monooxygenase (pMMO) from *Methylococcus capsulatus*. SQR catalyzes the oxidation of succinate to fumarate in the electron transport of higher organisms, and the reducing equivalents resulting from the two-electron oxidation are transferred to a ubiquinone to convert the latter to a quinol.[29,30] Aside from a flavin and several iron-sulfur clusters, it has been suggested that a cytochrome (*b*-heme) is involved in the shuttling of electrons across the protein.[30] The pMMO mediates the hydroxylation of methane to methanol in methanotrophic bacteria. This is a multi-copper enzyme containing five trinuclear copper clusters. The 15 copper ions could be differentiated into two groups according to their reactivity with the substrate dioxygen.[23,24,31] Two of the trinuclear copper clusters are involved in dioxygen chemistry and alkane hydroxylation, and have been termed catalytic clusters or C-clusters. The other clusters are thought to provide a buffer of reducing equivalents for ultimate transfer to the C-clusters. Accordingly, they are involved in electron transfer, and have been referred to as electron-transfer clusters or E-

clusters. As mentioned earlier, these multinuclear copper clusters are unlike other multinuclear copper centers found in metallobiochemistry.

Electron Paramagnetic Resonance (EPR): A Spectroscopic Tool to Probe Ligand Structure and Metal-metal Interactions of Metal Ions in Proteins

The wealth of spectroscopic properties associated with transition metals is important in shedding light on the nature of the metal sites in proteins. Electron paramagnetic resonance (EPR) offers tremendous advantages when the method is employed toward the elucidation of chemical binding and structure. Not only is the EPR spectrum of the paramagnetic transition metal a fingerprint of its identity and its electronic structure, fine structures in the spectrum can also offer important information about its immediate atomic neighbors and environment (eq 1).

The EPR spectrum of a single paramagnetic spin system (S) in a metalloprotein is often described by a spin Hamiltonian of the form

$$H = \beta_e \mathbf{B}\cdot\mathbf{g}\cdot\mathbf{S} + \sum_n \mathbf{S}\cdot\mathbf{A}_n\cdot\mathbf{I}_n + D[S_z^2 - \tfrac{1}{3}S(S+I)] + E(S_x^2 - S_y^2)\,. \qquad (1)$$

It consists of the electron Zeeman interaction, nuclear hyperfine and superhyperfine interactions, and the zero-field splitting. $\mathbf{A}_n$ is the hyperfine or superhyperfine tensor of the n-th nucleus, arising from the magnetic interaction(s) between the paramagnetic transition metal and its magnetic nuclei (hyperfine interaction) and the surrounding ligand nuclei (superhyperfine interaction). The last two terms give rise to the zero-field splitting, which is absent for $S = 1/2$. The zero-field splitting arises from the spin orbit

interactions within a $S > 1/2$ spin system as well as magnetic interactions among spins that might be localized on different centers. Thus the EPR signal reflects the nature of the transition metal and the number of unpaired electron spins (electronic structure) as well as the ligand-structure of the metal site.

For EPR to be a useful structural tool, it is necessary to have access to the information on the interaction(s) between paramagnetic centers within a metalloprotein as well as the superhyperfine interactions between the paramagnetic center(s) and the ligands. The interactions between paramagnetic centers could be weak or strong. When the paramagnetic centers are dispersed within the protein, these interactions are typically weak. However, they become strong when the transition metals become part of a cluster. In contrast, superhyperfine interactions are typically quite weak, and these spectral details are often masked by the inhomogeneous broadening, particularly in the spectra of paramagnetic centers in frozen solution. Under these conditions, even the desired information on the hyperfine interaction(s) between the unpaired electron(s) and the magnetic nuclei of the transition metal can only be obtained when the hyperfine splittings are large compared to the inhomogeneous linewidth.

Two different methods have been developed over the years to improve our ability to measure weak hyperfine and superhyperfine interactions: electron-nuclear double resonance (ENDOR)[32] and electron spin echo envelope modulation (ESEEM) spectroscopy.[33] The ENDOR spectrum corresponds to the spectrum of the nuclear transitions in a paramagnetic center. However, the continuous-wave (CW) ENDOR signal intensity is only ~1% of the intensity of the associated EPR signal. Nevertheless, the ENDOR method offers one of the most powerful approaches to discern hyperfine

interactions associated with a transition metal as well as superhyperfine interactions associated with ^{1}H and strongly coupled ^{14}N's. On the other hand, in ESEEM, one observes the EPR in the time-domain by pulse methods, and any unresolved structure of the EPR signal resulting from weak superhyperfine interactions with surrounding nuclei manifests itself as a modulation of the echo envelope. The modulation frequencies are related to nuclear transition frequencies, and it is relatively straightforward to analyze these data to yield the desired hyperfine interactions. Since the experiment involves the detection of the electron spin echo (ESE) signal amplitude modulation, the sensitivity is relatively improved over the ENDOR experiment.

In multicentered metalloproteins, the distances between adjacent metal centers represent important structural information. For example, these distances, which might range from 3 – 20 Å, often determine the rate of electron transfer between centers, other factors being equal. Accordingly, the interactions among the various metal centers are always crucial to the function of the protein. The electron spin-spin interactions between neighboring paramagnetic centers can also be detected through EPR spectroscopy.[34,35] Both exchange coupling and dipole-dipole interactions contribute to spin-spin effects that can have profound effects on the EPR spectrum. Exchange couplings are normally electrostatic and operate through chemical bonds (especially for shorter inter-center distances). On the other hand, dipole-dipole interactions are magnetic in character and operate through space. Though these interactions are only significant when the distances between the paramagnetic ions are very short, when exchange coupling dominates, the effects on the spectrum are profound and are capable of providing explicit information about the strength and type of interaction between the centers. However, even when the

interacting spins are relatively far apart, say 10 Å or more, they can influence each other. For example, the interaction with a faster-relaxing spin can enhance the relaxation of a slower relaxing spin, and the interaction between the two spins could lead to a decreased tendency toward microwave power saturation or an increase in resonance width for the slowly relaxing spin. Both the exchange and magnetic dipole-dipole interactions could contribute to the relaxation behavior of the slowly relaxing spin, and of course, the dipole-dipole interaction can provide distance information. Thus, through detailed analysis of the EPR spectra of the interacting paramagnetic transition metal centers and their relaxation behaviors, structural information could be deduced regarding the interacting paramagnetic pairs.

Applications of EPR to Two Interesting and Important Enzyme Systems

Succinate: Ubiquinone Oxidoreductase (SQR) — SQR participates in the tricarboxylic acid (TCA) cycle in cellular metabolism and in the respiratory chain as Complex II. These two processes are involved in the generation of large amount of energy released in the catabolism of glucose. SQR catalyzes the oxidation succinate to fumarate and transfers the electrons from succinate to membrane bound ubiquinones (UQ), according to eq 2:

$$\text{succinate} + \text{UQ} \rightarrow \text{fumarate} + \text{UQH}_2. \qquad (2)$$

The resulting ubiquinol (UQH_2) then serves as an electron donor to the Complex III (cytochrome bc_1) in the respiratory chain. As expected from the relatively small ΔE_m

that exists between the fumarate/succinate couple (E_{m7} = +10 mV) and the UQ/UQH_2 couple (E_{m7} = +60 mV), the electron flow through Complex II from succinate to ubiquinone is not linked to proton pumping. Nevertheless, SQR does serve as a regulatory site of the TCA cycle and an entry point for reducing equivalents into the respiratory chain.

The mammalian SQR (and the SQR from *Paracoccus denitrificans* in this study) consists of 4 subunits. The flavoprotein (FP) contains the substrate (dicarboxylate) binding site and a covalently bound flavin moiety (FAD); the iron-sulfur protein (IP) houses three iron-sulfur clusters of type 2Fe-2S, 4Fe-4S, and 3Fe-4S, often referred to as S-1, S-2, and S-3, respectively. Together, the FP and IP subunits form the soluble domain, which constitutes the succinate dehydrogenase activity (SDH) of the complex. This soluble domain is anchored to the plasma membrane by two hydrophobic polypeptides (QP); for reviews see ref. 30,36-38. The QP binds one molecule of *b*-heme[39-41] that may confer reactivity to two bound UQ's.[41,42] Despite extensive efforts, the electron-transfer pathway and the mechanism of UQ reduction in SQR remain controversial. Particularly, both the S-2 center and the *b*-heme exhibit redox potentials much lower than those of fumarate and ubiquinone. Therefore, their involvement in the electron transfer mechanism has been questioned.

Towards addressing these issues, we have studied the SQR from *Paracoccus denitrificans* (*P. d.*). SQR from *P. d.* appears to be the closest bacterial homologue to the mammalian SQR.[43,44] The objectives of the study are to map out the proximity relationships between the various cofactors in the protein, and ultimately to clarify the flow of electrons through the enzyme during turnover. To accomplish this goal, it is

necessary to prepare the enzyme in different protein states wherein selected metal centers are rendered paramagnetic and/or different radical species are elicited from the organic cofactors. Specifically, we need to prepare protein states in which different pairs of cofactors are paramagnetic. We can then apply the methods of electron spin-spin interactions to probe proximity relationships between different pairs of cofactors within the enzyme. It turns out that EPR spectroscopic "signatures" associated with the flavin radical, the three iron-sulfur cluster (the S-1, S-2, and S-3 centers), the *b*-heme, and the protein-bound ubisemiquinone radicals (Q•) could be obtained under various levels of reduction of the protein by oxidizing the enzyme in air, oxidizing the enzyme in the presence of ferricyanide, incubating the enzyme with different levels of succinate, and reducing the enzyme in dithionite. However, it is necessary to understand the nature of the EPR signal associated with each metal center as well as the various organic radicals before the work could move forward.

Radical signals were cleanly detected in the succinate-reduced preparation at 170 K, where the signals from other metal centers were readily broadened beyond detection. Based on spectral simulation, the spectrum is attributed to a flavin radical superimposed with two bound Q•'s. The number of stabilized Q•'s bound to the protein may shed some insight into the chemistry of the quinone reduction.

To probe the metal-metal interactions, we have undertaken EPR power saturation experiments of the S-1 and S-3 centers at different redox poised preparations. In the air-oxidized sample, only the S-3 center and the *b*-heme are EPR-active. The power saturation data of the S-3 center provided evidence for enhanced spin relaxation of the S-3 center, which is indicative of a weakly magnetic dipole-dipole interaction between the

S-3 center and *b*-heme. When the enzyme is incubated with excess succinate, the S-3 center is reduced and becomes an S = 2 state; the S-1 center is also reduced and becomes EPR active. Upon dithionite reduction, the *b*-heme becomes reduced to a diamagnetic ferro-heme, and the S-2 center is also reduced to yield a paramagnetic species with rather weak signals. Power saturation experiments of the reduced S-3 center and the reduced S-1 center in the above succinate- and dithionite-reduced forms of the protein revealed weak couplings of the S-2 center to both the S-1 and S-3 centers. Thus, these experiments yielded a rough topological picture of the geometric disposition of these metal centers in the protein.

Since microwave power saturation reflects the contribution of both the electron spin-lattice relaxation and spin-spin relaxation rates on an electron spin system, it is difficult to quantify the observations in terms of a distance between spin centers. The dipolar and exchange interactions contribute differently to these two relaxation rates. On the other hand, it is possible under favorable circumstances to obtain a distance between two interacting spins by exploiting the effect of dipole-dipole and exchange interactions of a rapidly relaxing electron spin on the electron spin-lattice relaxation rate of the more slowly relaxing paramagnetic center. Accordingly, we have resorted to pulse EPR methods to measure the effect of the *b*-heme on the electron spin-lattice relaxation rate of the S-3 center. In the air-oxidized preparation, the S-3 center and *b*-heme form the only magnetically interacting pair, and thus this system provided an unique opportunity for the application of this approach to obtain a detailed analysis of the proximity relationship between these two centers.

Finally, structural information about the environment of the reduced S-1 center,

the oxidized S-3 center, and the flavin radical in the purified SQR was investigated by ESEEM. A program based on the density matrix formalism of Mims was used to fit the ESEEM data.[45] This study provided a reliable determination of the nitrogen hyperfine and quadrupole coupling parameters. The complicated ESEEM signals observed for the flavin radical were simulated and attributed to the interactions of nitrogens of the flavin isoalloxazine ring with the electron spin. In the case of both S-1 and S-3 centers, the spectral features and modulation depths were accounted for by a coupled peptide-nitrogen nucleus. Armed with the latter results, the protein environments surrounding the S-1 and S-3 centers are discussed in terms of the recent reported structure of homologous enzymes, quinol:fumarate oxidoreductase (QFR or fumarate reductase (FRD)) from *E. coli*[46] and *Wolinella succinogenes*.[47] We conclude that the modulation of the redox potentials of the iron-sulfur clusters by protein matrix plays an important role in determining the direction of electron flow.

Particulate Methane Monooxygenase (pMMO) — The selective alkane activation is a difficult chemical process, which has been a challenge to the synthetic chemist for many years. However, the enzyme methane monooxygenase found in methanotrophic bacteria catalyzes the conversion of methane to methanol at ambient temperatures and pressures.[48]

$$CH_4 + O_2 + H^+ + NADH \rightarrow CH_3OH + H_2O + NAD^+ \qquad (3)$$

Bacterial methane oxidation plays a significant role in the global carbon cycle. In

addition, the unique metabolism of the methanotrophs offers a powerful approach to environmental biodegradation[49-51] as well as industrial selective hydroxylation reactions.[52]

This enzyme exists in two distinct forms, a soluble (cytoplasmic) enzyme (sMMO) and particulate (membrane-bound) enzyme (pMMO). While the sMMO has been extensively investigated and the hydroxylase has been shown to contain a non-heme binuclear iron(II) active site,[15,53] the pMMO has proved to be difficult to handle due to the lability of the enzyme activity *in vitro.* Unlike the sMMO, pMMO is a membrane protein and hence difficult to purify. Recently, the Chan laboratory has successfully purified the pMMO to homogeneity and has shown that it is a copper protein. A total of 15 copper ions are known to be associated with the enzyme, and these copper ions appear to be arranged into 5 trinuclear copper clusters.[23,24,54]

The functional form of the pMMO appears to be the fully reduced protein. As isolated in air, many of the copper ions remain reduced. No more than 50% of the copper ions are oxidized to Cu(II). However, all 15 copper ions could be oxidized by incubation of the enzyme with ferricyanide. Magnetic susceptibility and electron paramagnetic resonance (EPR) studies of the fully oxidized enzymes suggested that the copper ions of the protein were best described as a series of ferromagnetically coupled trinuclear copper clusters with $J \approx 20\ cm^{-1}$ and $D \leq 0.05\ cm^{-1}$.[23]

Based on the reactivity of the copper ions with dioxygen and ferricyanide as oxidants, the copper ions in pMMO have been differentiated into two subsets.[24] Using both EPR spectroscopy and x-ray absorption edge spectroscopy, it has been conclusively determined that a subset of ~6 copper ions (out of ~15) can be oxidized by dioxygen,

and but all 15 copper ions could be oxidized after the pMMO has been treated with millimolar concentrations of ferricyanide. This has led to the proposal that the copper ions are grouped into catalytically active clusters (C-clusters) and those involved in electron-transfer chemistry (E-clusters). Direct evidence in support of copper ions at the active site has recently been provided by extended X-ray Absorption Fine Structure (EXAFS) in conjunction with acetylene suicide substrate modification experiments.[31]

Clearly, the large number of copper ions within the protein severely complicates the interpretation of the spectroscopic data on the copper clusters. To begin with, in the resting state, the copper ions are reduced and reveal no spectroscopic signatures in the uv-visible and EPR spectrum. These copper ions are not spectroscopically accessible except by x-ray spectroscopy. A characteristic EPR is observed when the clusters are oxidized, but the spectrum must necessarily be heterogeneous due to variability in the electronic structure as well as ligand structure from cluster to cluster and dispersion in the spin Hamiltonian parameters for the five clusters. Accordingly, it has been difficult to associate a spectroscopic feature with a specific cluster.

Recently, Sean Elliott of the Chan laboratory undertook a series of chemical modifications and proteolytic treatments of pMMO in an attempt to distinguish between the various copper sites of the enzyme.[31] These experiments showed that the 9 copper ions associated with the E-clusters are associated with the water-soluble exposed domains of the 45 kDa subunit. The remaining 6 copper ions remain membrane-bound and are deeply buried in the 27 kDa transmembrane domain of pMMO. The results also suggested that the C-clusters exhibit a nearly isotropic EPR signal centered near $g = 2.1$, the same EPR signal that is associated with dioxygen chemistry and methane turnover.

Unlike the metal centers in SQR, which are held at relatively long distances from one another, the copper ions in the active site of pMMO exhibit strong exchange coupling with each other within the cluster. As mentioned earlier, when the exchange interactions exist among the electron spins, the exchange interaction can have a profound effect on the EPR spectrum, and in principle, EPR is capable of providing some structural information on the cluster(s). For example, in the present case, all indications are that the copper ions are ferromagnetically coupled to one another when they are oxidized. Ferromagnetically coupled trinuclear Cu(II) clusters are unprecedented in metalloenzymes, and such clusters are even few and far between in the inorganic chemistry literature. Accordingly, we have undertaken a survey of triangular model Cu(II) complexes with defined structural and ligand information, in the hopes that this analysis will provide some insights into the nature of the trinuclear copper clusters in pMMO. Based on these insights, we have carried out EPR spectral simulations of the pMMO cluster signal based on the structural information of the ferromagnetic model complexes. It is possible to simulate the EPR signal observed for the C-cluster of pMMO only with proper g-tensors and relative orientations between them. Moreover, certain magneto-structural correlations were derived based on ferromagnetically coupled trinuclear copper clusters.

Outline of the Thesis

Metalloproteins play important functions in biological systems. Within a multicentered metalloprotein, there are often interactions among neighboring metal sites, and these interactions are often critical to biological activity. This dissertation

summarizes the applications of EPR spectroscopy to elucidate interactions and proximity relationships between adjacent metal centers in two important and timely membrane proteins: succinate:ubiquinone oxidoreductase from *Paracoccus denitrificans* and the particulate methane monooxygenase from *Methylococcus capsulatus.*

The use of redox poising to control redox states in SQR and to ascertain proximity relationships — Chapter 2 summarizes the EPR spectroscopic signatures of the metal centers, flavin, and protein-bound ubisemiquinone radicals in SQR from *Paracoccus denitrificans* (*P. d.*) under various redox levels. Based on the spectroscopic characterizations of these metal centers, the paramagnetism for different metal sites can be controlled (on or off) when the protein is poised in a designated redox potential. The proximity relationships between these metal centers were then explored through their relaxation behaviors by means of EPR power-saturation measurements. A number of weak couplings between the metal centers were discerned, and from these results, a rough topology of the geometrical disposition of these metal centers has emerged. This work has provided the first clear evidence of a close proximity between the S-3 center in the hydrophilic domain and the *b*-heme in the membrane domain.

The use of T_1 to measure the distance between the S-3 center and the b-heme in SQR — Chapter 3 describes an elaborated method for distance determination between two coupled metal centers, namely, the S-3 center and the *b*-heme, based on their magnetic dipole-dipole interaction. Here, pulse EPR experiments (inversion recovery and "picket-fence" pulse sequences) were performed to determine the electron spin-

lattice relaxation rate constant (T_1) for the S-3 center over a range of temperatures. A detailed analysis of the components in the electron spin-lattice relaxation of the S-3 center led to a lower limit of the distance between the S-3 center and the b-heme as well as the intrinsic relaxation mechanism of the S-3 center. The implications of these results toward the role of the *b*-heme in the electron transfer pathway in SQR are discussed.

The use of ESEEM to probe ligand environments around the metal centers in SQR — Chapter 4 deals with the interactions between the unpaired electron spins (from paramagnetic metal centers or the flavin radical) and surrounding nuclear spins. ESEEM spectroscopy was employed to ascertain the ligand environment of certain EPR-active metal centers in SQR. Based on spectral simulations of the ESEEM data for the reduced S-1 center and the oxidized S-3 center, and the nitrogen quadrupolar coupling constants deduced, these metal centers are coupled to only peptide nitrogens. These ligand environments are then discussed in light of the recently reported crystal structure data on quinol:fumarate oxidoreductase (QFR or fumarate reductase (FRD)) from *E. coli* and *Wolinella succinogenes*, particularly, the chemistry of the electron transfer in these systems. Finally, the more complicated ESEEM data from the flavin radical were also analyzed in the same fashion.

The ferromagnetically coupled trinuclear Cu(II)clusters in pMMO — In Chapter 5, we consider the interactions between electron spins under the circumstance when the distances between unpaired spins are really short such that the exchange interactions become important. The profound effect of the exchange interaction on the EPR

spectrum of these clusters will be examined. As expected, the observed EPR signal is different from that of the individual Cu(II) ions. We were successful in simulating the EPR spectrum observed for the C-clusters and E-clusters in pMMO. These clusters exhibit distinctive EPR signals and the spectra could be rationalized in terms of ferromagnetically coupled equilateral trinuclear clusters. This work is novel inasmuch as there is no precedent for these trinuclear copper clusters in metalloproteins.

References

(1)Hoffman, B. M.; Natan, M. J.; Nocek, J. M.; Walin, S. A. *Struct. Bonding* **1991**, *75*, 85.

(2)Cammack, R.; Sykes, A. G. *Iron sulfur proteins*; Academic Press: San Diego, 1992.

(3)Carter, C. W., Jr.; Kraut, J.; Freer, S. T.; Alden, R. A.; Sieker, L. C.; Adman, E.; Jensen, L. H. *Proc. Natl. Acad. Sci. U. S. A.* **1972**, *69*, 3526.

(4)DePamphilis, B. V.; Averill, B. A.; Herskovitz, T.; Que, L., Jr.; Holm, R. H. *J. Am. Chem. Soc.* **1974**, *96*, 4159.

(5)Louro, R. O.; Catarino, T.; Salgueiro, C. A.; LeGall, J.; Xavier, A. V. *JBIC* **1996**, *1*, 34.

(6)Cammack, R. *Adv. Inorg. Chem.* **1992**, *38*, 281.

(7)Solomon, E. I. *Copper proteins*; John Wiley & Sons: New York, 1981.

(8)Adman, E. T. *Adv. Protein Chem.* **1991**, *42*, 144.

(9)Solomon, E. I.; Baldwin, M. J.; Lowery, M. D. *Chem. Rev.* **1992**, *92*, 521.

(10)Banci, L.; Bertini, I.; Luchinat, C.; Donaire, A.; Martinez, M.-J. M.; Mascarelli, J. M. *Comments Inorg. Chem.* **1990**, *9*, 245.

(11)Vallee, B. L. ; Spiro, T. G., Ed.; Wiley: New York, 1983, pp 1.

(12)Shimada, H.; Sligar, S. G.; Yeom, H.; Ishimura, Y. *Heme Monooxygenase. A chemical mechanism for cytochrome P450 oxygen activation*; Funabiki, T., Ed.; Kluwer Academic Publishers: Boston, 1997, pp 195.

(13)Chan, S. I.; Li, P. M. *Biochemistry* **1990**, *29*, 1.

(14)Babcock, G. T.; Wikstrom, M. *Nature* **1992**, *356*, 301.

(15)Rosenzweig, A. C.; Frederick, C. A.; Lippard, S. J.; Nordlund, P. *Nature* **1993**, *366*, 537.

(16)Sahlin, M.; Petersson, L.; Graslund, G.; Ehrenberg, A.; Sjoberg, B.-M.; Thelander, L. *Biochemistry* **1987**, *26*, 5541.

(17)Kroneck, P. M. H.; Antholine, W. E.; Koteich, H.; Kastrau, D. H. W.; Neese, F.; Zumft, W. G.; Karlin, K. D. and Tyeklar, Z., Ed.; Chapman & Hall: New York, 1993.

(18)Iwata, S.; Ostermeier, C.; Ludwig, B.; Michel, H. *Nature* **1995**, *376*, 660.

(19)Farrar, J. A.; Thomson, A. J.; Cheesman, M. R.; Dooley, D. M.; Zumft, W. G. *FEBS Lett* **1991**, *294*, 11.

(20)Spira-Solomon, D. J.; Allendorf, M. D.; Solomon, E. I. *J. Am. Chem. Soc.* **1986**, *108*, 5318.

(21)Allendorf, M. D.; Spira, D. J.; Solomon, E. I. *Proc. Natl. Acad. Sci. U. S. A.* **1985**, *82*, 3063.

(22)Messerschmidt, A.; Ladenstein, R.; Huber, R.; Bolognesi, M.; Avigliano, L.; Petruzzelli, R.; Rossi, A.; Finazziagro, A. *J. Mol. Biol.* **1992**, *224*, 179.

(23)Nguyen, H.-H. T.; Shiemke, A. K.; Jacobs, S. J.; Hales, B. J.; Lidstrom, M. E.; Chan,

S. I. *J. Biol. Chem.* **1994**, *269*, 14995.

(24)Nguyen, H.-H. T.; Nakagawa, K. H.; Hedman, B.; Elliott, S. J.; Lidstrom, M. E.; Hodgson, K. O.; Chan, S. I. *J. Am. Chem. Soc.* **1996**, *118*, 12766.

(25)Holm, R. H.; Kennepohl, P.; Solomon, E. I. *Chem. Rev.* **1996**, *96*, 2239.

(26)Malmstrom, B. G. *Chem. Rev.* **1990**, *90*, 1247.

(27)Jolly, R. L., Jr.; Evans, L. H.; Makino, N.; Mason, H. S. *J. Biol. Chem.* **1974**, *249*, 335.

(28)Zaitseva, I.; Zaitsev, V.; Card, G.; Moshkov, K.; Bax, B.; Ralph, A.; Lindley, P. *JBIC* **1996**, *1*, 15.

(29)Ackrell, B. A. C.; Kearney, E. B.; Edmondson, D. *J. Biol. Chem.* **1975**, *250*, 7114.

(30)Hägerhäll, C. *Biochim. Biophys. Acta* **1997**, *1320*, 107.

(31)Elliott, S. J.; California Institute of Technology: Pasadena, 2000.

(32)Hüttermann, J.; Kappl, R. *ENDOR: Probing the coordination environment in metalloproteins*; Sigel, H., Ed.; Marcel Dekker: New York, 1987; Vol. 22, pp 1.

(33)Tsvetkov, Y. D.; Dikanov, S. A. *Electron-spin echo: Applications to biological systems*; Sigel, H., Ed., 1987; Vol. 22, pp 207.

(34)Eaton, G. R.; Eaton, S. S. *Acc. Chem. Res.* **1988**, *21*, 107.

(35)Cammack, R.; Williams, R.; Guigliarelli, B.; More, C.; Bertrand, B. *Biochem. Soc. Trans.* **1994**, *22*, 721.

(36)Ohnishi, T. *Curr. Top. Bioenerg.* **1987**, *15*, 37.

(37)Ackrell, B. A. C.; Johnson, M. K.; Gunsalus, R. P.; Cecchini, G. *Structure and function of succinate dehydrogenase and fumarate reductase*; Müller, F., Ed.; CRC Press: Boca Raton, 1992; Vol. III, pp 229.

(38)Hederstedt, L.; Ohnishi, T. *Progress in succinate:quinone oxidoreductase research*; Ernster, L., Ed.; Elsevier Science Publishers: Amsterdam, 1992, pp 163.

(39)Yu, L., Xu, J.-X., Haley, Paul E., and Yu, Chang-An *J. Biol. Chem.* **1987**, *262*, 1137.

(40)Pennoyer, J. D.; Ohnishi, T.; Trumpower, B. L. *Biochim. Biophys. Acta* **1988**, *935*, 195.

(41)Waldeck, A. R.; Lee, H. K.; Matsson, M.; Hung, S.-C.; Stowell, M. H. B.; Hederstedt, L.; Ackrell, B. A. C.; Chan, S. I. *J. Biol. Chem.* **1997**, *272*, 19373.

(42)Ruzicka, F. J.; Beinert, H.; Schepler, K. L.; Dunham, W. R.; Sands, R. *Proc. Natl. Acad. Sci. U. S. A.* **1975**, *72*, 2886.

(43)Yang, D. C.; Oyaisu, H.; J., O. G.; Woese, C. R. *Proc. Natl. Acad. Sci. U. S. A.* **1985**, *82*, 4443.

(44)John, P.; Whatley, F. R. *Nature* **1975**, *254*, 495.

(45)Mims, W. B. *Physical Review B* **1972**, *5*, 2409.

(46)Iverson, T. M.; Luna-Chavez, C.; Cecchini, G.; Rees, D. C. *Science* **1999**, *284*, 1961.

(47)Lancaster, D. R. D.; Kroeger, A.; Auer, M.; Michel, H. *Nature* **1999**, *402*, 377.

(48)Anthony, C.; Academic Press: London, 1982, pp 296.

(49)Brusseau, G. A.; Tsien, H.-C.; Hanson, R. S.; Wackett, L. P. *Biodegradation* **1990**, *1*, 19.

(50)Moran, B. N.; Hickey, W. J. *Appli. Environ. Microbiol.* **1997**, *63*, 3866.

(51)Sullivan, J. P.; Dickinson, D.; Chase, H. A. *Critical Reviews in Microbiology* **1998**, *24*, 335.

(52)Higgins, I. J. Best, D. J.; Hammond, R.C. *Nature* **1980**, *286*, 561.

(53)Froland, W. A.; Andersson, K. K.; Lee, S.-K.; Liu, Y.; Lipscomb, J. D. *J. Biol.*

Chem. **1992**, *267*, 17588.

(54)Nguyen, H.-H. T.; Elliott, S. J.; Yip, J. H.; Chan, S. I. *J. Biol. Chem.* **1998**, *273*, 7957.

Chapter 2:

Electron Paramagnetic Resonance Studies of Succinate:Ubiquinone Oxidoreductase from *Paracoccus denitrificans*: Evidence for a Magnetic Interaction Between the 3Fe-4S Cluster and Cytochrome *b*

Abstract

Electron paramagnetic resonance (EPR) studies of succinate:ubiquinone oxidoreductase (SQR) from *Paracoccus denitrificans* have been undertaken in the purified and membrane-bound states. Spectroscopic "signatures" accounting for the three iron-sulfur clusters (2Fe-2S, 3Fe-4S, and 4Fe-4S), cytochrome *b*, flavin and protein-bound ubisemiquinone radicals have been obtained in air-oxidized, succinate-reduced, and dithionite-reduced preparations at 4-10 K. Spectra obtained at 170 K in the presence of excess succinate showed a signal typical of that of a flavin radical, but superimposed with another signal. The superimposed signal originated from two bound ubisemiquinones, as shown by spectral simulations. Power-saturation measurements performed on the air-oxidized enzyme provided evidence for a weak magnetic dipolar interaction operating between the oxidized 3Fe-4S cluster and the oxidized cytochrome *b*. Power-saturation experiments performed on the succinate- and dithionite-reduced forms of the enzyme demonstrated that the 4Fe-4S cluster is coupled weakly to both the 2Fe-2S and the 3Fe-4S clusters. Quantitative interpretation of these power-saturation experiments has been achieved through redox calculations. They revealed that a spin-spin interaction between the reduced 3Fe-4S cluster and the cytochrome *b* (oxidized) may also exist. These findings form the first direct EPR evidence for a close proximity ($\leq$ 2 nm) of the high-potential 3Fe-4S cluster, situated in the succinate dehydrogenase (SDH) part of the enzyme, and the low-potential, low-spin *b*-heme in the membrane anchor of the enzyme.

Introduction

Succinate:ubiquinone oxidoreductase, SQR[1], is the only membrane-bound enzyme in the tricarboxylic acid cycle. As 'Complex II', it performs the two-electron oxidation of succinate to produce fumarate, while transferring the electrons to quinone (Q) to yield quinol (QH_2). The reverse process is mediated by quinol:fumarate oxidoreductases (QFR), which occur in anaerobic and some facultative organisms. The two enzymes are related, and are capable of catalyzing their respective reverse reactions under suitable conditions.[1,2]

SQR contains three or four polypeptides depending on the organism. The largest subunit, a flavoprotein (FP), contains the dicarboxylate binding site and one flavin moiety (FAD); the latter is covalently bound in most cases. The iron-sulfur protein (IP) is intermediate in size and contains three iron-sulfur clusters of type 2Fe-2S, 4Fe-4S, and 3Fe-4S, often referred to as S-1, S-2, and S-3, respectively, in the case of SQR. These two hydrophilic subunits protrude into the cytosol (prokaryotic enzyme) or the mitochondrial matrix (eukaryotic enzyme), and together catalyze the succinate dehydrogenase (SDH) activity of the enzyme. They are anchored to the membrane by one or two hydrophobic quinone polypeptides (QP), which may contain zero, one, or two *b*-heme(s). These anchoring subunits confer reactivity with the bound Q's; for SQR from bovine-heart[3,4] and a variety of higher plants,[5] the existence of two Q sites has been

---

[1] The abbreviations used are: SQR, succinate:ubiquinone oxidoreductase; E_m, redox midpoint potential; FAD, flavin adenine dinucleotide; Hepes, 4-(2-hydroxyethyl)-1-piperazine-ethanesulfonate; $P_{1/2}$, half-saturation parameter; $Q_{2(6)(10)}$, ubiquinone-2(6)(10); S-1, 2Fe-2S cluster; S-2, 4Fe-4S cluster; S-3, 3Fe-4S cluster; SDH, succinate dehydrogenase; Thesit, polyoxethylene (9) lauryl ether; Tris, Tris(hydroxymethyl)aminomethane; Triton X-100, polyethylene glycol tert-octylphenyl ether; Q, (ubi)quinone; Q•, (ubi)semiquinone; QFR; quinol:fumarate oxidoreductase; QH_2, (ubi)quinol; MOPS, 4-morpholinepropanesulfonic acid.

established. SQR from *Paracoccus denitrificans* contains covalently bound FAD; the membrane-anchor consists of two polypeptides with a mono-heme cytochrome *b*.[6] Despite extensive efforts [for reviews see ref. 1,2,7], the electron-transfer pathway(s) and the mechanism of Q reduction in SQR remain controversial.[1,8,9]

We chose to study the enzyme from *P. denitrificans* for the following reasons. The membrane-bound form of the *P. denitrificans* enzyme in whole cells is characterized by electron paramagnetic resonance (EPR) signals like those observed in mammalian mitochondria.[10] *P. denitrificans* appears to be the closest bacterial homologue to this organelle,[11,12] and its SQR is amenable to molecular genetic techniques. The purification and basic biochemical properties of SQR from this bacterium have also been reported.[6]

The air-oxidized, ferricyanide-oxidized, succinate- and dithionite-reduced forms of the enzyme have been investigated by EPR spectroscopy. Spectroscopic "signatures" accounting for each of the redox centers have been obtained at these different levels of reduction of the protein. EPR spectral simulations of the radical signals are consistent with two Q binding sites. An EPR signal characteristic of a *reduced* 3Fe-4S cluster has been observed for the first time for SQR or QFR. In addition, we have analyzed quantitatively the power-saturation and redox behavior of the S-3 center in the air-oxidized enzyme, and the S-3 and S-1 centers in the succinate-reduced enzyme. Taken together, we conclude that S-3 center and the *b*-heme are coupled magnetically in their oxidized states, and presumably in their respective reduced and oxidized states, as well.

Experimental Procedures

Materials — Centricon ultrafiltration tubes were from Amicon Inc., Beverly, MA; Dodecyl-β-D-maltoside, DDM, was from Anatrace, Maumee, OH; 4-amino-TEMPO, (4-amino-2,2,6,6-tetramethyl-1-piperidinyloxyl), and Sephadex G-50 were purchased from Sigma Chemical Co., St Louis, MO; Polyethylene glycol tert-octylphenyl ether; Tris, Tris(hydroxymethyl)aminomethane; Triton X-100, and polyoxethylene (9) lauryl ether, Thesit, were purchased from Boehringer Mannheim Corp., IN, or Mannheim, Germany; Amberlite XAD-2 adsorbent was from Serva, Heidelberg, Germany. All other reagents were of AR grade.

Cell Growth Conditions and Membrane Isolation — Growth of *P. denitrificans* (ATCC No. 13543) used for isolation of SQR was performed as described previously.[13] Cells were harvested with a continuous flow centrifuge and frozen in liquid nitrogen as 200-gram flat packs. Growth conditions for the PD1222/pPSD100 strain containing overproduced (~2-fold) SQR, its construction, and isolation of membranes from it, will be described elsewhere.[63]

Enzyme Purification — SQR was purified by thawing the stored cell packs using 150-200 g of material each time. The purification procedure was as described previously,[6] with modifications similar to those described in.[14,15] The enzyme was concentrated and the salt and Triton X-100 concentrations of the final samples were reduced, the latter to ~0.05 % (w/v), by repeated exchange in Centricon 100 kDa cutoff

concentrators against 100 mM Hepes, pH 7.4. The final yield was 1-2 ml of 50-100 μM SQR. SQR from the PD1222/pPSD100 strain was purified in an identical fashion to that from the ATCC No. 13543 strain. The enzyme was considered sufficiently pure (> 90%) for use in our experiments by criteria of optical spectra (negligible absorption due to hemes other than b_{557}) and SDS-PAGE.[6]

Analytical Procedures — Enzyme concentrations were determined by measuring the acid-non extractable FAD content of the samples.[16] Cytochrome *b* concentrations were determined from dithionite reduced-minus-oxidized difference spectra in a pyridine hemochrome assay mixture, using $\Delta\epsilon_{557\text{-}540} = 24.0\ mM^{-1}\ cm^{-1}$.[17] The SQR activity was measured with a large excess of ubiquinone-2 (Q_2; 20 μM) and dichlorophenol-indophenol (DCPIP) as the primary and terminal electron acceptors, respectively;[6,18] activation of the enzyme was achieved by incubating the enzyme (in Triton X-100) for 20 min at 298 K in 50 mM Tris buffer, 50 mM sodium succinate, 0.2 mM DDM, pH 7.5. Typical turnover numbers (mol succinate/mol SQR) of the purified enzyme at 310 K were 300-350 s^{-1} based on the FAD concentrations of the samples [see also ref. 6]. Extraction of the protein-bound ubiquinone-10 (Q_{10}) was performed according to the procedure of Redfearn.[19] Its concentration was determined using ubiquinone-6 (Q_6) as an internal standard for analysis by HPLC (275 nm) employing a C_{18} reverse-phase column and eluting with a solvent gradient starting at 25:75% water:acetonitrile and finishing at 100% acetonitrile.

EPR Sample Preparation — Samples stored at 193 K were thawed on ice and equilibrated with argon prior to freezing the samples in liquid nitrogen in order to remove oxygen from the system. Samples reduced with excess sodium succinate (35-100 mM, pH 7.4) were incubated for 45 min at 297-300 K; (sodium) dithionite-reduced samples (10 mM, pH 7.4) were incubated for 5 min at the same temperature. The succinate concentrations were varied between 35-100 mM to yield [succinate] / [SQR] ≈ 1300 (E ≈ -71 mV, where E denotes solution potential; *vide infra*), for samples with different SQR concentrations; dithionite-reduced samples may be approximated by E ≤ -400 mV. Succinate- and dithionite-reduced PD1222/pPSD100 membranes in 20 mM MOPS, 65 mM Hepes, pH 7.4 were treated identically, except for the addition of 2 mM KCN (final concentration) to these samples. Ferricyanide-oxidized SQR was obtained by incubating the sample with excess ferricyanide, which was subsequently removed by Sephadex G-50 column filtration. Samples to which a three-fold excess of (exogenous) Q_2 were added were incubated for 5 min at 295 K and subsequently reduced with excess succinate, as described above. The QP were isolated from detergent-depleted SQR using perchlorate, essentially as described for the mammalian enzyme.[20] The nonionic detergent Thesit (1.5% w/v) was removed from the SQR-detergent micelle mixture by adsorption to Amberlite XAD-2 beads.

EPR Methods — EPR spectra were recorded on a Varian E-109 X-band spectrometer equipped with a E-231 TE-102 rectangular cavity, and interfaced with an IBM personal computer for accumulation and digitization of the spectra. Sample temperature was controlled by a variable temperature helium flow cryostat system

(Oxford Instruments). Spectral manipulation was performed using the program Labcalc on an IBM personal computer. Quantitation of the reduced S-1 and S-3 signal intensities (Figure 5) was performed by measuring peak heights;[21] double integration of the digitized first-derivative spectra was performed in the case of the oxidized S-3 center (Figure 4). Spectra obtained at liquid helium temperatures (4–20 K) were baseline-corrected by subtracting spectra derived from a buffer-filled EPR tube under identical conditions. EPR signal linewidths are given as peak-to-trough linewidths under nonsaturating conditions. The combined spin concentrations of the radical signals due to FAD• and Q•][2] of the purified preparations (*solid lines* in Figure 3**A**, **C**, and **E**) have been determined using a 4-amino-2,2,6,6-tetramethyl-1-piperidinyloxyl standard under nonsaturating conditions.[3] EPR acquisition parameters are given in the figure legends; the number of scans taken per spectrum is one, unless mentioned otherwise.

Computational Procedures — EPR simulations of the composite FAD•-Q• signal (Figure 3) have been carried out using the program EPR, a modelling approach (F. Neese, University of Konstanz, Konstanz, Germany) on an IBM-compatible 486:50 MHz computer. The computer program uses first-order perturbation theory to simulate the EPR transitions as a function of the magnetic field (or frequency). This treatment was deemed to be sufficient, as the condition $A_0 \ll g_e \beta_e B$ is fulfilled for radicals; i.e., their hyperfine interactions are much smaller than their Zeeman interactions. Initial

---

[2] We shall not distinguish here between the protonated and anionic forms of the FAD and Q semiquinones. In the bovine heart enzyme FAD• and Q• are predominantly in the protonated[49] and anionic[45] forms at physiological pH, respectively.

[3] The FAD• saturates at $P \geq 30$ μW in the *P. denitrificans* (A. R. W., H. K. L., and S. I. C. unpublished results) and bovine-heart enzymes.[37]

estimates of the anisotropy (axiality) in the g and hyperfine (A) matrices corresponding to the strongly coupled nitrogens of the FAD•, as well as the linewidths (x,y,z) of the FAD•, were obtained from those reported previously for flavoproteins. Proton hyperfine interactions and 'g-strain' were neglected.[22] Initial simulations were generated using the option "Spectra series," which allows the simulator to test the effect of a particular EPR parameter on the (simulated) spectrum. When a satisfactory likening between the simulated and experimental spectrum was obtained, the g-values and spectral weights of the Q• were "fine-tuned" using the option "Fit" (Simplex algorithm; see Results and the legend of Figure 3 for further details).

Redox calculations used to estimate the percentage reduction of the redox centers within SQR in the presence of excess succinate ($E \approx -71$ mV) and dithionite ($E < -400$ mV) were programmed in Mathematica (version 2.2.2);[23] the program is available from Dr. Chan upon request. The values of the redox midpoint potentials (E_m values) used in the calculations were those measured for the bovine-heart enzyme,[4] unless mentioned otherwise[5]: $E_m^{FAD/FAD\bullet} = E^{FAD\bullet/FADH_2} = -71$ mV[5]; $E_m^{S\text{-}1_{ox}/S\text{-}1_{red}} = -14$ mV[4];[24] $E_m^{S\text{-}2_{ox}/S\text{-}2_{red}} = -$

---

[4] Preliminary redox titrations (S-C. H., A. R. W., and S. I. C. unpublished results) have shown that $E_m \approx 60$ mV for the *P. denitrificans* S-3 center, as in the bovine heart enzyme.[26] A spin-concentration of 90% is predicted for the S-1 center using the bovine heart E_m value (-14 mV);[24] this compares well with the 88% measured experimentally (see "Results"). The resonances due to the S-2 center are elicited by dithionite-reduction, but not by succinate-reduction, as in the bovine-heart protein ($E_m = -260$ mV).[25]

[5] The spin-concentration of the composite FAD•-2Q• signal (Fig. 3) in succinate-reduced samples ($E \approx -71$ mV) has been measured (see "EPR Methods") to amount to ~44% of the FAD (protein) concentrations for enzyme isolated from both strains. Using this estimate and the spectral weight of ($Q_A\bullet + Q_B\bullet$) with respect to FAD• (see legend of Figure 3) we estimate 33% FAD•:FAD and 11% Q•:FAD (16% Q•:Q), and 36% FAD•:FAD and 8% Q•:FAD ($\geq$ 4% Q•:Q) for samples isolated from the ATCC No. 13543 and PD1222/pPSD100 strain supplemented with a 3-fold excess of Q_2, respectively (see also legend of Figure 3). Note that in the latter preparation *maximally* 2 Q may bind. These spin concentrations are reproduced in the redox calculations using: $E_m^{FAD/FAD\bullet} = E_m^{FAD\bullet/FADH_2} = -71$ mV; and $E_m^{Q/Q\bullet} = 30$ mV; $E_m^{Q\bullet/QH_2} = -20$ mV, $E_m^{Fe^{3+}/Fe^{2+}} = -175$ mV at pH 7.4 for the *P. denitrificans* enzyme (measured using redox mediators) (M. Matsson and L. Hederstedt, unpublished results).

260 mV**4**;[25] $E_m^{S-3_{ox}/S-3_{red}}$ = 60 mV**4**;[26] $E_m^{Fe^{3+}/Fe^{2+}}$ = -175 mV mV**5**; $E_m^{Q/Q^{\bullet}}$ = 30 mV**5**; $E_m^{Q^{\bullet}/QH_2}$ = -20 mV.**5**

The half-saturation parameter, $P_{1/2}$, was obtained from the EPR power-saturation data in Figure 4**A** using curves generated in Mathematica.[27,28] The power-saturation data in Figures 4 and 5 were (also) analyzed using non-linear least-squares regression onto the data of a semi-empirical equation**6** (see also Table 2)[29,30] using the program Kaleidograph.

Results

SQR from various eukaryotes and prokaryotes has been characterized by EPR in the membrane-bound and purified states.[1] The bovine-heart protein has been under intense investigation for many years,[1,2,7] and should serve as an excellent point of departure for the *P. denitrificans* enzyme, because of its close evolutionary linkage.[11] Also, the amino acid sequence similarity of the FP and IP subunits is highly conserved between species.[1]

We have focused on three issues in the present study: (1) EPR "fingerprinting" of membrane-bound and purified SQR, (2) investigating the EPR power-saturation behaviors of the EPR signals of the iron-sulfur clusters centers in an attempt to derive structural information from their spin-relaxation behavior, and (3) performing redox calculations allowing quantitative interpretation of the experimental results.

---

6 $I = K P^{1/2} [1 + (P / P_{1/2})]^{-b/2}$, where I, K, P, $P_{1/2}$, and b denote absorption integral or derivative intensity, proportionality constant, microwave power, half-saturation parameter, and inhomogeneity parameter, respectively.[29,30]

Fingerprinting Spectra — EPR spectra of "as-isolated" (i.e., air-oxidized), succinate-, and dithionite-reduced membranes of the SQR overproducing PD1222/pPSD100 strain are shown in Figure 1. The spin-states of the redox centers of the enzyme at the three levels of reduction are given in Table 1. For air-oxidized SQR, the almost isotropic resonance centered at g = 2.006 with a linewidth of 2.5 mT (Figure 1**A**) is characteristic of a signal arising from the oxidized S-3 center (see also Figure 2**A**).[1,31,32] The very broad trough superimposed onto the S-3 signal (see inset for absorption signal) forms part of a $g_y \approx 2.1$ component of the *b*-heme of SQR. This g-value falls within the range of g_y-values reported for low-spin ferric hemes,[33-35] and is the same as that for the purified enzyme (*vide infra*).

Table 1. Spin states[a] of the redox centers in SQR in the absence and presence of excess succinate[b] and dithionite.

Center	Air-oxidized	EPR	Succinate-reduced	EPR	Dithionite-reduced	EPR
FAD	S = 0	—	FAD•, S = 1/2	√	$FADH_2$, S = 0	—
S-1	Fe^{3+} (5/2) - Fe^{3+} (5/2) $S_T = 0$	—	Fe^{3+} (5/2) - Fe^{2+} (2) $S_T = 1/2$		Fe^{3+} (5/2) - Fe^{2+} (2) $S_T = 1/2$	√
S-2	Fe^{3+} - Fe^{2+}, $S_1 = 9/2$ Fe^{3+} - Fe^{2+}, $S_2 = 9/2$ $S_T = 0$	—	Fe^{3+} - Fe^{2+}, $S_1 = 9/2$ Fe^{3+} - Fe^{2+}, $S_2 = 9/2$ $S_T = 0$	—	Fe^{3+} - Fe^{2+}, $S_1 = 9/2$ Fe^{2+} - Fe^{2+}, $S_2 = 4$ $S_T = 1/2$	√
S-3	Fe^{3+}-Fe^{3+}, $S_1 = 0$ Fe^{3+}, $S_2 = 5/2$ $S_T = 5/2$[c]	√	Fe^{3+} - Fe^{2+}, $S_1 = 9/2$ Fe^{3+}, $S_2 = 5/2$ $S_T = 2$	√	Fe^{3+} - Fe^{2+}, $S_1 = 9/2$ Fe^{3+}, $S_2 = 5/2$ $S_T = 2$	√
b-heme	Fe^{3+} (1/2), S = 1/2	√	Fe^{3+} (1/2), S = 1/2	√	Fe^{2+}, S = 0	—
Q_A	S = 0	—	Q_A•, S = 1/2	√	Q_AH_2, S = 0	—
Q_B	S = 0	—	Q_B•, S = 1/2	√	Q_BH_2, S = 0	—

[a] The iron atoms in the iron-sulfur clusters are 'high-spin' (S = 5/2; see S-1); the heme-iron is 'low-spin' (S = 1/2). The total spin state (S_T) of the iron-sulfur clusters are calculated using antiferromagnetic interactions between the individual spins or "spin-pairs" (subscripts 1, 2). The interactions between spin pairs are ferromagnetic; see, e.g., S-2.

[b] Note that succinate is a mild reductant. Thus, addition of (excess) succinate to a sample of SQR elicits a "semireduced" (heterogeneous) state of the protein (see Results).

[c] Formally $S_T = 5/2$, but the Kramers' doublet ground state ($S_T = 1/2$) is the operative spin state at T = 4 K (Figure 4**A**).

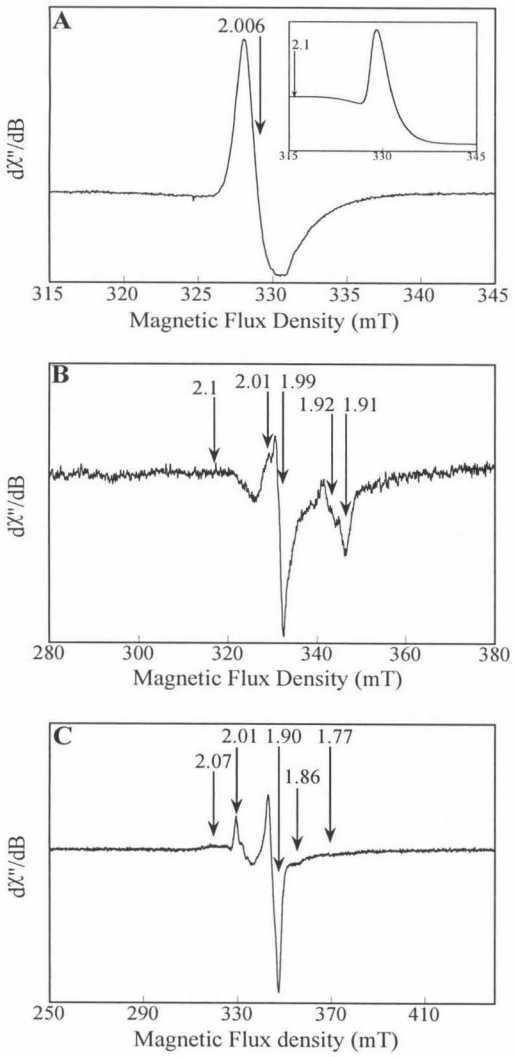

Figure 1. EPR spectra of membranes of the ~2-fold overproducing *P. denitrificans* strain, PD1222/pPSD100 [0.30 nmol FAD per mg protein (~2-fold overproduced); 3 mg protein/ml]. (**A**) No reductant added. EPR parameters: magnetic field, 330 mT; modulation amplitude, 0.5 mT; modulation frequency, 100 kHz; microwave power, 0.2 mW; microwave frequency, 9.236 GHz; field sweep rate, 0.17 mT s^{-1}; time constant, 0.064 s; temperature, 4 K. The *inset* shows the absorption (integrated) spectrum. (**B**) Succinate-reduced. EPR parameters were as in **A**, except for: modulation amplitude, 0.8 mT; field sweep rate, 0.21 mT s^{-1}; time constant, 0.25 s; number of scans, 2. (**C**) Dithionite-reduced. EPR parameters were as in **B**, except for: magnetic field, 350 mT; microwave power, 1 mW; temperature, 5 K. Relative gains of spectra **A**, **B**, and **C** were 1:7.5:2.3.

The above assignment to the *b*-heme was confirmed by the persistence of the signal in the succinate-reduced spectrum (Figure 1**B**), as the E_m of the cytochrome *b* of the *P. denitrificans* enzyme[5] is much lower than that of the fumarate:succinate couple at pH 7.4 [5 mV; ref. 36]. Therefore, it is not reduced appreciably (~8%; data not shown) by succinate (see also Figure 2, **A** and **B**). The g_z-component, $3 < g_z < 4$, was also detectable, though barely (spectral region not shown, but see Figure 2, **A** and **B**, for evidence of this feature). In addition, reduction with succinate elicited an almost axial ferredoxin-like spectrum for the S-1 center

with $g_z = 2.01$, $g_y = 1.92$, and $g_x = 1.91$ (Figure 1**B**); the g = 1.99 signal is characteristic of the FAD• of SQR.[10,37-39]

Upon addition of dithionite to the sample, broad resonances at g = 2.07 (positive maximum), and 1.86 and 1.77 (negative minima) due to the S-2 center appeared, superimposed onto those of the S-1 center, but those due to the FAD• and the *b*-heme disappeared (Figure 1**C**). Assignment of the former features to the S-2 center was based on the fact that they were not elicited in the succinate-reduced spectrum, the S-2 center being a low-potential center [E_m = -260 mV in the bovine-heart enzyme ref. 25]. Also, these signals are of very low intensity in SQR and fumarate reductase; this low intensity is thought to be due to spin-spin interactions with the other iron-sulfur clusters[1,40] (see Figure 5 for the relevant power-saturation experiments).

Figure 2 depicts spectra recorded on purified SQR. Figure 2**A** shows a nearly isotropic (g = 2.008) S-3 resonance (linewidth, 1.9 mT; see also ref. 6) observed for the as-isolated enzyme. The EPR signal intensities of the ferricyanide-oxidized and as-isolated S-3 center were not significantly different; therefore, the 3Fe-4S cluster in as-isolated samples of the enzyme was present in its oxidized state. The broad trough was (again) assigned to the g_y-component of the *b*-heme (~2.1). The 0-300 mT region of the spectrum (*inset*) for the as-isolated protein shows peaks at g = 5.9 and 4.2, and a very small one at g = 3.6; these features were assigned to high-spin ferric hemes (presumably originating from slight contamination with terminal oxidases), adventitious iron, and a g_z-component due to the *b*-heme, respectively.

The extent to which g-anisotropy could be the cause of the low intensities of the *b*-heme g_z- and g_y-components[33,34] was ascertained by comparing the intensities of the

g_z-components of low-spin heme signals from different species. This effect was excluded because the g_z-value of the *P. denitrificans* *b*-heme is comparable to that of the low-potential *b*-heme of the bovine-heart enzyme (g_z = 3.46; E_m = -185 mV)[41] and the high-potential *b*-heme of the *B. subtilis* succinate:menaquinone oxidoreductase (g_z = 3.68; E_m = 65 mV).[42] To determine whether the virtual EPR-invisibility of the *b*-heme (g_z- and g_y-components) was due to relaxation-enhancement of this metal center by the S-3 center, or due to an extremely short *intrinsic* spin-lattice relaxation time,

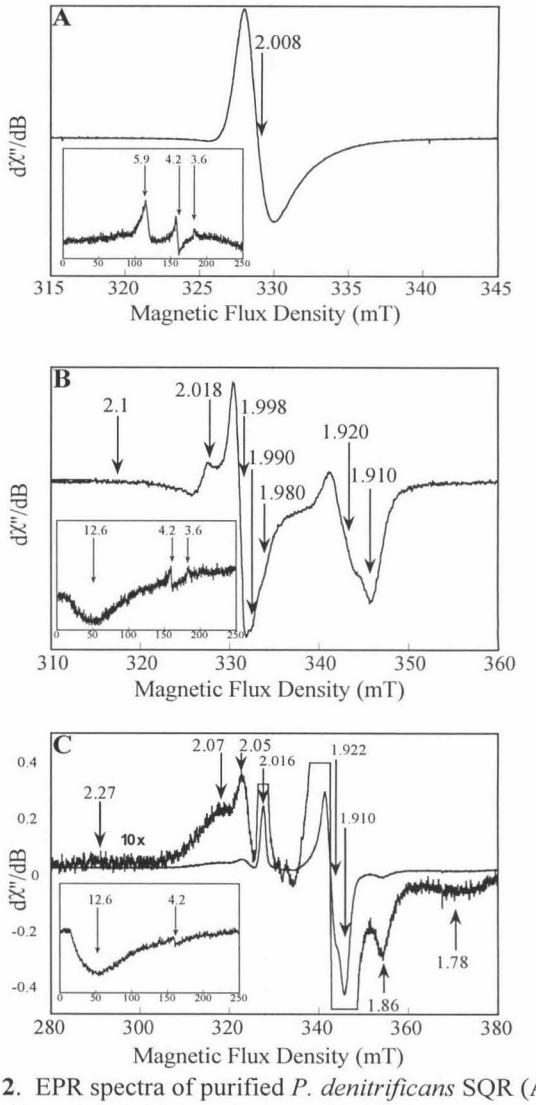

Figure 2. EPR spectra of purified *P. denitrificans* SQR (ATCC No. 13543 strain). (**A**) No reductant added (106 μM FAD; 79 μM *b*-heme). EPR parameters: magnetic field, 330 mT; modulation amplitude, 0.5 mT; modulation frequency, 100 kHz; microwave power, 1.0 mW; microwave frequency, 9.234 GHz; field sweep rate, 0.08 mT s^{-1}; time constant, 0.064 s; temperature, 4 K. (**B**) Succinate-reduced SQR (77 μM FAD; 78 μM *b*-heme). EPR parameters were as in **A**, except for: field sweep rate, 0.21 mT s^{-1}; time constant, 0.13 s. (**C**) Dithionite-reduced; FAD and *b*-heme concentrations as in **B**. EPR parameters were as in **B**, except for: temperature, 10 K. Relative gains of spectra **A**, **B**, and **C** were 1:20:5. The *insets* show the entire 0-300 mT spectral regions. The relative gains of the insets to spectra **A**, **B**, and **C** were 15:1:1; the temperatures were 4, 8, and 4 K, respectively.

T_1, we prepared isolated QP. The EPR of the isolated QP (24 μM *b*-heme) showed a very small $g_z = 3.6$ signal (spectrum not shown), again in comparison with the g_z-signals originating from the bovine-heart enzyme and the *B. subtilis* succinate:menaquinone oxidoreductase, for comparable *b*-heme concentrations. Thus, it was concluded that the intrinsic T_1 of the cytochrome is very short.

Succinate-reduced purified SQR (Figure 2**B**) gives rise to resonances at $g_z = 2.018$, $g_y = 1.920$, and $g_x = 1.910$ due to the reduced S-1 center. The $g_y \approx 2.1$ and $g_z \approx 3.6$ components due to the *b*-heme persist, as expected. A FAD• signal is observed at $g = 1.998$. The "shoulders" at $g = 1.990$ and 1.980 are attributed to Q• and scalar coupling of the FAD free radical electron to a strongly coupled nitrogen atom,[22] respectively (*vide infra*; Figure 3). The spectral feature due to the Q• in the membrane-bound enzyme was less readily detected due to the lower signal-to-noise ratio of that spectrum (see Figure 1**B**). The *inset* in Figure 2**B** shows a broad signal at $g = 12.6$ due to the reduced S-3 center. This spectral feature is consistent with a $\Delta M_S = 4$ transition within the $S_T = 2$ spin-manifold of the iron-sulfur cluster[43,44] (see also "Discussion").

The dithionite-reduced enzyme (Figure 2**C**) shows the spectral features expected from reduced centers S-1, at $g_z = 2.016$, $g_y = 1.922$, and $g_x = 1.910$, [see also ref. 6]; and S-2, at 2.27, 2.07, 2.05 (positive maxima), and 1.86 and 1.78 (negative minima). The g-values of the S-1 center are virtually identical to those characterizing the iron-sulfur cluster in the succinate-reduced state of the enzyme (*vide supra*; Figure 2**B**). This result suggests little or no reorganization of the ligands of the 2Fe-2S cluster upon reduction of the 4Fe-4S cluster. However, the succinate-reduced enzyme yielded ~0.88 spins/molecule compared with 1.00 for the dithionite-reduced sample, as measured from

the intensities of the g_x-components of the 2Fe-2S cluster in the two samples. The integrated intensities of the resonances in the dithionite-reduced enzyme due to the S-1 and S-2 centers were approximately twice (2.15 ± 0.07; N = 2) that of the S-1 center alone. We take these findings as evidence for the fact that these centers are present in a 1: 1 molar ratio in the purified enzyme. The reduced S-3 center remained EPR-active (g = 12.6) as expected (see Table 1) in the dithionite-reduced sample; the g = 12.6 signal has also been observed for the succinate- and dithionite-reduced membranes (spectra not shown).

EPR Spectral Simulations of the Radical Signals — SQR from bovine-heart[1,3,4,45-47] and a variety of higher plants[5] binds tightly two Q's, of which the semi-quinone form is stabilized preferentially. In the bovine-heart enzyme a four-line spectrum is observed at E ≈ 100 mV and T = 10-13 K,[1,46,47] or during turnover (100 ms).[3] The spectral features appear to be best simulated by a dipolar-coupled Q•-Q• signal superimposed onto that of a non-interacting oxidized S-3 center.[3,45] However, evidence attesting to the possibility that the oxidized S-3 center ($M_S = \pm 1/2$; ground state Kramer's doublet; see Table 1) interacts with the Q• has been provided by EPR simulation, and the fact that the spectroscopic features disappear concomitantly with reduction of the S-3 center.[3] In our experiments we observed a signal reminiscent of Q• in the equilibrium succinate-reduced state of the *P. denitrificans* enzyme at 4 K (Figure 2**B**); however, no observable splittings were present at this low temperature, as may be expected for the reduced state of the S-3 center ($S_T = 2$; see Table 1). Therefore, we performed EPR spectral simulations of the g = 2 region of the succinate-reduced enzyme at 170 K (Figure 3). At

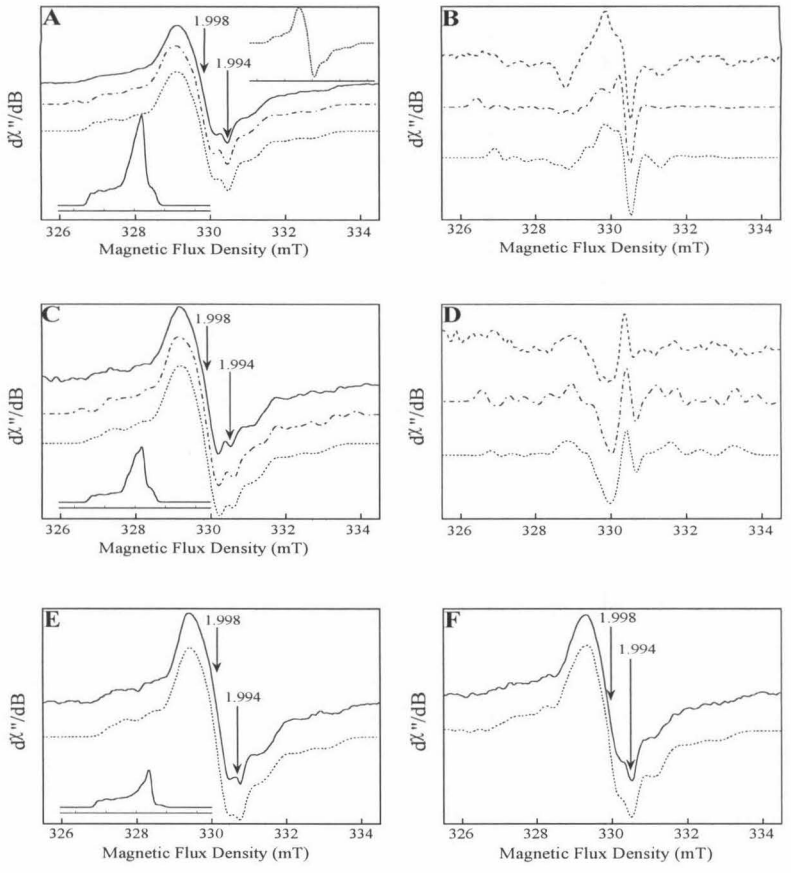

Figure 3. EPR spectra and spectral simulations of the g = 2 region of purified and membrane-bound succinate-reduced SQR at 170 K. (**A**) EPR spectrum (*solid line*) from purified SQR (average of two spectra; ATCC No. 13543 strain; 20 μM FAD; 22 μM *b*-heme; 13 μM Q_{10}) and simulations of a FAD• with one (*dashed-dotted line*) or two superimposed Q• (*dotted line*). The *inset* in the *top right-hand corner* depicts a simulation of the "pure" FAD• (see "Results"). The *inset* in the *lower left-hand corner* shows the absorption signal of the two Q• for the dotted line. The FAD•:FAD and Q•:Q molar ratios[5] are 0.33 and 0.17, respectively. (**B**) The effect of superposition of one and two Q• signals onto that of the FAD• for the spectra shown in **A**. *Dashed line*, experimental spectrum minus FAD• simulation; *dashed-dotted line*, FAD•-1Q• simulation minus FAD• simulation; *dotted line*, FAD•-2Q• simulation minus FAD• simulation. (**C**) EPR spectrum obtained on purified SQR samples from the PD1222/pPSD100 strain (39 μM FAD; 42 μM *b*-heme; 4 μM Q_{10}, supplemented with 117 μM Q_2; *solid line*) and spectral simulations of a FAD• superimposed with one (*dashed-dotted line*) or two Q• (*dotted line*). The *inset* shows the absorption signal of the two Q• for the *dotted line*. The FAD•: FAD and Q•: Q molar ratios[5] are 0.36 and ≥ 0.04, respectively. (**D**) The effect of superposition of one and two Q• signals onto that of the FAD• (as in **B**) for the spectra shown in **C**. (**E**) EPR spectrum obtained on SQR purified from the PD1222/pPSD100 strain (46 μM FAD; 58 μM *b*-heme; 11 μM Q_{10}; solid line) and spectral simulation of a FAD• superimposed with two Q• (*dotted line*). The *inset* shows the absorption signal of the two Q• (*dotted line*). The FAD•:FAD and Q•:Q molar ratios[5] are 0.38 and 0.25, respectively. The relative absorption integrals for the insets in **A**, **C**, and **E** are: 1.00, 0.60, and 0.43, respectively; they reflect the relative Q•(Q_A• + Q_B•) spin-concentrations of the three preparations. (**F**) EPR spectrum (*solid line*) and simulation (*dotted line*) of membrane-bound SQR (0.30 nmol FAD:mg protein; 3 mg protein/ml). EPR parameters: magnetic field, 330 mT; modulation amplitude, 0.2 mT; modulation frequency, 100 kHz; microwave power, 0.5 mW (saturating conditions with respect to FAD•[3]); microwave frequency, 9.243 (**A**), 9.246 (**C** and **F**), 9.253 (**E**) GHz; field sweep rate, 0.167 mT s^{-1}; time constant, 0.250; number of scans, 100 (16 for **C** and **E**); temperature 170 K. Simulation parameters, FAD• (*inset* **A**): $g_{x,y,z}$ = 2.0008, 2.0019, 2.0033; $A_{\|}$ - A_z = 21.8 MHz and 54.2 MHz for N(5) and N(10), respectively. Gaussian linewidth (x,y,z) = 0.454, 0.325, 0.366 mT; these parameters were kept constant. Q•: Gaussian linewidth (x,y,z) = 0.155 mT (kept constant). Spectral weight of Q• (with respect to FAD•) Q• = 0.26, $g_{x,y,z}$ = 1.9982, 1.9986, 2.0229, for the *dashed-dotted line* in **A**. Q_A• = 0.26, $g_{x,y,z}$ = 1.9978, 1.9988, 2.0199; Q_B• = 0.09, $g_{x,y,z}$ = 1.9932, 2.0005, 2.0052, for the dotted line in **A**. Q• = 0.16, $g_{x,y,z}$ = 1.9686, 1.9982, 2.0229, for the *dashed-dotted line* in **C**. Q_A•, weight = 0.14; $g_{x,y,z}$ = 1.9980, 1.9980, 2.0210; Q_B•, weight = 0.07; $g_{x,y,z}$ = 1.9932, 2.0005, 2.0052, for the *dotted line* in **C**. Q_A•, weight = 0.14; $g_{x,y,z}$ = 1.9984, 1.9988, 2.0200; Q_B•, weight = 0.01; $g_{x,y,z}$ = 1.9932, 2.0005, 2.0052, for the *dotted line* in **E**. Q_A• = 0.24, $g_{x,y,z}$ = 1.9982, 1.9992, 2.0333; Q_B• = 0.14, $g_{x,y,z}$ = 1.9943, 2.0016, 2.0051, for the *dotted line* in **F**.

this temperature the resonances due to the S-1 center and the *b*-heme are conveniently broadened beyond detection.

We have simulated the experimental composite FAD•-Q• signal to establish whether the *P. denitrificans* enzyme binds one or two Q•. We have studied three different preparations from two strains. The first preparation (ATCC No. 13453 strain) contained 0.7 bound Q_{10}: FAD (see Figure 3**A**); the second (PD1222/pPSD100 strain) contained 0.1 bound Q_{10}: FAD and was supplemented with a three-fold stoichiometric excess (with respect to the FAD concentration) of exogenous Q_2 (see Figure 3**C**); the control for this sample was a non-supplemented sample containing 0.2 Q_{10}: FAD (see Figure 3**E**). In the Q_2-supplemented preparation, we assume that the binding site(s) (is) are saturated with Q_2; in the former the Q_{10} is sub-stoichiometric with respect to the enzyme, and distributes over the two Q-sites (Q_A and Q_B; if present) according to their relative affinities ($1/K_d$'s), which are unknown at present.

To achieve our objective of assigning one or two Q sites to the *P. denitrificans* enzyme, without having an experimental spectrum of the "pure" *P. denitrificans* FAD• signal (*vide infra*), we simulated the composite signal with a FAD• and either one or two superimposed Q•. Evidence for the g = 1.994 spectroscopic feature originating from Q• has come from comparison of the three samples with different Q contents. In accordance with the different Q content of these preparations, the g = 1.994 feature was altered (see legend to Figure 3, **A**, **C**, and **E**).

We commenced by adjusting/fitting (see "Computational Procedures" for details) the EPR spectral parameters associated with the FAD• and one Q• (Figure 3, *dashed-dotted line*) to the experimental FAD•-Q• spectrum (*solid line*) of the enzyme isolated

from the ATCC No. 13543 strain; this simulation was then repeated with two Q• (Figure 3**A,** *dotted line*). The hyperfine (*A*) constants, g-values and linewidths characterizing the EPR transitions of the FAD•, and the linewidths of the Q•, for which a good fit to the experimental (FAD•-Q•) spectrum was obtained in both cases, were then kept constant (see Figure 3 legend for their values). Thus, the EPR parameters that best characterized the *P. denitrificans* FAD• were decided upon, and chosen to represent the pure FAD• signal (see *inset* of Figure 3**A**; *top right-hand corner*). Further refinement (fitting; see "Computational Procedures") of the FAD•-1Q• and FAD•-2Q• simulations involved the g-values and weights of the (two) Q•.

It is clear from Figure 3**A** that the experimental spectrum of the ATCC No. 13543 strain is rather well simulated using either one or two superimposed Q•, although the FAD•-2Q• simulation appears superior (see, e.g., 329 mT region of the spectrum). However, to circumvent this problem, we subtracted the FAD• simulation from the experimental spectrum and from the FAD•-1Q• and FAD•-2Q• simulations. Thus, this procedure yields the features due to one Q• or two Q• only (see Figure 3**B**), allowing us to discriminate more precisely between the FAD•-1Q• and FAD•-2Q• simulations. We conclude that the composite FAD•-Q• signal is best simulated using two Q•. The same procedure was then followed for the enzyme purified from the PD1222/pPSD100 strain in the presence of exogenous Q_2 (three-fold excess; Figure 3**C**). Again, the simulated spectral features are better for the simulation with two Q• (*dotted lines* in Figure 3, **C** and **D**). The experimental spectrum (*solid line*) and simulation (*dotted line*) for a similar preparation without added Q_2 is shown in Figure 3**E**. The spectrum obtained on the

membrane-bound enzyme (*solid line*) and its FAD•-2Q• simulation (*dotted line*) are shown in Figure 3**F**.

The FAD• signals with their characteristic "wings," due to the strongly coupled N(5) and N(10) nitrogens[22,48,49] are observed in both the purified and membrane-bound preparations (*solid lines* in Figure 3, **A**, **C**, **E**, and **F**, respectively). The linewidth of the FAD• signal of the purified preparation is 1.15 mT. The "extreme shoulders" are separated by 5.4 mT, and are due to the molecules with the magnetic field perpendicular to the plane of the FAD ring system. The values of the linewidth and the separation of the extreme shoulders are suggestive of the "red" (anionic) form of the radical.[50] However, it is possible that the spectrum includes a contribution from proton hyperfine interactions.[48] A mixed form at pH 7.4 would be consistent with a $pK_a = 8.0 \pm 0.2$ for the bovine-heart enzyme.[49]

Heme and Q Contents of the Purified Protein — The molar ratio of FAD to *b*-heme and Q_{10} in the enzyme purified from membranes of ATCC No. 13543 strain was 1: 1.0 ± 0.3: 0.9 ± 0.3 (n = 11 and 5, respectively); thus, the preparations contained 0.9 ± 0.4 Q_{10} per *b*-heme. The number n represents measurements on different enzyme preparations. However, enzyme purified from membranes of PD1222/pPSD100 strain contained 1: 1.3 ± 0.4: 0.1 ± 0.1 (n = 5) FAD: *b*-heme: Q_{10}; or 0.1 ± 0.1 Q_{10} per *b*-heme. The reason for the difference in the Q_{10}-contents of SQR purified from the two strains is unknown at present.

EPR Power-saturation Behavior of the S-3 Center in the Air-oxidized Enzyme — The power-saturation behavior of the (air)oxidized 3Fe-4S cluster has been measured in an attempt to deduce whether a dipolar interaction exists between this iron-sulfur cluster and the *b*-heme. Such magnetic coupling had been postulated,[7] but EPR evidence for this interaction has been lacking.

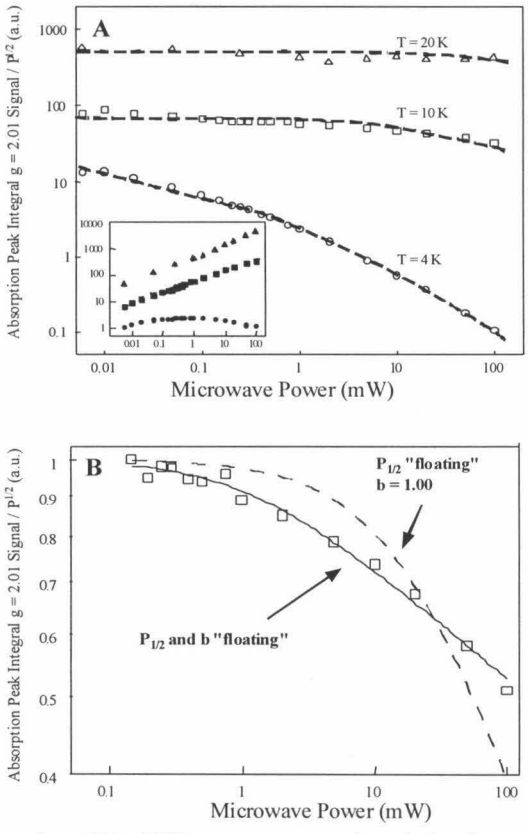

Figure 4. (**A**) EPR power-saturation behavior of the oxidized S-3 center at 4 K, 10 K, and 20 K (ATCC No. 13543 strain). EPR parameters: magnetic field, 330 mT; modulation amplitude, 0.32 mT; modulation frequency, 100 kHz; microwave power, 0.2 mW; microwave frequency, 9.225 GHz; field sweep rate, 0.17 mT s^{-1}; time constant, 0.128 s. The "raw" data (absorption peak-integral versus microwave power) are shown in the *inset*. The $P_{1/2}$-values obtained from the simulated curves are given under "Results." (**B**) Best fits of an empirical equation describing the EPR power-saturation[6] to the 10 K data (**A**); see "Results" and Table 2 for parameter estimates.

Figure 4**A** shows the EPR power-saturation behavior of the S-3 signal in the air-oxidized enzyme. In this state of the enzyme, the cytochrome *b* is the only other center that is paramagnetic (see Table 1). The $P_{1/2}$ values obtained from the computer-generated curves (see "Experimental Procedures") were 0.02 mW, 32 mW and ~200 mW for the data recorded at 4 K, 10 K, and 20 K, respectively. The precision of the double-integrations could have been compromised slightly by the superimposed g_y-component

from the *b*-heme for the 4 K data. The g_y- and g_z-components were broadened beyond detection for $T \geq 9$ K. Using the same analysis, the $P_{1/2}$-values of the S-3 center in the *Bacillus subtilis* enzyme have been reported as 20 mW (5.5 K) and >300 mW (7 K), respectively.[39,51] Thus, interestingly, the spin-relaxation of the 3Fe-4S cluster from the *P. denitrificans* enzyme is significantly slower than that of the *B. subtilis* enzyme, which contains *two b*-hemes.[42]

Figure 4**B** depicts the normalized 10 K power-saturation data from Figure 4**A** and "best fits" of a semi-empirical equation describing the power saturation behavior[6]. The fits were obtained by "floating" the parameters $P_{1/2}$ and b (*solid curve*), or $P_{1/2}$ only (b = 1.00; *dashed curve*) in the regression analysis. The parameter estimates for the 10 K data were $P_{1/2} = 1.1 \pm 0.2$ mW and $b = 0.28 \pm 0.02$ for the *solid curve*, and $P_{1/2} = 18.1 \pm 3.4$ mW for the *dashed curve*; see Table 2 for estimates of the 4 K data.

Table 2. Parameter estimates obtained from best fits of the equation $I = K P^{1/2} [1 + (P / P_{1/2})]^{-b/2}$ to the power-saturation data (P > 0.1 mW) of the S-3 center in the air-oxidized enzyme, and the S-1 and S-3 centers in the succinate- (sred) and dithionite-reduced (dred) enzymes.

Center	$P_{1/2} \pm SE$[a] (mW)	b ± SE	Absorption:Derivative[b]	T (K)
$S\text{-}3_{ox}$	0.21 ± 0.03	0.68 ± 0.01	Absorption	4
$S\text{-}3_{ox}$	1.1 ± 0.2	0.28 ± 0.02	Absorption	10
$S\text{-}3_{sred}$	6.0 ± 1.0	2.07 ± 0.13	Derivative	4
$S\text{-}3_{dred}$	8.2 ± 1.3	1.62 ± 0.08	Derivative	4
$S\text{-}1_{sred}$[c]	0.052 ± 0.018	1.13 ± 0.02	Derivative	4
$S\text{-}1_{dred}$[c]	0.58 ± 0.14	1.16 ± 0.04	Derivative	4
$S\text{-}1_{sred}$	3.9 ± 0.9	1.23 ± 0.07	Derivative	15
$S\text{-}1_{dred}$	25.1 ± 6.8	0.94 ± 0.10	Derivative	15

[a] SE denotes the standard error of the estimate.
[b] Absorption peak integral or derivative signal peak height (g_x-component for the S-1 center).
[c] Fit to data for $P \geq 0.1$ mW.

The effect of the inhomogeneity parameter, b, is to flatten the curve in the region where part of the spins are being saturated; i.e., in the region where P is comparable to $P_{1/2}$. For a purely inhomogeneously-broadened absorption signal (peak integral), b = 1; the purely homogeneously-broadened case yields b = 2. The corresponding values for a derivative-type signal are b = 1 and b = 3, respectively.[29] Thus, it is physically impossible for an isolated spin system to be characterized by b < 1, and such a scenario is therefore diagnostic of a dipolar interaction.[30] As a result, the analysis provides evidence for enhancement of the spin relaxation of the S-3 center due to magnetic coupling with the *b*-heme.

Power-saturation Behavior of the S-3 and S-1 Centers in the Succinate- and Dithionite-reduced Enzymes — Two of the three Fe-S clusters are paramagnetic in both the succinate- and dithionite-reduced samples, namely S-1 (S_T = 1/2) and S-3 (S_T = 2). However, reduction of a sample of SQR with succinate or dithionite yields two distinct levels of reduction. As a result, the redox centers may be diamagnetic or paramagnetic in one or the other state of the enzyme depending on their E_m values (see Table 1 and "Computational Procedures," respectively). Thus, by measuring the power saturation behaviors of the S-1 and S-3 centers in succinate- and dithionite-reduced samples, we expect to observe relief of power-saturation of these centers due to fast-relaxing centers that are coupled to them.

Figure 5 depicts the EPR power saturation behavior of the reduced S-3 (g = 12.6; **A**) and S-1 (g_x = 1.91; **B**) centers in the presence of excess succinate (■) and dithionite (and succinate) (□) at 4 K. The *inset* in **B** shows data obtained on the S-1 center at 15 K.

The dithionite-reduced samples were noted to be less readily power saturated than their succinate-reduced counterparts. Also, the extent of relief of power-saturation is more pronounced for the S-1 center than for the S-3 center (*vide infra*). Since reduction of the S-2 center with dithionite causes it to be paramagnetic (see Figure 2**C** and Table 1), the data demonstrate magnetic couplings between the S-3 and S-2 centers (**A**), and S-1 and S-2 centers (**B**).

In the above we have assumed that the center under observation in the power-saturation experiment is the only paramagnetic center in the succinate-reduced enzyme, and that the S-2 center and the center under observation are the only paramagnetic centers in the dithionite-reduced enzyme. However, this is not the case for SQR (see Table 1). To ascertain the effects of other paramagnetic centers, we therefore calculated the

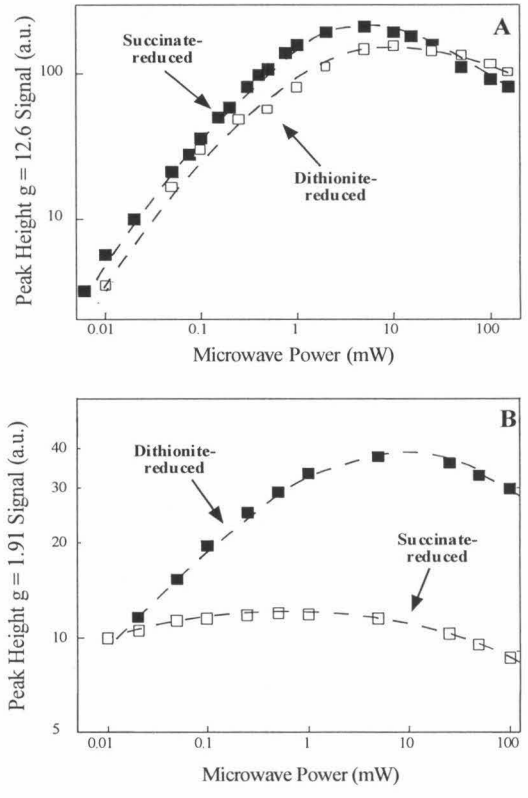

Figure 5. EPR power-saturation behavior of the reduced S-3 (**A**) and S-1 (**B**) centers (ATCC No. 13543 strain). The symbols ■ and □ denote succinate- and dithionite-reduced enzyme, respectively. (**A**) EPR parameters: magnetic field, 50 mT; modulation amplitude, 2.0 mT; modulation frequency, 100 kHz; microwave frequency, 9.229 GHz; field sweep rate, 0.83 mT s^{-1}; time constant, 0.25, temperature 4 K. (**B**) EPR parameters: magnetic field, 345 mT; modulation amplitude, 0.5 mT; modulation frequency, 100 kHz; microwave frequency, 9.229 GHz; field sweep rate, 0.33 mT s^{-1}; time constant, 0.128, temperature 4 K. *Inset* (PD1222/pPSD100 strain), identical EPR parameters, except for temperature, 15 K. The *dashed lines* serve to guide the eye; see Table 2 for estimates of $P_{1/2}$ and b.

fractions of protein-molecules that contained the center under study, as well as each of the other paramagnetic centers, both for the succinate- and dithionite-reduced states of the enzyme (*vide infra*; "Computational Procedures"). Armed with these results, we reconsider our interpretation of the power-saturation curves in Figure 5, **A** and **B**.

When changing from the succinate-reduced state to the dithionite-reduced state of the enzyme, the S-3 center remains reduced, and the *b*-heme and the S-2 center become reduced (see Table 1). The species consisting of S-3_{red} and oxidized *b*-heme (Fe^{3+}), and S-3_{red} and S-2_{red}, decrease and increase by 98% and 100%, respectively (subscript red denotes reduced); thus, S-2_{red} "substitutes" for Fe^{3+} when changing E from -71 mV to < -400 mV in the experiment in Figure 5**A**.

The percentages of enzyme-molecules consisting of S-3_{red} and any of S-1_{red}, Q•, or FAD• also change upon reduction of the succinate-reduced sample with dithionite (10%, 11%, 33%, respectively). However, these changes are inconsequential to the analysis, as radicals are not capable of relaxing a metal-center, and the S-1 center relaxes much slower than the S-3 center at 4 K (see Table 2).

When changing from the succinate-reduced state to the dithionite-reduced state of the enzyme the protein species containing S-1_{red} and Fe^{3+}, and S-1_{red} and S-2_{red} decrease by 89% and increase by 100%, respectively. Thus, in the experiment in Figure 5**B** these enzyme species are also affected most by reduction of the succinate-reduced sample with dithionite.

Enzyme molecules consisting of S-1_{red} and either FAD• or Q• (30% and 10%, respectively), are (again) affected to a lesser extent, and (again) the radicals are not capable of relaxing the iron-sulfur clusters, the 2Fe-2S cluster in this case. The

percentage concentration of the protein species containing S-1_{red} and S-3_{ox} remains essentially unchanged, and therefore, it could not have caused the relief of power-saturation observed in the experiment, either at 4 K or 15 K (inset). However, the species containing S-1_{red} (S_T = 1/2) and S-3_{red} (S_T = 2) increases by 10% upon dithionite-reduction of the sample. Thus, there is a possibility that there is a minor contribution to the relief of power saturation from relaxation enhancement of S-1_{red} by S-3_{red} through a putative magnetic interaction.[52,53] There is precedent for an interaction between the oxidized S-3 center (S_T = 1/2) and the reduced S-1 center in *Micrococcus luteus*[54] and *B. subtilis*.[55]

Taken together, the *minor* relief of power-saturation of the succinate-reduced S-3 center upon reduction of the sample with dithionite (Figure 5**A**) may be due to substituting the *b*-heme with the S-2 center as the interacting partner. However, it remains possible that the S-2 center is more efficient at relaxing the S-1 center, than it is at relaxing the S-3 center. This scenario would also result in minor relief of power-saturation.

In the case of the S-1 center (Figure 5**B**), there is *substantial* relief of power-saturation due to the S-2 center becoming paramagnetic in the dithionite-reduced state of the enzyme. This observation suggests that the 2Fe-2S cluster is not coupled to the *b*-heme. This finding is consistent with the topology of this iron-sulfur cluster within the IP [see Figure 10 in ref. 7].

Discussion

In the present work we have characterized the EPR signals observed in air- and ferricyanide-oxidized, and succinate- and dithionite-reduced SQR purified from *P. denitrificans.* We have focussed in particular on elucidating the magnetic interactions operating between the metal centers, and simulating the EPR signals from the radicals.

EPR Fingerprinting Studies — Bacterial respiratory chains are generally dominated by features originating from SQR.[44,56] As a general comparison, we obtained spectra of membranes from a *P. denitrificans* strain (PD1222/pPSD100) overproducing SQR (Figures 1 and 3**F**). These spectra were highly similar to those of the purified enzyme (Figures 2 and 3**A**; ATCC No. 13543 strain) at the three levels of reduction of the protein. Therefore, we conclude that the purified enzyme has been prepared in its native state.

EPR Spectral Simulations of the Radical Signals — The two Q• in the FAD•-2Q• simulations were taken to be isolated spins; i.e., no dipolar interaction between them needs to be included. Since a dipolar-coupled signal is observed for the Q•-pair in the bovine-heart enzyme[3,4,45-47,57] and that of a variety of higher plants,[5] it may be expected that such an interaction would also operate in the *P. denitrificans* enzyme. However, we predict a maximal spin-concentration of 55% Q•:FAD at E = 5 mV (i.e., ($E_m^{Q/Q\bullet}$ + $E_m^{Q\bullet/QH_2}$)/2) instead of 11%[5] as determined from the spin-concentration and EPR simulations of the ATCC No. 13543 strain. Thus, (redox) poising the enzyme with a large excess of succinate (E ≈ -71 mV) is most likely not optimal for eliciting substantial

spin-concentrations of Q•. This may also be the main reason for the signal being well simulated by two *non*-interacting Q. In addition, the sample with the full complement of Q (Q_2) has less Q•:Q (see Figure 3, **A** and **C**) than the sample with 0.7 Q (Q_{10}):FAD. This result suggests that the enzyme has greater affinity (lower K_d) for the native Q_{10}.

Power-saturation Behavior of the S-3 center in the Air-oxidized Enzyme — The analysis used in Figure 4**B** provides evidence for a magnetic interaction between the cytochrome *b* and the S-3 center in their respective oxidized states; see Results. In the following, we shall argue that Figure 4**A** also presents evidence for the interaction.

The analysis used in Figure 4**A** corrects for extended sample geometry, unlike the one used in Figure 4**B**. That is, the magnetic component of the microwave magnetic field is not constant inside the EPR cavity, and this is corrected for by sampling (averaging) the field over the dimensions of the cavity. It is evident from Figure 4**A** that inclusion of such a correction term in the (analytical) equation[27,28] accommodates some of the "flattening" (inhomogeneity) effect for $P \approx P_{1/2}$ (see also "Results"). However, upon closer inspection of the 10 K data, it becomes clear that it does so less well than the empirical fit[6] with b = 0.3 (*solid line* in Figure 4**B**). Notably, however, the curve to the 10 K data in Figure 4**A** was simulated assuming a 100% gaussian distribution for the individual spin-packet line-shapes; i.e., 100% inhomogeneous broadening. Using < 100% inhomogeneous broadening resulted in a worse fit. In this regard, it is worth considering that one phenomenon giving rise to inhomogeneous broadening, is a dipole-dipole interaction between non identical centers.[27] Thus, taken together, both analyses provide evidence for the fact that the spin-relaxation of the oxidized 3Fe-4S is enhanced

by a (weak) dipolar interaction provided by the fast-relaxing spin of the *b*-heme (oxidized).

Previous indirect evidence obtained on the bovine-heart enzyme also points to the S-3 center being proximal to the *b*-heme. The sensitivity of the S-3 center in SDH to molecular oxygen[58] is consistent with our evidence for a magnetic interaction between the *b*-heme and the 3Fe-4S cluster.

Estimation of the Inter-center Distance Between the S-3 Center and the b-heme in the Air-oxidized Enzyme — From the absence of observable (~0.5 mT) splittings in the g = 2.01 signal, a lower limit of ~1.8 nm between the 3Fe-4S cluster and the *b* heme may be estimated assuming dipolar coupling[7].[7,52] However, these splittings may be obscured due to the large anisotropy of the *b*-heme signal and the relative orientations of the principal axes of the two centers with respect to each other and the magnetic field. A significant exchange-interaction (J) may be excluded, as it could not have resulted in a "signature" signal for an oxidized 3Fe-4S cluster, namely g_{av}-value = 2.01 [where $g_{av} = (g_x + g_y + g_z) / 3$].[59] Therefore, we estimate a distance (r) of $0.5 < r \leq 2$ nm.

The Magnitude of the Zero-field Splitting Parameters of the S-3 center in the Reduced Enzyme — In samples reduced with excess succinate and dithionite, we observed for the first time for SQR or QFR a spectral feature originating from a reduced

---

[7] $H_{eff} = \pm\ 3/2\ \mu_0^2 / r^3\ (1 - 3\cos^2\theta)$, where H_{eff} is the (classical) effective magnetic field splitting by two interacting equivalent electron dipole moments, and μ_0 denotes the permeability of vacuum.[52] Thus, we have $H_{eff} \propto 3/2\ \mu_0^2 / r^3$ from which an inter-center distance of ~1.8 nm is estimated for splittings of 0.5 mT.

3Fe-4S cluster ($S_T = 2$; see Table 1). The resonance is observed at low-field ($g \approx 13$), and is consistent with a $\Delta M_S = 4$ transition within the reduced cluster.[43] Observation of (part of) such a 'quarter-field' resonance at X-band implies that $\Delta \approx 0.3$ cm^{-1}, where Δ is the energy splitting between the $M_S = \pm 2$ ground state levels.[60,61] From similar observations on natural and synthetic cuboidal 3Fe-4S clusters (see Table 6 in ref. 62) and a suitable spin Hamiltonian[8], we may estimate $D \approx -2.5$ cm^{-1} and E/D = 0.20-0.25, respectively, where D, and E denote the axial and rhombic zero-field splitting parameters, respectively.

Power-saturation Behavior of the S-3 and S-1 Centers in the Succinate- and Dithionite-reduced Enzymes — The relief of power-saturation of the S-3 and S-1 centers upon reduction of the succinate-reduced samples with dithionite (Figure 5) has been taken as evidence for weak dipolar interactions between the centers in question and the S-2 center. Similar decreases in the T_1's of succinate-reduced S-1 centers upon reduction with dithionite have been observed in bovine-heart SQR,[38] *B. subtilis* succinate:menaquinone reductase,[39] and *E. coli* fumarate reductase.[40] A magnetic interaction between the reduced S-2 and S-3 centers has also been inferred from soluble (SDH) preparations partially or almost completely devoid of 3Fe-4S cluster.[1]

---

[8] $\hat{H}_e = D[\hat{S}_z^2 - 1/3\ S(S+1) + E/D(\hat{S}_x^2 + \hat{S}_y^2)] + \beta_e \mathbf{B} \cdot \mathbf{g_e} \cdot \mathbf{S}$. Assuming the Zeeman interaction is isotropic ($g_e \approx 2$), and $|D| \gg g_e \beta_e B$, each Kramers' doublet may be treated separately, assuming a 'fictitious' spin **S'** = 1/2. The splitting D of the levels lowest in energy ($M_s = \pm 2$) puts a constraint on the axial (D) and rhombic (E) zero-field splitting parameters, namely $D = 2D(x^{1/2} - 1)$, where $x = [1 + 3(E/D)^2]$.[60-62]

Conclusions

In this work we have shown that the fingerprinting spectra obtained on the *P. denitrificans* enzyme are largely similar to those of the bovine-heart enzyme, with the exception of the Q• signals. It has been demonstrated by EPR simulation that *P. denitrificans* SQR binds two Q•; however, their E_m values are ~100 mV lower than in the bovine-heart enzyme. A weak dipolar interaction between the S-3 center and the *b*-heme in the oxidized enzyme has been revealed by power saturation experiments. A similar magnetic interaction may exist in the reduced enzyme, as revealed by power-saturation data obtained on the succinate- and dithionite-reduced samples and redox calculations. This is the first evidence obtained on the intact complex for a close proximity of these two centers. Taken together, these EPR data are entirely consistent with the topological picture postulated by Ohnishi; see Figure 10 in ref. 7. That is, the three iron-sulfur clusters are located in the IP within 2 nm of each other, and the S-3 center is the iron-sulfur cluster in closest proximity (≤ 2 nm) to the *b*-heme in the QP.

References

(1)Ackrell, B. A. C.; Johnson, M. K.; Gunsalus, R. P.; Cecchini, G. *Structure and function of succinate dehydrogenase and fumarate reductase*; Müller, F., Ed.; CRC Press: Boca Raton, 1992; Vol. III, pp 229-297.

(2)Hederstedt, L.; Ohnishi, T. *Progress in succinate:quinone oxidoreductase research*; Ernster, L., Ed.; Elsevier Science Publishers: Amsterdam, 1992, pp 163-198.

(3)Ruzicka, F. J.; Beinert, H.; Schepler, K. L.; Dunham, W. R.; Sands, R. *Proc. Natl. Acad. Sci. U. S. A.* **1975**, *72*, 2886.

(4)Ingledew, W. J.; Salerno, J. C.; Ohnishi, T. *Arch. Biochem. Biophys.* **1976**, *177*, 176.

(5)Rich, P. R.; Moore, A. L.; Ingledew, W. J.; Bonner, W. D. *Biochim. Biophys. Acta* **1977**, *462*, 501.

(6)Pennoyer, J. D.; Ohnishi, T.; Trumpower, B. L. *Biochim. Biophys. Acta* **1988**, *935*, 195.

(7)Ohnishi, T. *Curr. Top. Bioenerg.* **1987**, *15*, 37.

(8)Cammack, R.; Maguire, J. J.; Ackrell, B. A. C. *Mechanisms of electron-transfer in succinate dehydrogenase and fumarate reductase: possible functions for iron-sulphur centre 2 and cytochrome b*; Papa, S., Chance, B. and Ernster, L., Ed.; Plenum Press: New York, 1987, pp 485-491.

(9)Salerno, J. C. *Biochem. Soc. Trans.* **1991**, *19*, 599-605.

(10)Albracht, S. P.; Van Verseveld, H. W.; Hagen, W. R.; Kalkman, M. L. *Biochim. Biophys. Acta* **1980**, *593*, 173.

(11)Yang, D. C.; Oyaisu, H.; J., O. G.; Woese, C. R. *Proc. Natl. Acad. Sci. U. S. A.* **1985**, *82*, 4443.

(12)John, P.; Whatley, F. R. *Nature* **1975**, *254*, 495.

(13)Stowell, M. H. B.; Larsen, R. W.; Winkler, J. R.; Rees, D. C.; Chan, S. I. *J. Phys. Chem.* **1993**, *97*, 3054.

(14)Berry, E. A.; Trumpower, B. L. *J. Biol. Chem.* **1985**, *260*, 2458.

(15)Steffens, G. C. M.; Pascual, E.; Buse, G. *J. Chromatogr.* **1990**, *521*, 291.

(16)Wilson, D. F.; King, T. E. *J. Biol. Chem.* **1964**, *239*, 2683.

(17)Berry, E. A.; Trumpower, B. L. *Anal. Biochem.* **1987**, *161*, 1.

(18)Trumpower, B. L.; Simmons, Z. *J. Biol. Chem.* **1979**, *254*, 4608.

(19)Redfearn, E. R. *Meth. Enzymol.* **1967**, *10*, 381.

(20)Hatefi, Y.; Galante, Y. M. *J. Biol. Chem.* **1980**, *255*, 5530.

(21)Orme-Johnson, N. R.; Orme-Johnson, W. H. *Meth. Enzymol.* **1978**, 252.

(22)Eriksson, L. E. G.; Ehrenberg, A. *Biochim. Biophys. Acta* **1973**, *293*, 57.

(23)Wolfram, S. *Mathematica*; Addison-Wesley: Redwood City, 1994.

(24)Bonomi, F.; Pagani, S.; Cerleti, P.; Giori, C. *Eur. J. Biochem.* **1983**, *134*, 439.

(25)Maguire, J. J.; Johnson, M. K.; Morningstar, J. E.; Ackrell, B. A. C.; Kearney, E. B. *J. Biol. Chem.* **1985**, *260*, 10909.

(26)Ohnishi, T.; Lim, J.; Winter, D. B.; King, T. E. *J. Biol. Chem.* **1976**, *251*, 2105.

(27)Blum, H.; Ohnishi, T. *Biochim. Biophys. Acta* **1980**, *621*, 9.

(28)Castner, T. G. *Phys. Rev.* **1959**, *115*, 1506.

(29)Sahlin, M.; Gräslund, A.; Ehrenberg, A. *J. Magn. Reson.* **1986**, *67*, 135.

(30)Galli, C.; Innes, J. B.; Hirsh, D. J.; Brudvig, G. W. *J. Magn. Reson.* **1996**, *B110*, 284.

(31)Ackrell, B. A. C.; Kearney, E. B.; Mims, W. B.; Peisach, J.; Beinert, H. *J. Biol. Chem.* **1984**, *259*, 4015.

(32)Morningstar, J. E.; Johnson, M. K.; Cecchini, G.; Ackrell, B. A. C.; Kearney, E. B. *J. Biol. Chem* **1985**, *260*, 13631.

(33)De Vries, S.; Albracht, S. P. J. *Biochim. Biophys. Acta* **1979**, *546*, 334.

(34)Salerno, J. C. *J. Biol. Chem.* **1984**, *259*, 2331.

(35)Moore, G. R.; Williams, R. J. P.; Peterson, J.; Thomson, A. J.; Mathews, F. S. *Biochim. Biophys. Acta* **1985**, *829*, 83.

(36)Sucheta, A.; Ackrell, B. A. C.; Cochran, B.; Armstrong, F. A. *Nature* **1992**, *356*, 361.

(37)Beinert, H.; Ackrell, B. A. C.; Kearney, E. B.; Singer, T. P. *Eur. J. Biochem.* **1975**, *54*, 185.

(38)Ohnishi, T.; Salerno, J. C.; Winter, D. B.; Lim, J.; Yu, C.-A.; Yu, L.; King, T. E. *J. Biol. Chem.* **1976**, *251*, 2094.

(39)Hederstedt, L.; Maguire, J. J.; Waring, A. J.; Ohnishi, T. *J. Biol. Chem.* **1985**, *260*, 5554.

(40)Johnson, M. K.; Morninstar, J. E.; Cecchini, G.; Ackrell, B. A. C. *Biochem. Biophys. Res. Commun.* **1985**, *131*, 756.

(41)Yu, L., Xu, J.-X., Haley, Paul E., and Yu, C.-A. *J. Biol. Chem.* **1987**, *262*, 1137.

(42)Hägerhäll, C.; Aasa, R.; von Wachtenfeldt, C.; Hederstedt, L. *Biochemistry* **1992**, *31*, 7411.

(43)Hagen, W. R.; Dunham, W. R.; Johnson, M. K.; Fee, J. A. *Biochim. Biophys. Acta* **1985**, *828*, 369.

(44)Anemüller, S.; Hettmann, T.; Moll, R.; Teixeira, M.; Schäfer, G. *Eur. J. Biochem.* **1995**, *232*, 563.

(45)Salerno, J. C.; Ohnishi, T. *Biochem. J.* **1980**, *192*, 769.

(46)Ohnishi, T.; Trumpower, B. L. *J. Biol. Chem.* **1980**, *255*, 3278.

(47)Miki, T.; Yu, L.; Yu, C. *Arch. Biochem. Biophys.* **1992**, *293*, 61.

(48)Hyde, J. S.; Eriksson, L. E. G.; Ehrenberg, A. *Biochim. Biophys. Acta* **1970**, *222*, 688.

(49)Ohnishi, T.; King, T. E.; Salerno, J. C.; Blum, H.; Bowjer, J. R.; Maida, T. *J. Biol. Chem.* **1981**, *256*, 5577.

(50)Edmondson, D. E.; Ackrell, B. A. C.; Kearney, E. B. *Arch. Biochem. Biophys.* **1981**, *208*, 69.

(51)Hägerhäll, C.; Sled, V.; Hederstedt, L.; Ohnishi, T. *Biochim. Biophys. Acta* **1995**, *1229*, 356.

(52)Abragam, A.; Bleaney, B. *Electron paramagnetic resonance of transition ions.*; Dover Publications, Inc.: New York, 1986.

(53)Cammack, R.; Williams, R.; Guigliarelli, B.; More, C.; Bertrand, B. *Biochem. Soc. Trans.* **1994**, *22*, 721.

(54)Crowe, B. A.; Owen, P.; Patil, D. S.; Cammack, R. *Eur. J. Biochem.* **1983**, *137*, 191.

(55)Maguire, J. J.; Magnusson, K.; Hederstedt, L. *Biochemistry* **1986**, *25*, 5202.

(56)Hurst, J. K.; Barrette, W. C.; Michel, B. R.; Rosen, H. *Eur. J. Biochem.* **1991**, *202*, 1275.

(57)Salerno, J. C.; Harmon, H. J.; Blum, H.; Leigh, J. S.; Ohnishi, T. *FEBS Lett.* **1977**, *82*, 179.

(58)Ohnishi, T.; Winter, D. B.; Lim, J.; King, T. E. *Biochem. Biophys. Res. Commun.* **1974**, *61*, 1017.

(59)Beinert, H.; Thomson, A. J. *Arch. Biochem. Biohys.* **1983**, *222*, 333.

(60)Moura, I.; Macedo, A.; Moura, J. J. G. *EPR of Iron-sulfur and Mixed Metal Clusters in Proteins*; Hoff, A. J., Ed.; Elsevier: Amsterdam, 1989, pp 813.

(61)Papaefthymiou, V.; Girerd, J.-J.; Moura, I.; Münck, E. *J. Am. Chem. Soc.* **1987**, *109*, 4703.

(62)Zhou, J.; Hu, Z.; Münck, E.; Holm, R. H. *J. A. Chem. Soc.* **1996**, *118*, 1966.

(63)Matsson, M.; Ackrell, B. A. C.; Cochran, B.; Hederstedt, L. *Arch Microbiol* **1998**, *170*, 27.

Chapter 3:

Electron Spin-Lattice Relaxation Measurement of the 3Fe-4S (S-3) Cluster in Succinate:Ubiquinone Reductase from *Paracoccus denitrificans*: A Detailed Analysis Based on a Dipole-Dipole Interaction Model

Abstract

The electron spin-lattice relaxation for the 3Fe-4S (S-3) center in Succinate:Ubiquinone Reductase has been examined using both inversion recovery and 'picket-fence' pulse sequences at a temperature range of 4-8K. The latter pulse sequence is used to eliminate the interference of spectral diffusion in frozen solids. An abnormally fast relaxation was observed for the S-3 center. We attribute this rapid relaxation to a magnetic dipolar interaction between the S-3 center and a nearby paramagnetic *b*-heme (cytochrome *b*). A model has been developed to treat the interaction between two paramagnetic redox centers in a rigid lattice at a fixed distance apart but with random orientations in a magnetic field. Both the contribution to the spin-lattice relaxation rate from the dipolar interaction ($k_{1\theta}$), which is anisotropic, and the intrinsic electron spin relaxation, which is scalar ($k_{1scalar}$), have been deduced. We find that the contribution of exchange interaction to the anisotropic part of the relaxation rate ($k_{1\theta}$) is very small. Accordingly, we conclude that $k_{1scalar}$ is dominated by the intrinsic electron spin-lattice relaxation. From $k_{1\theta}$, a lower limit ($r > 10$ Å) has been deduced for the distance between the S-3 center and the *b*-heme.

Introduction

Succinate:Ubiquinone Oxidoreductase (SQR; complex II) links the oxidation of succinate to fumarate in the Kreb's cycle to the reduction of quinone to quinol in the respiratory chain in aerobic cells. The SQR from *Paracoccus denitrificans* contains four subunits, a flavoprotein (FP), an iron-sulfur protein (IP), and two hydrophobic polypeptides (QP).[1,16,17,25] The FP contains the dicarboxylate binding site and a covalently bound flavin moiety (FAD). Three iron-sulfur clusters, of type 2Fe-2S, 4Fe-4S, and 3Fe-4S, are part of the IP; these are often referred to as S-1, S-2, and S-3, respectively. Together, the FP and IP subunits constitute the succinate dehydrogenase activity (SDH) of the complex. In SQR, this soluble domain is anchored to the plasma membrane by the two hydrophobic polypeptides (QP). The QP binds one molecule of *b*-heme[26,32] and consists of two quinone binding sites.[32]

In the air-oxidized SQR, the S-3 center and *b*-heme are the only redox centers that are paramagnetic. Both centers are fully oxidized, as was determined in our earlier electron paramagnetic resonance (EPR) studies.[32] The S-3 center exhibits a prominent and almost isotropic EPR signal at g = 2, which may be used as an endogenous probe for the paramagnetic *b*-heme. Previous indirect evidence obtained on the bovine heart enzyme has pointed to the S-3 center being proximal to the *b*-heme.[25] Recently, we studied the electron spin relaxation properties of the S-3 center from *Paracoccus denitrificans* by cw EPR power saturation experiments.[32] Enhanced relaxation of S-3 was observed and taken as an evidence of the dipolar interaction between the S-3 and *b*-

heme. An upper limit of the distance (r) between the S-3 and *b*-heme was inferred from the power saturation results ($r \leq 20$ Å).

This study is concerned with a more reliable estimate of the distance between the S-3 and *b*-heme in SQR. We exploit the effect of the dipolar and exchange interactions between the interacting spins and the dependence on electron spin-lattice relaxation rate of the more slowly relaxing S-3 center on these interactions to deduce the distance of the S-3 center from the neighboring *b*-heme.

Several methods have been used for measuring the electron spin-lattice relaxation. One is saturation recovery, in which a long saturating microwave pulse is applied to the entire spin system to drive it into a state away from equilibrium during the preparation period prior to observation of its recovery. This is the most widely used method, as this kind of measurement is not compromised by spectral diffusion in frozen solid provided that the whole spectrum can be excited.[12] Electron spin-lattice relaxation rates are often determined by the inversion recovery method as well. Unfortunately, even for the most modern pulsed EPR instruments, the typical microwave field magnitudes are insufficient to saturate or invert the entire EPR spectrum of the S-3 center. As a result, the evolution of a perturbed EPR line toward equilibrium is driven by both the intrinsic spin-lattice relaxation process as well as the redistribution of the initial perturbation across the non-uniformly perturbed system.

In this paper, we implement the 'picket-fence' pulse sequence in the inversion recovery experiment in order to exclude the influence of spectral diffusion on the

observed recovery traces.[19] This pulse sequence allows us to obtain a more uniform initial perturbation[10,21] of the EPR spectrum of the S-3 center.

We find that, even under these conditions, the S-3 center exhibits spin-lattice relaxation behavior that deviates markedly from exponentiality. This is the result expected from the dipolar interaction between the S-3 center and the *b*-heme for a powder sample. Equations have been developed to describe the recovery traces of a "slow" relaxing spin when its spin-lattice relaxation is perturbed by pairwise interaction with a "fast" relaxing spin.[18,27] This treatment allows us to separate the orientation-dependent and isotropic contributions to the spin-lattice relaxation. We use this approach to obtain a more reliable estimate of the distance between the S-3 center and the *b*-heme in SQR.

Experimental Procedures

Materials — Triton X-100; Poly(ethylene glycol) tert-octylphenyl ether; Tris(hydroxymethyl)aminomethane, Tris; and poly(oxyethylene) lauryl ether[30] were purchased from Boehringer Mannheim Corp., IN, or Mannheim, Germany. Centricon ultrafiltration tubes were from Amicon Inc., Beverly, MA; Sephadex G-50 was purchased from Sigma Chemical Co., St Louis, MO; Amberlite XAD-2 adsorbent was from Serva, Heidelberg, Germany. All other reagents were of AR grade.

Cell Growth, Enzyme Purification, and Analytical Procedures — Growth conditions for the strain PD1222/pPSD100 containing overproduced (~2-fold) SQR and

its construction have been described elsewhere.[24] SQR was purified by thawing the stored cell packs using 150-200 g of material each time. The purification procedure was as described previously,[26] with modifications similar to those described in ref. 5,29. Prior to the EPR experiments, the enzyme was concentrated and the salt and Triton X-100 concentrations were reduced, the latter to ~0.05 % (w/v), by repeated exchange in Centricon 100 kDa cutoff concentrators against 100 mM Hepes, pH 7.4. The final yield was 1-2 ml of 50-100 μM SQR. The enzyme was considered to be sufficiently pure for use in our experiments according to two criteria: (i) optical spectra (negligible absorption from hemes other than b_{557}); and (ii) SDS-PAGE (> 90%).[26] Enzyme concentrations were determined by measuring the acid-nonextractable FAD content of the samples.[33] Cytochrome *b* concentrations were determined from dithionite reduced-minus-oxidized difference spectra in a pyridine hemochrome assay mixture, using $\Delta\varepsilon_{557\text{-}540} = 24.0\ mM^{-1}\ cm^{-1}$.[6] Typical [cytochrome *b*]/[FAD] ratios in our preparations were 1.3 ± 0.4. Samples stored at 193 K were thawed on ice before the pulsed EPR experiments. The concentration of SQR samples in the EPR experiments was ~ 50 μM.

EPR Methods — The pulsed EPR experiments at X-band were conducted on a home-built instrument in the laboratory of Prof. R. D. Britt at UC-Davis.[31] The electron spin lattice relaxation rates were measured with the picket-fence pulse sequence $\{\pi - \tau_{pf} - \pi - \tau_{pf} \ldots \pi - T - \pi/2 - \tau - \pi - ESE\}$.[10,11] The pulse sequence was generated by a 0.1 ms clock. In this experiment, π pulses of ca. 20 ns were applied during a period of 0.1 ms and the inter-pulse times (τ_{pf}) between these π pulses are 1 μs. Echo intensity was

monitored at time intervals T following the picket-fence pulses. The one picket pulse experiment is exactly equivalent to the standard inversion recovery experiment.[3,23] The interpulse time τ of 210 ns was used. The microwave power was 35 watts at 9.26 GHz. The magnetic field was set at 3292 G (the resonance field corresponding to the absorption maximum of the signal of oxidized S-3).

In the picket-fence pulse sequence, many 180-degree pulses are sent in succession. Although spectral diffusion may compete with spin-lattice relaxation in filling in the hole created by an initial inversion pulse, in principle, with the application of many subsequent pulses, the entire spectral region in rapid spectral diffusional contact with the on-resonance bandwidth will be driven away from equilibrium, with only spin-lattice relaxation acting to drive the system back to the pre-pulse equilibrium. The result is a saturated spectrum from which the contribution of spectral diffusion to the spin-lattice relaxation is excluded.[4]

To measure T_2 of the *b*-heme, a 2-pulse transverse relaxation experiment (sequence equivalent to 2-pulse ESEEM) was performed. A $\pi/2$ - τ - π - τ - echo sequence was used. The time for a $\pi/2$ pulse was 10 ns. Echo decays were recorded starting at 150 ns with 5 ns increment. Only data at 4.2 K were obtained due to the fast relaxing nature of the *b*-heme. The time constant for the ESE decay is referred to as T_m to encompass all processes that result in echo dephasing. The values obtained directly from these experiments are typically cited as the decay time constant. It is assumed that instantaneous diffusion makes a negligible contribution to the dephasing process, so T_m can be a reasonable estimate of T_2.

The temperature of the EPR sample was determined and controlled with a Lake Shore Cryotronics Model 805 temperature controller, which samples the resistance of a Lake Shore Cryotronics TG-120P gallium-aluminum-arsenide diode sensor mounted near the sample position of an X-band pulsed EPR probe inserted in the variable-temperature sample chamber of a Janis Supervaritemp liquid He cryostat. The system stabilizes the temperature at a set value by controlling the temperature of the cold He gas introduced into the sample chamber.[23]

Results

The field swept EPR spectrum of air-oxidized SQR (~ 50 μM) at 4K is shown in Figure 1. For the spin-lattice relaxation measurements, the magnetic field was set to the position marked by arrow (3292 G). This signal was characterized in our earlier work[32] as an isotropic signal arising from the oxidized S-3 center superimposed with a very weak and broad g_y- component of the *b*-heme.[32]

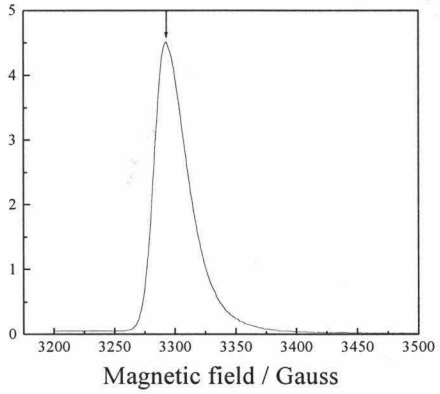

Figure 1. Field swept EPR absorption spectrum of air-oxidized SQR detected by spin-echo method with microwave frequency: 9.26 GHz. The spectral width of a 20 ns π pulse is approximately 18 G. The concentration of SQR in this sample is ~ 50 μM.

Figure 2 presents examples of the inversion-recovery [π - T - π/2 - τ - π - ESE] transients observed at different temperatures. The recovery traces are clearly non-exponential. These inversion recoveries could be fitted to a sum of two exponentials,

with decay constants equal to T_s and T_f, as highlighted for each panel. There are several possible reasons for this abnormal recovery behavior. First, the presence of a chemically distinct species at the same resonant field position could produce a bi-exponential recovery for this g = 2 signal.[32] However, magnetic dipolar interaction could also be the cause of this non-exponential behavior. Finally, this behavior could also arise from spectral diffusion. In order to eliminate the contribution of spectral diffusion to the relaxation transient, we have recorded the relaxation recovery using the picket-fence pulse sequence.

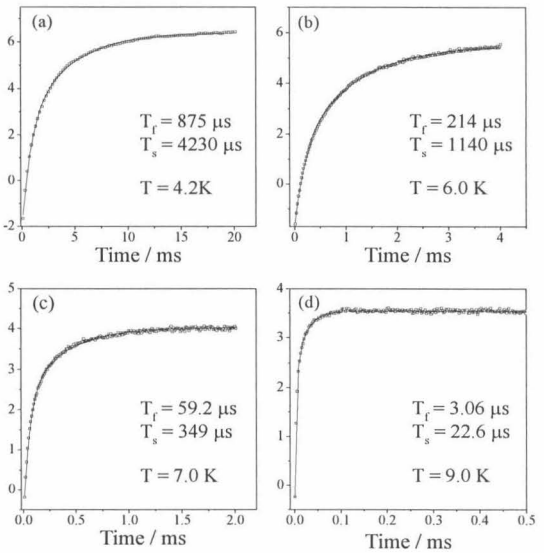

Figure 2. Inversion-recovery traces for the S-3 (3Fe-4S) center at different temperatures: (a) 4.2 K; (b) 6.0 K; (c) 7.0 K; (d) 9.0 K. The solid lines are obtained by fitting the data to a sum of two exponentials and the two decay constants, T_f and T_s, are provided in each panel.

Elimination of Spectral Diffusion — The dependence of the effective electron spin-lattice relaxation rates for the S-3 center on the number of picket-fence pulses at 4K is shown in Figure 3. Here the effective spin-lattice relaxation rate is measured by the time when the magnetization has decayed to 1/e of its initial value assuming that the decay is exponential. Not surprisingly, this effective relaxation rate decreases with the

number of picket-fence pulses and begins to level off as the number of picket-fence pulses is increased to 100. Thus, indeed, spectral diffusion is contributing to the original decay, but it can be effectively excluded by the use of the picket-fence pulse sequence. As a control, we have studied the relaxation of $CuSO_4$ in aqueous solution at 4K using both inversion-recovery and picket-fence pulse sequences. A single exponential decay of the magnetization following elimination of spectral diffusion by the picket-fence sequence was observed (Figure 4). We have used $CuSO_4$ here as a control because Cu^{2+} is known to exhibit bi-exponential recovery due to spectral diffusion.

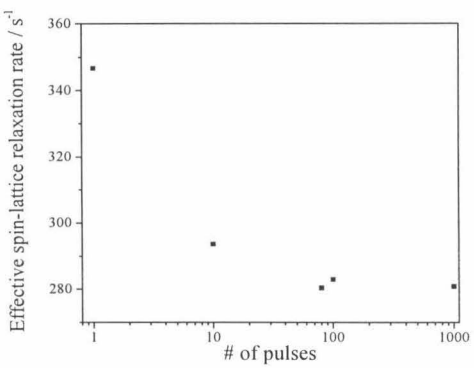

Figure 3. Dependence of the effective spin-lattice relaxation rate at 4 K for the S-3 center of SQR on the number of the picket-fence pulses.

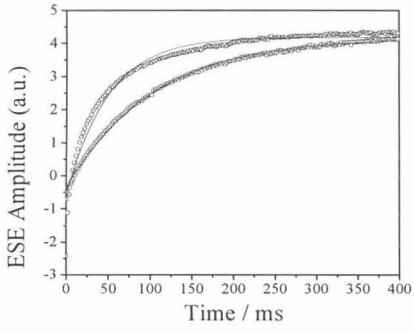

Figure 4. The picket-fence experiment of the Cu^{2+} ion (2 mM) at 4.2 K. One picket-fence pulse (inversion recovery) data (open circle) and data of 100 picket-fence pulse experiment (open rectangular) are superimposed with the single exponential fits (solid line).

We have applied the picket-fence sequence (100 pulses) to record recovery traces of the S-3 center in SQR over a temperature range of 4-8 K and these data are shown in Figure 5 along with fits to the data as described below.

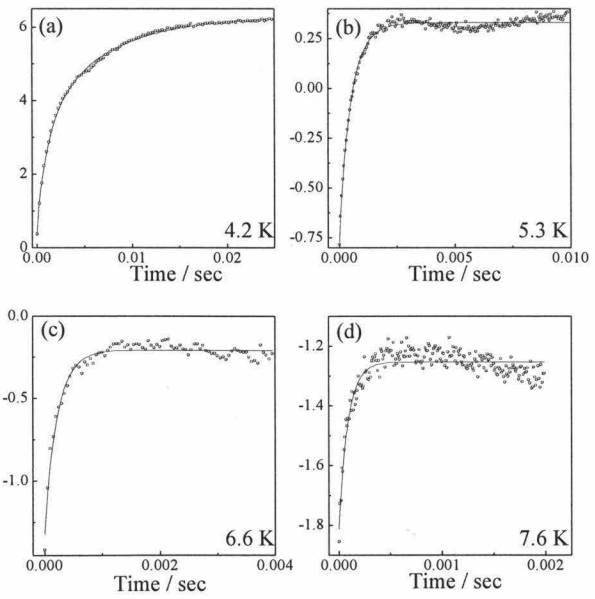

Figure 5. The recovery traces of the S-3 center (obtained by 100 picket-fence pulses) and the corresponding simulated curve using eq 13 at four different temperatures: (a) 4.2 K; (b) 5.3 K; (c) 6.6 K; (d) 7.6 K.

Anomalous Spin-lattice Relaxation of the S-3 Center — We found that the recovery trace remains nonexponential at 4K (Figure 6) even after the spectral diffusion effect is excluded by use of the picket-fence sequence. We surmise that this nonexponential recovery arises either from spectral interference from an overlapping signal, or from dipolar interaction with another

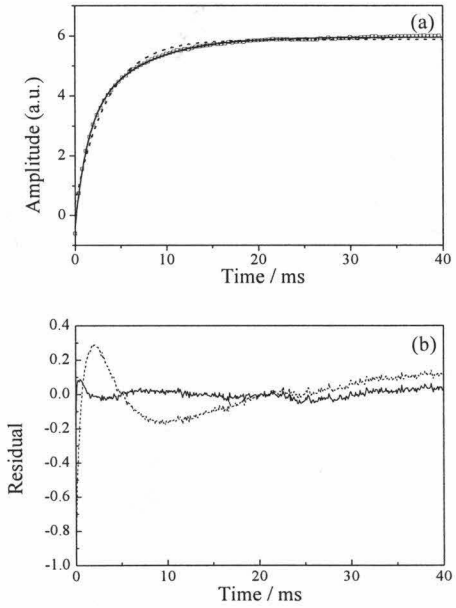

Figure 6. (a) The picket-fence data of the S-3 center at 4.2 K (open circle) obtained by 1000 π pulses superimposed with single-exponential (dashed line) and bi-exponential (solid line) fits. (b) The residual of single-exponential (dashed line) and bi-exponential (solid line) fit.

magnetic center that is relaxing rapidly.

If the non-exponential behavior is caused by the superposition of the S-3 signal and the signal of *b*-heme at g = 2 ($g_y^{b\text{-heme}}$ = 2.1),[32] presumably a bi-exponential model can be used to describe it. The recovery trace is fitted by a bi-exponential in Figure 6 and the fitting parameters are shown in Table 1. As reported in our previous study,[32] the *b*-heme has a very broad and weak signal at g_y = 2.1 and a small signal at g_z = 3.6 (at least 200 times smaller in magnitude than the S-3 signal). It is also expected to have a faster relaxation rate compared to the S-3 center. However, as shown in Table 1, the difference between the faster relaxation rate (T_f) and slower relaxation rate (T_s) constants is within one order of magnitude. Also, the signal intensity of the *b*-heme is much smaller than that of the S-3 center.[32] The weights (C_f and C_s in Table 1) of these two relaxation rates are expected to be very different, but they are not. Therefore, we have excluded the possibility of a significant *b*-heme contribution to the inversion recovery.

Table 1. Time constants and fitting coefficients for the recovery traces of the S-3 center at 4 K using the bi-exponential[a] and single exponential[b] models[c].

# of pulses	bi-exponential					single exponential	
	T_f (ms)	T_s (ms)	C_f	C_s	R^2	T_1 (ms)	R^2
1	0.7298	4.4704	3.4046	4.8365	0.99939	2.8847	0.98547
10	1.1178	5.2910	2.8166	3.2455	0.99927	3.4058	0.98756
80	0.8674	6.9325	2.9489	3.3616	0.99907	3.5667	0.97503
100	1.4941	6.3189	3.4360	2.8257	0.99937	3.5347	0.98782
1000	1.2534	5.9431	3.2079	3.1731	0.99940	3.5604	0.98619

[a] $M_0 - C_f \exp(-t/T_f) - C_s \exp(-t/T_s)$

[b] M_0-C exp $(-t/T_1)$

[c] M_0, C_f, C_s, and C are fitting parameters; T_f and T_s are the fast and slow relaxation time constants, respectively; T_1 is the effective spin-lattice relaxation time constant.

Instead, we have attributed the anomalous relaxation behavior of the S-3 center to a tensor magnetic dipolar interaction between the S-3 center and the low-spin *b*-heme. This interaction produces a "powder" distribution of spin-lattice relaxation rates, and thus the composite decay should not be exponential. A similar non-exponential recovery is apparently not observed for the magnetically isolated 3Fe-4S cluster in fumarate reductase (FRD), the homologue enzyme that catalyzes the reverse reaction. The FRD does not contain the *b*-heme. Shergill *et al.*[28] have studied the spin-lattice relaxation of the oxidized 3Fe-4S in FRD at 10K using the inversion recovery pulse sequence and have interpreted the data in terms of a single exponential.

Analysis of the Relaxation Recovery — In the air-oxidized state of SQR, only the S-3 center and the *b*-heme are paramagnetic. The *b*-heme is a low-spin ferric center with S = 1/2. In the case of the [3Fe-4S] cluster, antiferromagnetic exchange among the three ferric ions also lead to an S = 1/2 ground state with near isotropic g-values ($g \sim 2.0$).[15] Accordingly, we can treat this system as an isolated pair of electron spins separated by a fixed distance (r). The two spins, however, differ in their relaxation properties: the *b*-heme is rapidly relaxing, whereas the S-3 center is slowly relaxing. If the two spins are in close proximity, as appears to be the case here, then the rapidly relaxing *b*-heme can influence the relaxation of the slow-relaxing S-3 center. Specifically, the spin-lattice and transverse relaxation rates of the "slow"-relaxing spin can be affected by scalar exchange coupling and tensor magnetic dipolar interaction between the "fast" and "slow" relaxing spins. The spin-lattice relaxation of the "slow" relaxing spin will then include three

contributions: intrinsic relaxation, scalar exchange coupling, and the tensor magnetic dipolar interaction. The intrinsic and the scalar exchange relaxation rates are isotropic; and, together, they contribute a single exponential rate constant to the spin-lattice relaxation transients. However, the dipolar relaxation rate is orientation dependent.

Accordingly, the observed rates of spin-lattice relaxation can be described by

$$k_{1obs}(\theta) = k_{1scalar} + k_{1\theta}, \tag{1}$$

where $k_{1scalar} = k_{1i} + k_{1ex}$. k_{1i} is the intrinsic spin-lattice relaxation rate and k_{1ex} is the contribution to the relaxation rate due to superexchange. $k_{1\theta}$ denotes the dipolar relaxation rate previously derived by Kulikov and Likhtenstein[22] and by Goodman and Leigh[14] as well as cross-relaxation terms arising from superexchange and magnetic dipolar interaction (see Appendix I and II for details). For a given orientation θ of the interspin vector with respect to the applied magnetic field,

$$k_{1\theta} = (B + C + E). \tag{2}$$

The corresponding contribution to T_2 is

$$k_{2\theta} = \left(A + \frac{1}{2}B + \frac{C}{2} + 2D + \frac{E}{2} \right). \tag{3}$$

The terms *A*-*E* are given by

$$A = \frac{1}{3} T_{1f} [J^{A} \sqrt{S(S+1)} + \frac{\gamma_s \mu_f}{r^3} (1 - 3\cos^2 \theta)]^2, \tag{4}$$

$$B = \left(\frac{8}{3}\right)\frac{T_{2f}}{1+(\omega_s-\omega_f)^2T_{2f}^2}\left[\frac{J^B\sqrt{S(S+1)}}{2}+\frac{\gamma_s\mu_f}{4r^3}(1-3\cos^2\theta)\right]^2, \quad (5)$$

$$C = \frac{3T_{1f}}{1+\omega_s^2T_{1f}^2}\left[J^C\sqrt{S(S+1)}+\frac{\gamma_s\mu_f}{r^3}\sin\theta\cos\theta\right]^2, \quad (6)$$

$$D = \left(\frac{3}{2}\right)\frac{T_{2f}}{1+\omega_f^2T_{2f}^2}\left[J^D\sqrt{S(S+1)}+\frac{\gamma_s\mu_f}{r^3}\sin\theta\cos\theta\right]^2, \quad (7)$$

and $$E = \left(\frac{3}{2}\right)\frac{T_{2f}}{1+(\omega_s+\omega_f)^2T_{2f}^2}\left[\frac{J^E\sqrt{S(S+1)}}{2}+\frac{\gamma_s\mu_f}{r^3}\sin^2\theta\right]^2, \quad (8)$$

where γ_s is the magnetogyric ratio for the slow spin; μ_f is the magnetic dipole moment of the fast relaxing spin; r is the interspin distance; and J^A, J^B, J^C, J^D, and J^E denote the exchange contributions arising from the scalar and anisotropic electron exchange between the S-3 center and *b*-heme (Appendix II); T_{1f} and T_{2f} are the spin-lattice and transverse relaxation times of the fast relaxing spin; and ω_s and ω_f are the Larmor frequencies of the slow (observed) and fast spins, respectively. These expressions are valid when T_{1f} and $T_{2f} \ll T_{1s}$, the conditions observed here.

From these expressions, it is evident that $k_{1\theta}$ and $k_{2\theta}$ are dependent on the orientation of the interspin vector with respect to the applied magnetic field. For any one orientation of the interspin vector (θ, ϕ), the inversion recovery will decay exponentially with decay constant $k_1(\theta)$. Aside from r, T_{1f} and T_{2f} and J^B, $k_{1\theta}$ also depends on ω_s and ω_f. In our experiments, the slow spin (S-3 center) resonates over a wide range of frequency (100 G) while a 20 ns pulse has only a spectral width of ~18 G. Therefore, the

pulse is not able to excite the whole envelope of the S-3 center absorption. However, the signal of the S-3 center is approximately isotropic, so ω_s can be regarded as a constant for all orientations. On the other hand, the fast relaxing *b*-heme in SQR has a rhombic EPR signal, so that its Larmour frequency, ω_f, varies with the orientation of the protein molecule with respect to the applied magnetic field (see Appendix I for detail). For a given orientation (θ, ϕ) of the interspin vector relative to the applied magnetic field (Figure 7),

$$\mu_f = g_f(\theta, \phi)\beta[S(S+1)]^{1/2} = \frac{\sqrt{3}}{2}\beta g_f(\theta,\phi), \tag{9}$$

and $$\omega_f = g_f(\theta, \phi)\beta H_0. \tag{10}$$

$g_f(\theta, \phi)$ in turn depends on the orientation of the $\tilde{g}$ tensor of the *b*-heme *vis a vis* the magnetic field. Specifically,

$$g_f(\theta,\phi) = \left(g_z^{f\,2}\cos^2\eta + g_x^{f\,2}\sin^2\eta\cos^2\varepsilon + g_y^{f\,2}\sin^2\eta\sin^2\varepsilon\right)^{1/2} \tag{11}$$

where g_x^f, g_y^f, g_z^f refer to the principal components of the g-tensor for the *b*-heme, and (η, ε) denote the polar and azimuthal angles of the applied magnetic field *vis a vis* these principal axes. The detailed relationship between the effective $g_f^{b\text{-heme}}(\theta, \phi)$, or $g_{eff}^{b\text{-heme}}(\theta, \phi)$, and the orientations of the *b*-heme (θ', ϕ') *vis a vis* the interspin vector is given in Appendix I. Two sets of the angles, (θ, ϕ) and (θ', ϕ') between these three coordination

systems, the g-tensor of the *b*-heme, the interspin vector, and the magnetic field are shown in Figure 7.

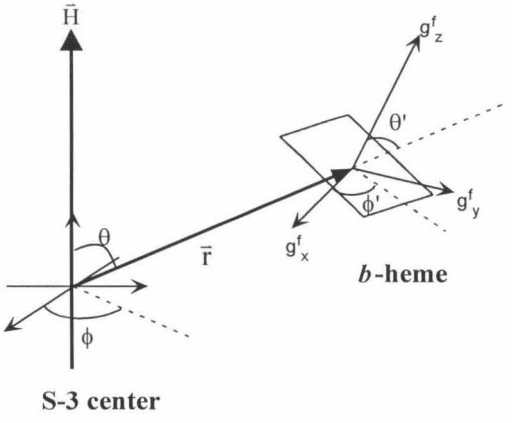

Figure 7. Relationship between the coordinate systems of the magnetic field, the interspin vector, and the g-tensor of *b*-heme. The orientation of the interspin vector with respect to the magnetic field: θ and ϕ. The orientation of g tensor principal axes of *b*-heme with respect to the interspin vector: θ' and ϕ'.

Due to the distribution of orientations (θ, ϕ) within the sample, the observed recovery traces will be the sum of exponentials. For a uniform distribution of interspin vectors, we can write

$$\frac{I(t)}{I(0)} = 1 - \frac{1}{4\pi}\int_0^{2\pi}\int_0^{\pi} e^{-(k_{1scalar}+k_{10})t}\sin\theta\, d\theta d\phi \quad , \qquad (12)$$

where I(t) is the intensity of the recovery transient at time t, I(0) is the initial intensity. Since the EPR signal of the S-3 center has no evident splitting caused by the exchange interaction with the *b*-heme, we suspect that the values of the J's are very small. We then will fit the data in the limit of J^A, J^B, J^C, J^D, and $J^E \rightarrow 0$ (for non-zero J^A, J^B values see below). Furthermore, to reach the limit $(\omega_s - \omega_f)^2 T_{2f}^2 >> 1$, it requires $T_{2f} >> 0.01$ ns at X-band. This is a reasonable range of T_{2f} ($0.001 < T_{2f} < 1$ μs) for a first row transition metal below liquid nitrogen temperature. Therefore, eq 12 simplifies to

$$\frac{I(t)}{I(0)} = 1 - e^{-k_{1scalar}t} \cdot \frac{1}{4\pi}\int_0^{2\pi}\int_0^{\pi}(e^{-k_{1d}\mu_f^2(\mathbf{b}+\mathbf{c}+\mathbf{e})t})\sin\theta d\theta d\phi, \qquad (13)$$

where we have defined $k_{1d} = \frac{\gamma_s^2}{r^6}$.

The terms **b**, **c**, **e** are

$$\mathbf{b} = \frac{(1-3\cos^2\theta)^2}{6(\omega_s - \omega_f(\theta,\phi))^2 T_{2f}}, \mathbf{c} = \frac{3\sin^2\theta\cos^2\theta}{\omega_s^2 T_{1f}}, \mathbf{e} = \frac{3\sin^4\theta}{2(\omega_s + \omega_f(\theta,\phi))^2 T_{2f}}. \qquad (14)$$

Of the three terms in eq 13, the last term, i.e., the **e** term, is usually unimportant. Hirsh and Brudvig[18] have shown that either the **b** or **c** term dominates $k_{1\theta}$ for isotropic spin systems.

Investigation on the relative contributions of b, c, and e terms in eq 13 —Eq 12 was integrated over θ and φ at specific orientations (θ', φ') of the *b*-heme with respect to the interspin vector (Figure 7). We used g_x^f, g_y^f, and g_z^f of 1.5, 2.1, and 3.6, respectively, for the *b*-heme. For SQR, there is a defined orientation of the interspin vector relative to the principal axes of the *b*-heme g-tensor. Unfortunately, in the absence of a structure for SQR, this orientation (θ', φ') is not known (Figure 7). Accordingly, we have examined various possibilities of this orientation, and the effects of this orientation on the relative contributions of the **b**, **c**, **e** terms in $k_{1\theta}$ (see Appendix III for detail). The **b**, **c**, and **e** term contributions are summarized in Figure A3-5. There, the **b**, **c**, **e** terms are plotted as a function of φ for various θ's for three combinations of θ'

and ϕ' (Figure A-3 for $\theta' = \phi' = 0°$; Figure A-4, for $\theta' = 30°$, $\phi' = 0°$; and Figure A-5, for $\theta' = 90°$, $\phi' = 0°$) and assuming $T_{1f} = T_{2f} = 0.1\mu s$ (see discussion and ref. 27). Although the **b** term will not dominate when $(1-3\cos^2\theta)^2/6 < 3\sin^2\theta\cos^2\theta$, a condition that is obtained for $\theta = 40°\sim 60°$ and $120°\sim 140°$, when eq 13 is integrated over θ and ϕ, the **b** term dominates.

We reach the same conclusions, if we ignore the variation of g_f/g_s in eq 14; i.e., if we assume that *b*-heme g tensor is isotropic and g_f is set equal to the average value of 2.2. In this limit, the three terms only depend on angle θ (see eq 14). Figure 8 shows the comparison of the magnitude of these three terms assuming $T_{1f} = T_{2f} = 0.1$ μs. Again, it is evident that the **b**-term dominates the other two terms, except when $(1-3\cos^2\theta) \approx 0$, or for θ near 54.74° or 125.26° , where all three terms are equally small. The same behavior was observed if $T_{1f} = T_{2f} = 0.01$ μs was used in calculation (data not shown).

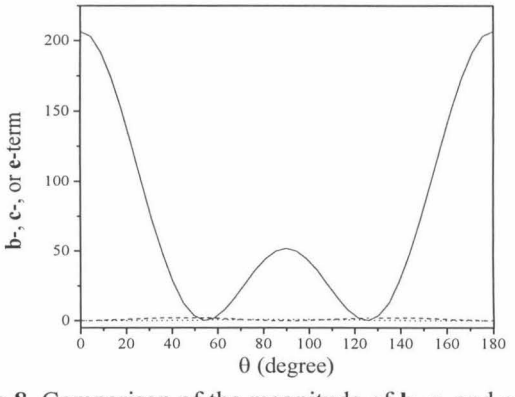

Figure 8. Comparison of the magnitude of **b**, **c**, and **e** terms of eq 14. **b** (solid line), **c** (dashed line), and **e** term (dotted line). Values are plotted versus θ. $T_{1f} = T_{2f} = 10^{-7}$ sec, and g_f (*b*-heme) fixed at 2.2.

From these results, it is evident that the **b**-term is the only dominant one for essentially any orientation of the *b*-heme tensor axes relative to the interspin vector. Apparently, $\omega_s - \omega_f << \omega_s$ or $\omega_s + \omega_f$ for any orientation of the *b*-heme. Moreover, T_{2f} is typically shorter than T_{1f}, and we have taken $T_{1f} = T_{2f}$ in these sample calculations in

order to deaccentuate the contribution of **b** and **c** terms as much as possible. Therefore, we may conclude with a high degree of assurance that the magnetic dipolar contribution to $k_{1\theta}$ comes principally from the **b** -term only, for any orientation of the *b*-heme relative to the interspin vector.

Simulations of the Magnetization Recovery — Simulations of the magnetization recovery were obtained at 4 K using the **b** term with $J^B = 0$ (eq 13) for various orientations of the *b*-heme (θ', ϕ') relative to the interspin vector. (θ' is the angle between the interspin vector and z axis of the g-tensor for the *b*-heme; ϕ' is the angle between the interspin vector and x axis.) The distance between the S-3 center and *b*-heme is included in k_{1d}. In the absence of a reliable T_{2f} measurement of the *b*-heme, we fit the data to yield $T_{2f}{\cdot}r^6$.

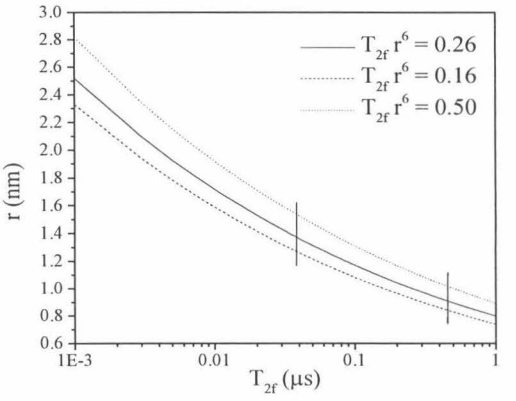

Figure 9. The relationship of r versus T_{2f} generated by the $T_{2f}{\cdot}r^6$ obtained from the simulations. $T_{2f}{\cdot}r^6 = 0.26$ $\mu s{\cdot}nm^6$ (solid line), $T_{2f}{\cdot}r^6 = 0.16$ $\mu s{\cdot}nm^6$ (dashed line), and $T_{2f}{\cdot}r^6 = 0.50$ $\mu s{\cdot}nm^6$ (dotted line). The vertical line at the right marks the T_{2f} obtained from the 2-pulse spin echo experiment and the vertical line at the left marks the lowest T_{2f} observed for low-spin hemes.

The simulation parameters that gave good fits are summarized in Table 2. From these results, we see that $k_{1scalar}$ ranges from 100 to 170 s^{-1} depending on the orientation (θ', ϕ') assumed and used to simulate the recovery. The $T_{2f}{\cdot}r^6$ distance obtained for the different heme orientations varies between 0.16 ~

0.50 μs·nm^6. A plot illustrating the relationship between T_{2f} and r for this range of $T_{2f}\cdot r^6$ as well as for $T_{2f}\cdot r^6 \sim 0.26$ is shown in Figure 9.

Table 2. Simulation parameters of the recovery trace of the S-3 center at 4 K (Figure 5(a)) for various heme orientations relative to the interspin vector.

(θ', ϕ')	$k_{1scalar}$ (s^{-1})	$T_{2f}\cdot r^6$ (μs·nm^6)	(θ', ϕ')	$k_{1scalar}$ (s^{-1})	$T_{2f}\cdot r^6$ (μs·nm^6)
0°, 0°	112.1	0.22	20°, 70°	106.1	0.24
0°, 30°	109.7	0.21	20°, 80°	104.7	0.23
0°, 60°	114.6	0.22	20°, 90°	103.3	0.21
0°, 90°	113.9	0.23	30°, 0°	148.6	0.36
10°, 10°	106.8	0.20	30°, 30°	123.0	0.30
10°, 20°	103.7	0.18	30°, 40°	131.5	0.29
10°, 30°	107.1	0.20	30°, 60°	130.5	0.32
10°, 40°	104.3	0.19	30°, 90°	89.32	0.23
10°, 50°	104.1	0.18	60°, 0°	129.5	0.25
10°, 60°	104.9	0.20	60°, 20°	121.2	0.26
10°, 70°	112.4	0.23	60°, 40°	152.9	0.34
10°, 80°	118.0	0.25	60°, 60°	152.6	0.31
10°, 90°	106.6	0.20	60°, 90°	124.1	0.22
20°, 0°	124.6	0.24	90°, 0°	129.5	0.40
20°, 10°	126.8	0.26	90°, 10°	151.2	0.37
20°, 20°	141.9	0.31	90°, 20°	171.2	0.50
20°, 30°	130.9	0.26	90°, 45°	136.0	0.16
20°, 40°	117.9	0.24	90°, 60°	169.1	0.35
20°, 50°	105.5	0.21	90°, 80°	146.7	0.29
20°, 60°	106.4	0.20	90°, 90°	130.5	0.19

2-pulse Transverse Relaxation Measurement of the b-heme — To have a good estimate of interspin distance between the S-3 center and *b*-heme, T_{2f} for the *b*-heme is needed. As noted in our previous study on SQR, the *b*-heme signal at g = 3.6 is very weak. The low intensity of the *b*-heme need not be associated with an unusually short T_1 or T_2. In derivative spectrum, the dispersion of the signal near g_z might be more important in determining the appearance of the signal than relaxation factors. We have

undertaken 2-pulse spin echo measurement of this signal at 4.2 K in an attempt to deduce the transverse relaxation time of the *b*-heme (T_{2f}). From the 2-pulse spin echo decay, T_m was the relaxation time constant obtained by fitting the data using a single-exponential decay (Figure 10). In addition to exponential decay, modulations are also shown in Figure 10, but we focus on the decay caused by transverse relaxation here. However, it should be noted that the T_m measured here can only be an upper limit to the real T_2, since it is possible that certain components of the heterogeneous signal are missed in the two-pulse experiments. Thus, we have $T_{2f} \leq T_m = 0.48$ μs, and we obtain a lower limit to r of 9 Å from the limiting range of $T_{2f} \cdot r^6$ ($8.33 < r < 10.07$ Å).

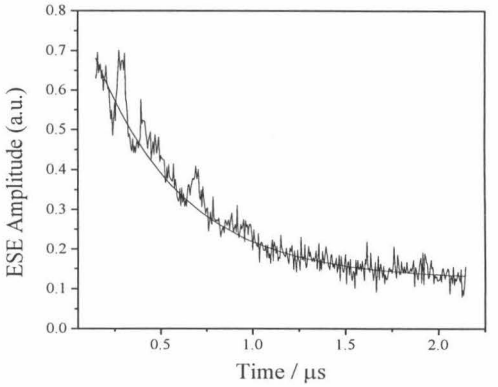

Figure 10. 2-pulse spin echo decay of the *b*-heme of SQR measured at g = 3.04 (microwave frequency: 10.22 GHz, magnetic field: 2402G) superimposed with single-exponential fit.

The Contribution of the Exchange Interaction Between the S-3 Center and the b-heme — It should be noted that the exchange interaction ($\mathbf{S} \cdot \mathbf{J} \cdot \mathbf{S}$) becomes important when the distance between spins is less than a few Å (~10 Å). The exchange interaction contributes to the same $S_{1\pm}S_{2\mp}$ matrix elements of the dipole-dipole interaction Hamiltonian that are the basis of the B term (Appendix II). The addition of non-zero values of J^B was tested to determine if the fit to the data could be improved. Again, these simulations (Table 3) were examined for different heme orientations (θ', ϕ'). The fits to

the data were not significantly improved with the addition of the exchange interaction. In any case, the exchange interaction required to improve the fits is small (≤ 6 MHz).

Table 3. Simulation parameters with the addition of exchange interaction. Other parameters are the same as the simulations mentioned in Table 2.

(θ', ϕ')	k_{1i} (s^{-1})	r (Å)	J^B (MHz)
0°, 0°	119.4	9.46	1.2
90°, 0°	127.6	10.6	3.54
0°, 90°	129.7	9.70	1.55
90°, 90°	147.1	10.8	6.01
45°, 0°	129.6	9.71	2.34
0°, 45°	128.2	9.66	2.13
60°, 60°	133.7	9.48	2.54
30°, 30°	119.7	9.78	2.98
0°, 30°	126.4	9.62	2.48
30°, 0°	143.8	10.0	3.10
60°, 0°	120.8	9.44	2.77
0°, 60°	128.1	9.64	1.83
45°, 45°	135.7	9.82	1.91

The Temperature Dependence of the Relaxation Time Constants — The recovery traces remain nonexponential over a temperature range of 4 – 8 K. At higher temperatures, we were not able to obtain data with sufficient signal to noise ratio because the S-3 center relaxes very fast. We simulated the data measured at the higher temperatures (data not shown) by fixing the value of $T_{2f} \cdot r^6$ to the average value estimated from the data obtained at 4.2 K; that is, $k_{1\theta}$ was assumed to be independent of temperature and $k_{1scalar}$ was treated as the only adjustable parameter in simulations ($k_{1\theta}$ is a function of T_{2f}, θ, ϕ, θ', ϕ', and r^6 when only **b** term is considered). This approximation assumes that T_{2f} is independent of temperature (case A), which is of course not correct.

Since $k_{1\theta}$ is proportional to $1/T_{2f}$ and $k_{1scalar}$ is related to the intrinsic $1/T_{1s}$, the temperature dependence of $k_{1scalar}$ should dominate the observed overall spin-lattice relaxation rate. Typically, T_2 exhibits a smaller temperature dependence compared to T_1. For example, in the low-spin ferric porphyrin, the temperature dependence of T_2 is much smaller than that of T_1.[27] For an upper limit on the temperature dependence of T_{2f} (case B), we scaled T_{2f} by the temperature dependence of $k_{1scalar}$. The calculated recovery curves for the S-3 center signal at four temperatures are shown in Figure 5. The values of simulation parameters used to simulate the curves for the two limits are given in Table 4. Figure 11 depicts the temperature dependence of the rate constant $k_{1scalar}$ for the S-3 center for the two limiting cases. As expected, $k_{1scalar}$ increases with increasing temperatures. As noted earlier, $k_{1scalar}$ consists of two parts; k_{1i} and k_{1ex}. Since the exchange contribution is small, i.e., J^B is small, $k_{1scalar}$ is dominated by k_{1i}.

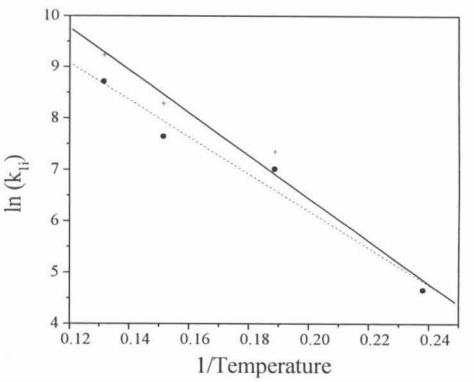

Figure 11. The temperature dependence of the spin-lattice relaxation rate for the S-3. The solid line is the fit of the data (case A: +) to exp(-41.6/T) for an Orbach process. The dashed line is the fit of the data (case B: •) to exp(-36.0/T).

Table 4. Simulation parameters for the recovery traces of the S-3 center measured at different temperatures (Figure 5).

Temperature (K)	$k_{1scalar}$ (s^{-1}) (case A)	$k_{1scalar}$ (s^{-1}) (case B)
4.2	105.52	105.52
5.3	1562.0	1111.2
6.6	3953.7	2094.5
7.6	10252	6064.8

Discussion

In a previous inversion recovery study of the S-3 center in fumarate reductase, the observed magnetization recovery was interpreted in terms of a simple exponential.[28] Only the 3Fe-4S center was paramagnetic in this previous study. In our present study on SQR, we have observed non-exponential behavior of the S-3 center, and have shown that the magnetization recovery following inversion remains non-exponential even after spectral diffusion effects are excluded by use of the picket-fence sequence. Since in SQR, the oxidized S-3 center coexists with the oxidized *b*-heme for the protein as isolated, we have attributed the anomalous spin-lattice relaxation of the S-3 center to magnetic tensor dipolar interaction and electron exchange interaction between the 3Fe-4S cluster and the *b*-heme. A theoretical model based on these interactions has been developed to account for the observed non-exponential decays, and recovery traces were simulated under varying conditions for comparison with experiment.

As expected, the contribution of the dipolar interaction to the relaxation of the S-3 center depends on the orientation of the *b*-heme relative to the vector between the interacting magnetic centers. In the absence of a structure for SQR, this orientation is, of course, not known. However, from the simulations of the 4 K data, we were able to obtain a range of possible value for $T_{2r}.r^6$, depending on the orientation of the *b*-heme.

Based on the two-pulse spin echo experiment of the *b*-heme, we have estimated a $T_{2f} = 0.48$ μs for the heme. From plots of r versus T_{2f} in Figure 9, the distance r could be determined to be in the range of 8.3 - 10.1 Å (right vertical line in the figure). Since the

two-pulse spin echo experiment provided merely an upper limit for T_{2f}, we conclude that this analysis offers a lower limit of 9 Å to the distance between the interacting centers.

On the other hand, a lower limit to T_{2f} could be inferred from the spin-lattice relaxation and transverse relaxation rates of known low-spin hemes. Eaton and co-workers[27] have examined the transverse relaxation rate for a number of low-spin iron porphyrins between 10 to 25 K. The T_2's of these centers are around 0.1 ~ 1.0 μs (0.21 ~ 0.63 μs) over this temperature range; thus, the rates are only weakly temperature dependent. Our 2-pulse spin echo measurement of the *b*-heme also yielded a T_{2f} that fell within this reasonable range. For other low-spin hemes, $T_2 \approx 0.13$ μs for cyt. *c* at 10 K,[2,9] and 0.036 μs for the cyt. *a* in cytochrome *c* oxidase at 15 K.[14] Note that these T_{2f}'s also fit the limit set before (eq 13), i.e., $T_{2f} >> 0.01$ ns. If we take 0.036 μs as the lower limit of T_{2f} for the *b*-heme in SQR, an upper limit of 12.7 ~ 15.4 Å can be obtained for r (left vertical line in Figure 9).

The above conclusions were based on an analysis that assumed only magnetic tensor dipolar interaction between the S-3 center and the *b*-heme. However, the exchange interaction ($\mathbf{S} \cdot \mathbf{J} \cdot \mathbf{S}$) becomes important when the distance between the interacting spins becomes sufficiently short, say, ≈ 10 Å. Since r ≥ 10 Å in the present problem, the exchange interaction to the relaxation is expected to be small. The addition of an exchange contribution (J^B) did not significantly improve the fits. Nevertheless, the possibility of a small contribution from the electron exchange interaction ($J^B \leq 6$MHz) cannot be excluded.

Although a constant value of J^B was used in these simulations to include the effect of electron exchange, strictly speaking the exchange contribution J^B to the *B* term is also angle-dependent. The presence of a low-spin heme species allows for anisotropic components in the exchange interaction due to the low-lying orbital states, in addition to those from the dipolar term. As shown in Appendix II, anisotropic exchange would contribute to an effective interaction that is dependent on the orientation of the interacting spin system *vis a vis* the applied magnetic field. However, since only the *B* term contributes to the non-exponential behavior in the T_1 decay of the S-3 center, there is no way to distinguish between isotropic versus anisotropic exchange contributions arising from the interaction of S-3 center with the *b*-heme. Moreover, when the exchange interaction is weak and is not even detected as a scalar interaction, its orientation dependence will escape detection as well.

We therefore conclude that the $k_{1\theta}$ is dominated by the magnetic dipole-dipole interaction. If so, the exchange interaction can contribute only in a minor way to the scalar relaxation rate. That is, $k_{1scalar}$ is dominated by k_{1i}.

Gayda *et al.*[13] and Bertrand *et al.*[7] have reported T_1 for the 3Fe-4S center in ferredoxin II *from Desulfovibrio gigas* and ferredoxin I from *Azotobacter vinelandii* at low temperatures (4 -10 K) using the power saturation method. These authors obtained $1/T_1$ values on the order of 1000 s^{-1} near 4 K, which is close to, but larger than, the $1/T_1$ deduced from our measured values of $k_{1scalar}$. From this correspondence, we surmise that the contribution from exchange interaction between the S-3 center and the *b*-heme to $k_{1scalar}$ could not be significant in SQR, in accord with our present conclusions.

In addition, the earlier results on the ferredoxins demonstrated that the relaxation behavior of the isolated 3Fe-4S cluster in these ferredoxins could be adequately described by the Orbach process, and their temperature dependences were used to deduce the energy of the lowest excited level in each of these clusters. An energy of about 20 cm^{-1} was obtained for both clusters. For the S-3 center in SQR, the temperature dependence of $k_{1scalar}$ ($\approx k_{1i}$) gave a simple exponential dependence [exp(-41.6/T) and exp(-36.0/T) for case A and case B, respectively], clearly suggesting an Orbach mechanism for the intrinsic relaxation of the 3Fe-4S cluster as well. From the data, we obtained energies of 29 ± 3.1 cm^{-1} and 25 ± 3.2 cm^{-1} for the two limiting cases.

For short interspin distances, one might expect splittings of the S-3 EPR signal by the exchange coupling. In the present instance, the magnitude of J^B is clearly small (< 6 MHz), and any splitting would be limited by the linewidth of the S-3 signal.

The role of the two redox centers, 4Fe-4S cluster (S-2 center) and *b*-heme, in the electron transfer pathway of SQR has been puzzling because of their low reduction potentials. In the recently solved x-ray crystal structure of fumarate reductase,[20] the iron-sulfur clusters are arranged in the sequence 2Fe-2S···4Fe-4S···3Fe-4S (S-1···S-2···S-3), and each of them are 13 ~ 14 Å apart. Involvement of the S-2 center in the electron transfer pathway was suggested on the basis of these results.[20] However, unlike SQR there is no heme in FRD. We speculate that the *b*-heme could mediate the electron transfer from the S-3 center to the quinone in SQR. The distance between the *b*-heme and the S-3 center deduced here is within the range of common cofactor separation distance observed in multi-centered electron transfer proteins. However, the detailed

mechanism of involvement of the *b*-heme in shuttling electrons or reducing equivalents to the quinone remains to be established.

Conclusions

The interspin distance between the S-3 center and *b*-heme in SQR has been estimated by simulating the recovery traces of the S-3 center measured by picket-fence pulse sequence. A lower limit of 10 Å was obtained. The temperature dependence of the intrinsic spin-lattice relaxation rate of the S-3 center suggests an Orbach mechanism for the process.

References

(1)Ackrell, B. A. C.; Johnson, M. K.; Gunsalus, R. P.; Cecchini, G. *Structure and function of succinate dehydrogenase and fumarate reductase*; Müller, F., Ed.; CRC Press: Boca Raton, 1992; Vol. III, pp 229-297.

(2)Allen, J. P.; Colvin, J. T.; Stinson, D. G.; Flynn, C. P.; Stapleton, H. J. *Biophys. J.* 1982, *38*, 299.

(3)Banci, L.; Bertini, I.; and Luchinat, C. *Nuclear and electron relaxation*; VCH: New York, 1991.

(4)Beck, W. F.; Innes, Jennifer B.; Lynch, John B.; and Brudvig, Gary W. *J. Magn. Reson.* 1991, *91*, 12.

(5)Berry, E. A.; Trumpower, B. L. *J. Biol. Chem.* 1985, *260*, 2458.

(6)Berry, E. A.; Trumpower, B. L. *Anal. Biochem.* 1987, *161*, 1.

(7)Bertrand, P.; Guigliarelli, B.; Meyer, J.; Gayda, J.-P. *Biochimie* 1984, *66*, 77.

(8)Bloembergen, N.; Shapiro, S.; Pershan, P. S.; Artman, J. O. *Phys. Rev.* 1959, *114*, 445.

(9)Brudvig, G. W.; Blair, D. F.; Chan, S. I. *J. Biol. Chem.* 1984, *259*, 11001.

(10)Cheng, C., Lin, T.-S., and Sloop, David J. *J. Mag. Res.* 1979, *33*, 71.

(11)Dalton, L. R., Harvard University, 1971.

(12)Galli, C.; Innes, J. B.; Hirsh, D. J.; Brudvig, G. W. *J. Magn. Reson.* 1996, *B110*, 284.

(13)Gayda, J.-P.; Bertrand, P.; Theodule, F.-X. *J. Chem. Phys.* 1982, *77*, 3387.

(14)Goodman, G.; Leigh, J. S. J. *Biochemistry* 1985, *24*, 2310.

(15)Guigliarelli, B.; More, C.; Bertrand, P.; Gayda, J.-P. *J. Chem. Phys.* 1986, *85*, 2774.

(16)Hägerhäll, C. *Biochim. Biophys. Acta* 1997, *1320*, 107.

(17)Hederstedt, L.; Ohnishi, T. *Progress in succinate:quinone oxidoreductase research*; Ernster, L., Ed.; Elsevier Science Publishers: Amsterdam, 1992, pp 163-198.

(18)Hirsh, D. J.; Brudvig, G. W. *J. Phys. Chem.* 1993, *97*, 13216.

(19)Houseman, A. L. P.; Doan, P. E.; Goodin, D. B.; Hoffman, B. M. *Biochemistry* 1993, *32*, 4430.

(20)Iverson, T. M.; Luna-Chavez, C.; Cecchini, G.; Rees, D. C. *Science* 1999, *284*, 1961.

(21)Koptyug, I. V.; Bossmann, Stefan H.; Turro, Nicholas J. *J. Am. Chem. Soc.* 1996, *118*, 1435.

(22)Kulikov, A. V.; Likhtenstein, G. I. *Adv. Mol. Relax. Interact. Processes* 1977, *10*, 47.

(23)Lorigan, G. A.; Britt, R. D. *Biochemistry* 1994, *33*, 12072.

(24)Matsson, M.; Ackrell, B. A. C.; Cochran, B.; Hederstedt, L. *Arch Microbiol* 1998, *170*, 27.

(25)Ohnishi, T. *Curr. Top. Bioenerg.* 1987, *15*, 37.

(26)Pennoyer, J. D.; Ohnishi, T.; Trumpower, B. L. *Biochim. Biophys. Acta* 1988, *935*, 195.

(27)Rakowsky, M. H.; More, K. M.; Kulikov, A. V.; Eaton, G. R.; Eaton, S. S. *J. Am. Chem. Soc.* 1995, *117*, 2049.

(28)Shergill, J. K.; Cammack, R.; Weiner, J. H. *J. Chem. Soc. Faraday Trans.* 1991, *87*, 3199.

(29)Steffens, G. C. M.; Pascual, E.; Buse, G. *J. Chromatogr.* 1990, *521*, 291.

(30)Stowell, M. H. B.; Larsen, R. W.; Winkler, J. R.; Rees, D. C.; Chan, S. I. *J. Phys. Chem.* 1993, *97*, 3054.

(31)Sturgeon, B. E.; Britt, R. D. *Rev. Sci. Instrum.* 1992, *63*, 2187.

(32)Waldeck, A. R.; Stowell, M. H. B.; Lee, H. K.; Hung, S.-C.; Matsson, M.; Hederstedt, L.; Ackrell, B. A. C.; Chan, S. I. *J. Biol. Chem.* 1997, *272*, 19373.

(33)Wilson, D. F.; King, T. E. *J. Biol. Chem.* 1964, *239*, 2683.

Appendix I

We defined the interspin vector as **X**(x, y, z) coordinate. The angles between the interspin vector and the magnetic field are θ and ϕ. The unit vector along the magnetic field can be expressed in this coordinate as

$$\hat{n} = \sin\theta\cos\phi\ \hat{x} + \sin\theta\sin\phi\ \hat{y} + \cos\theta\ \hat{z} \tag{A1}$$

The **X**'(x', y', z') coordinate of *b*-heme g-tensor can be defined by the two angles between the **X** and **X**' coordinate, θ' and ϕ'.

$$\mathbf{X}' = \mathbf{A}\mathbf{X} = \begin{pmatrix} \cos\theta'\cos\phi' & \cos\theta'\sin\phi' & -\sin\theta' \\ -\sin\phi' & \cos\phi' & 0 \\ \sin\theta'\cos\phi' & \sin\theta'\sin\phi' & \cos\theta' \end{pmatrix} \mathbf{X} \tag{A2}$$

$$\hat{n}_{X'} = \mathbf{A}\cdot\hat{n}_X = \begin{pmatrix} \cos\theta'\cos\phi' & \cos\theta'\sin\phi' & -\sin\theta' \\ -\sin\phi' & \cos\phi' & 0 \\ \sin\theta'\cos\phi' & \sin\theta'\sin\phi' & \cos\theta' \end{pmatrix} \cdot \begin{pmatrix} \sin\theta\cos\phi \\ \sin\theta\sin\phi \\ \cos\theta \end{pmatrix} \tag{A3}$$

$$\begin{aligned} g_{\text{eff}}^{\text{b-heme}} &= [\hat{n}_{X'}^{T}(g\cdot g^{T})\hat{n}_{X'}]^{1/2} \\ &= \left(g_z^{f\,2}\cos^2\eta + g_x^{f\,2}\sin^2\eta\cos^2\varepsilon + g_y^{f\,2}\sin^2\eta\sin^2\varepsilon\right)^{1/2} \end{aligned} \tag{A4}$$

Appendix II

In order to introduce the exchange coupling into the dipolar model, we begin with Bloembergen and co-worker's treatment of cross relaxation.[8] Consider the general spin Hamiltonian

$$\hat{H} = \hat{H}_{z} + \hat{H}_{cf} + \hat{H}_{sp-sp}, \tag{A5}$$

where the three terms on the right-hand side are the Zeeman term $\hat{H}_{z}$, the crystal field plus quadrupolar term $\hat{H}_{cf}$, and the generalized spin-spin interaction $\hat{H}_{sp-sp}$, respectively. For the generalized spin-spin interaction between the two spins, $\hat{H}_{12}$ contains dipolar ($g_1 g_2 \beta^2 / r_{12}^3$) and pseudodipolar ($B_{12}$) terms, and it has the explicit form

$$\hat{H}_{sp-sp} = \boldsymbol{A} + \boldsymbol{B} + \boldsymbol{C} + \boldsymbol{D} + \boldsymbol{E} + \boldsymbol{F} \tag{A6}$$

with $$\boldsymbol{A} = [(\frac{g_1 g_2 \beta^2}{r_{12}^3} + B_{12})(1 - 3\cos^2\theta_{12})] S_{1Z} S_{2Z}$$

$$\boldsymbol{B} = \frac{1}{4}[(\frac{g_1 g_2 \beta^2}{r_{12}^3} + B_{12})(1 - 3\cos^2\theta_{12})](S_{1+} S_{2-} + S_{1-} S_{2+})$$

$$\boldsymbol{C} = \frac{-3}{2}(\frac{g_1 g_2 \beta^2}{r_{12}^3} + B_{12}) \sin\theta_{12} \cos\theta_{12} \exp(-i\phi_{12})(S_{1+} S_{2Z} + S_{1Z} S_{2+})$$

$$\boldsymbol{D} = \frac{-3}{2}(\frac{g_1 g_2 \beta^2}{r_{12}^3} + B_{12}) \sin\theta_{12} \cos\theta_{12} \exp(i\phi_{12})(S_{1-} S_{2Z} + S_{1Z} S_{2-})$$

$$\boldsymbol{E} = \frac{-3}{4}(\frac{g_1 g_2 \beta^2}{r_{12}^3} + B_{12}) \sin^2\theta_{12} \exp(-2i\phi_{12}) S_{1+} S_{2+}$$

$$\boldsymbol{F} = \frac{-3}{4}(\frac{g_1 g_2 \beta^2}{r_{12}^3} + B_{12}) \sin^2\theta_{12} \exp(2i\phi_{12}) S_{1-} S_{2-}.$$

With $B_{ij} = 0$, the spin-spin interaction reduces to dipolar interaction. When the interspin distance becomes sufficiently short, we need to add the exchange contribution $\hat{H}_{ex}$ to the Hamiltonian:

$$\hat{H}_{ex} = \boldsymbol{S}_1 \cdot \mathbf{J} \cdot \boldsymbol{S}_2 = (S_{1x} \quad S_{1y} \quad S_{1z}) \begin{pmatrix} J_{xx} & J_{xy} & J_{xz} \\ J_{yx} & J_{yy} & J_{yz} \\ J_{zx} & J_{zy} & J_{zz} \end{pmatrix} \begin{pmatrix} S_{2x} \\ S_{2y} \\ S_{2z} \end{pmatrix} \tag{A7}$$

where x, y, z denote a set of axes fixed onto the molecular frame. To convert $\hat{H}_{ex}$ to the laboratory frame, the J-tensor can be transformed to $\mathbf{J'} = \mathbf{n}^{\mathrm{T}} \cdot \mathbf{J} \cdot \mathbf{n}$, where $\mathbf{n}$ is similar to the rotation matrix $\mathbf{A}$ introduced in Appendix I (eq A2). Thus, eq A7 can be re-written as

$$\begin{aligned} \hat{H}_{ex} &= \boldsymbol{S}_1 \cdot \mathbf{J'} \cdot \boldsymbol{S}_2 = (S_{1X} \quad S_{1Y} \quad S_{1Z}) \mathbf{J'} \begin{pmatrix} S_{2X} \\ S_{2Y} \\ S_{2Z} \end{pmatrix} \\ &= (S_{1X} \quad S_{1Y} \quad S_{1Z}) \begin{pmatrix} J'_{XX} & J'_{XY} & J'_{XZ} \\ J'_{YX} & J'_{YY} & J'_{YZ} \\ J'_{ZX} & J'_{ZY} & J'_{ZZ} \end{pmatrix} \begin{pmatrix} S_{2X} \\ S_{2Y} \\ S_{2Z} \end{pmatrix} \end{aligned} \tag{A8}$$

As usual, $\mathbf{J'}$ can be separated into a scalar part, a polar vector, and a symmetric traceless tensor. When eq A8 is expanded, different terms in J′-tensor contribute to the various terms of the dipolar Hamiltonian ($\boldsymbol{A} - \boldsymbol{F}$ terms in eq A6). Specifically, only J'_{XX} and J'_{YY} of exchange coupling contributes to $\boldsymbol{B}$ term (J^{B}). Note that all terms in J′-tensor are angle-dependent and vary with the orientation of the *b*-heme with respect to the interspin vector.

Appendix III

The contributions of **b**, **c**, **e** terms in eq 13: Eq 13 were integrated over θ and ϕ at a specific orientation (θ', ϕ') of the *b*-heme with respect to the interspin vector (Figure 7). g_f in turn can be expressed as a function of these four angles, θ, ϕ, θ', and ϕ' (Appendix I), where the g_x, g_y, and g_z of the *b*-heme are 1.5, 2.1, and 3.6, respectively.

g_f is a function of θ and ϕ at a specific orientation of θ', ϕ'; therefore, the three terms, **b**, **c**, and **e** terms, which are functions of g_f, are also dependent on these four angles. In Figure A-1, g_f is plotted versus ϕ at various θ's. g_f ranges from 1.5 (g_x) to 3.6

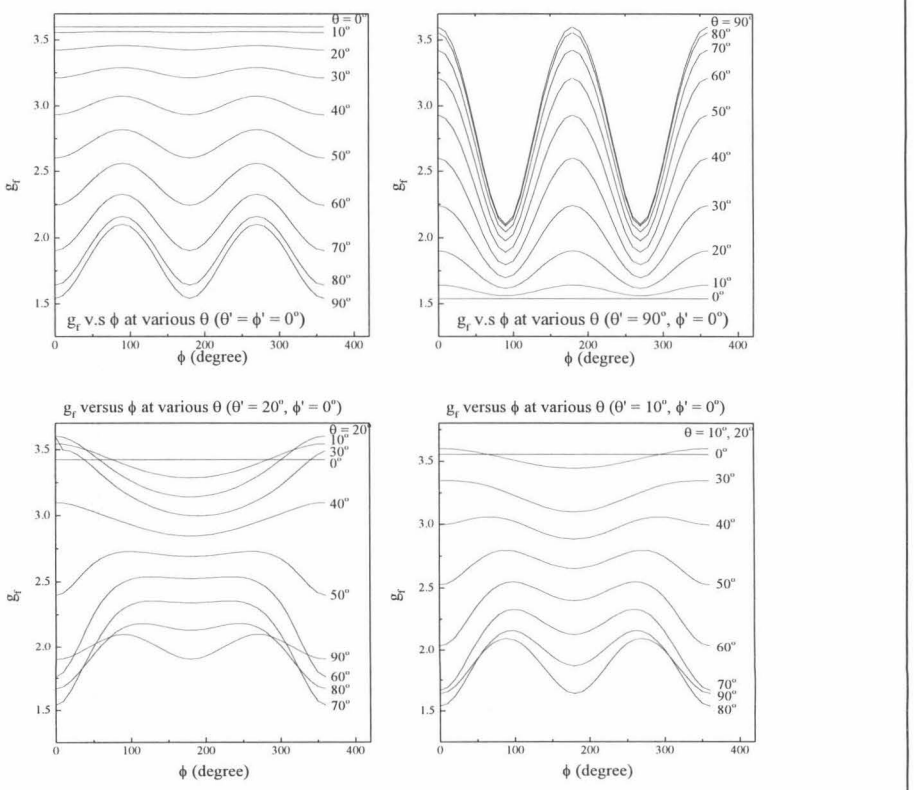

Figure A-1. The dependence of g_f (*b*-heme) on θ and ϕ at several (θ', ϕ') orientations.

(g_z) for different (θ', ϕ') orientations. (The averaged g_f is also plotted versus ϕ' at various θ''s in Figure A-2.) Similarly, for each combination of θ' and ϕ', **b**, **c**, and **e** terms can be

plotted as a function of ϕ for various θ's (Figure A-3 for $\theta' = \phi' = 0°$; Figure A-4, for $\theta' = 30°$, $\phi' = 0°$; and Figure A-5, for $\theta' = 90°$, $\phi' = 0°$) and assuming $T_{1f} = T_{2f} = 0.1$ μs. The dominance of the **b** term will not be valid when $(1 - 3\cos^2\theta)/6 < 3\sin^2\theta\cos^2\theta$, which normally occurs at $\theta = 40°$ ~ 60° and 120° ~ 140°. However, for the majority of the θ and ϕ region, the **b** term dominates. Therefore, for each integration over θ and ϕ in eq 13, **b** term dominates.

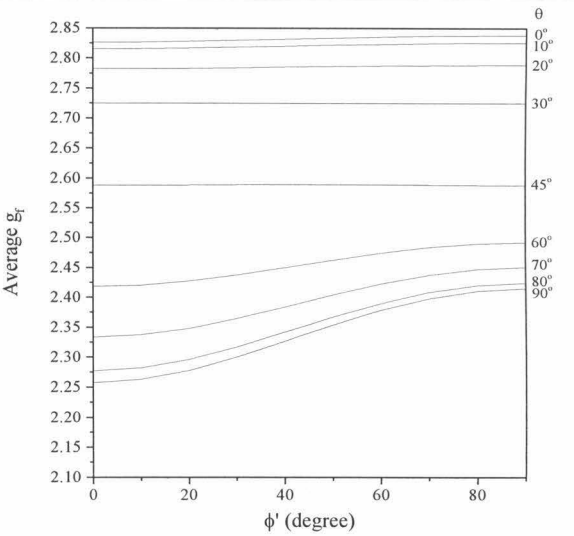

Figure A-2. Averaged g_f (*b*-heme) as a function of the *b*-heme orientation with respect to the interspin vector (θ',

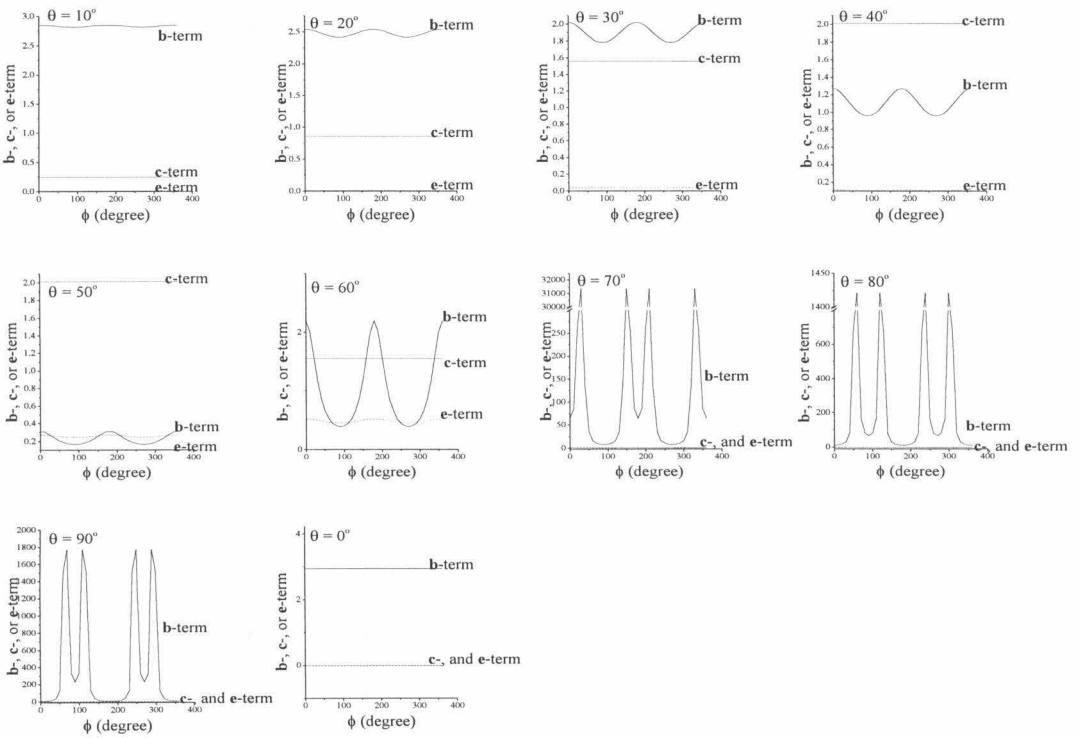

Figure A-3. Comparison of the magnitude of **b**, **c**, and **e** terms of eq 14. **b** (solid line), **c** (*dashed line*), and **e** term (dotted line). Values are plotted versus ϕ at various θ's. $T_{1f} = T_{2f} = 10^{-7}$s, and $\theta' = \phi' = 0°$.

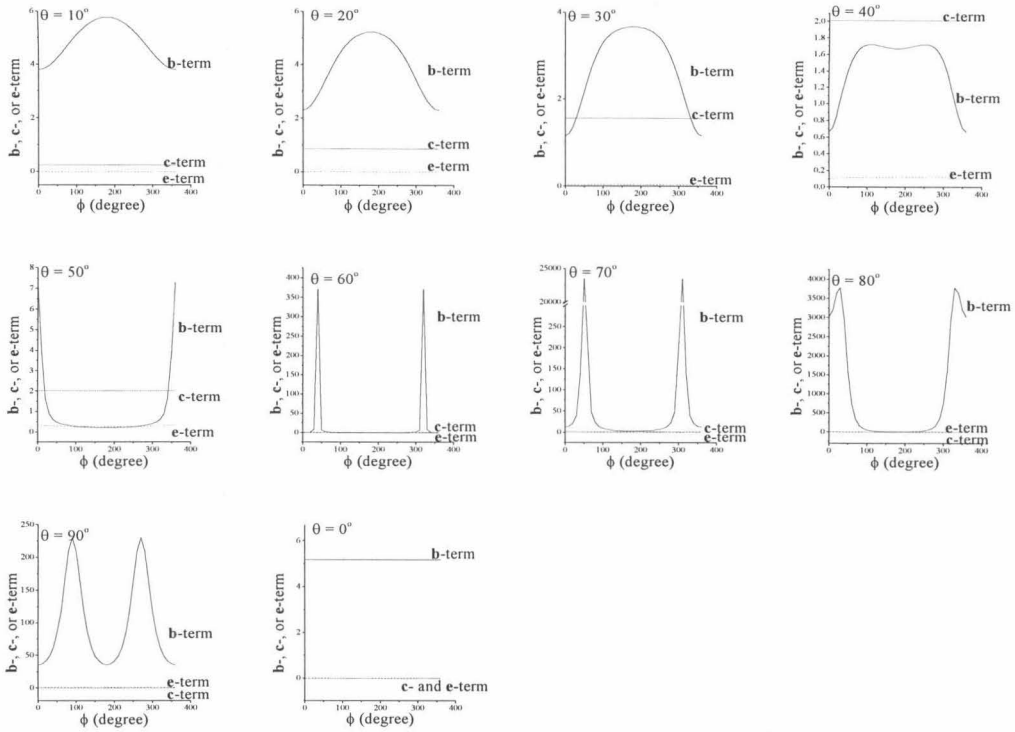

Figure A-4. Comparison of the magnitude of **b**, **c**, and **e** terms of eq 14. **b** (solid line), **c** (dashed line), and **e** term (dotted line). Values are plotted versus ϕ at various θ's. $T_{1f} = T_{2f} = 10^{-7}$ s, and θ' = 30°, ϕ' = 0°.

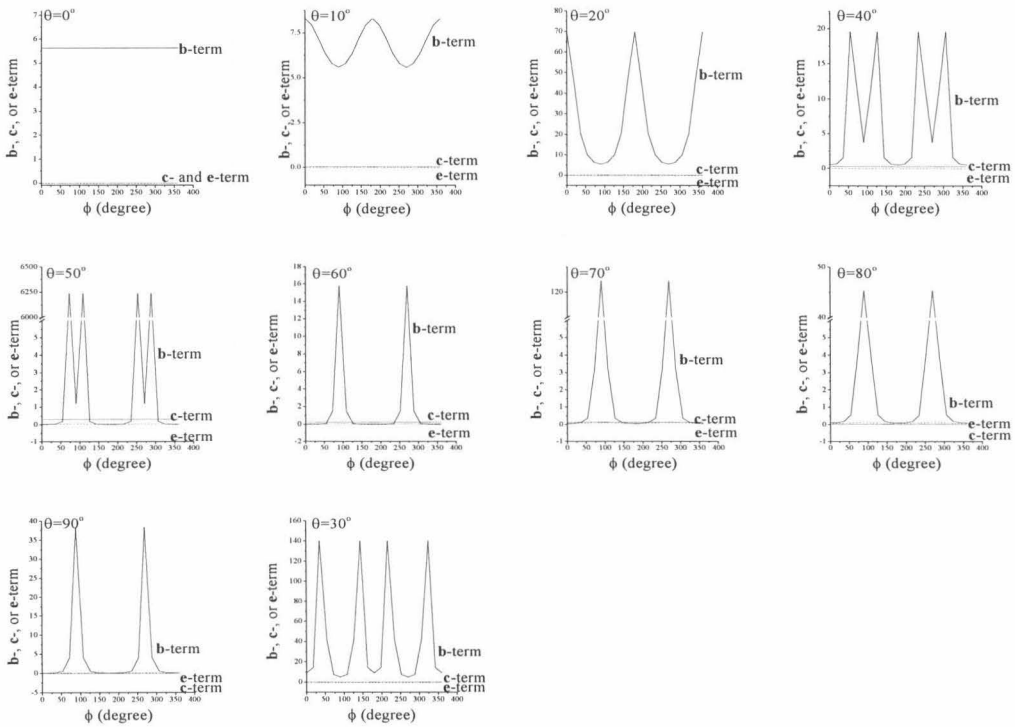

Figure A-5. Comparison of the magnitude of **b**, **c**, and **e** terms of eq 14. **b** (solid line), **c** (dashed line), and **e** term (dotted line). Values are plotted versus ϕ at various θ's. $T_{1f} = T_{2f} = 10^{-7}$ s, and θ' = 90°, ϕ' = 0°.

Chapter 4:

ESEEM Studies of Succinate:Ubiquinone Reductase from *Paracoccus denitrificans*

Abstract

Electron spin-echo envelope modulation (ESEEM) spectroscopy has been performed in order to obtain structural information about the environment of the reduced [2Fe-2S] cluster (S-1 center), the oxidized [3Fe-4S] cluster (S-3 center), and the flavin semiquinone radical in purified succinate:ubiquinone reductase from *Paracoccus denitrificans*. Spectral simulations of the ESEEM data from the reduced [2Fe-2S] yielded nuclear quadrupole interaction parameters that are indicative of peptide nitrogens. We also observed a weak interaction between the oxidized [3Fe-4S] cluster and a peptide ^{14}N. There was no evidence for coordination of any of the Fe atoms to ^{14}N-atoms of imidazole rings. The ESEEM data from the flavin semiquinone radical were more complicated. Here, evidence was obtained for interactions between the unpaired electron and only the two nitrogen atoms in the flavin ring.

Introduction

Electron spin-echo (ESE) techniques have been demonstrated to be useful for gaining qualitative and quantitative information about the ligand structure of a paramagnetic center in biological systems. In recent years, structural data have been obtained by analyzing electron spin-echo envelope modulation (ESEEM) arising from hyperfine interaction with various types of nuclei.[1]

ESEEM spectroscopy greatly improves our ability to measure small electron-nuclear hyperfine couplings, which are typically not resolved by the continuous-wave (CW) EPR. Hyperfine and nuclear quadrupole frequencies can be obtained conveniently by Fourier transformation of two- or three-pulse ESEEM data. It is the method of choice for detecting weakly coupled nuclei, such as magnetic nuclei of ligand atoms in the second coordination sphere of a metal center. This method is therefore supremely suited for the observation of the remote ^{14}N nuclei of histidines coordinated to a paramagnetic center. For example, all [2Fe-2S] clusters examined to-date have shown an interaction with a nitrogen atom, coordinated either directly[2-4] or indirectly.[5,6]

In this paper, we describe the application of ESEEM spectroscopy to Succinate:Ubiquinone Reductase (SQR) from *Paracoccus denitrificans* (*P. d.*). This enzyme catalyses the oxidation of succinate to fumarate in the plasma membrane. It is a membrane protein consisting of two hydrophilic subunits: the flavoprotein subunit (Mw 65,600); the iron-sulfur subunit (Mw 29,600); and two smaller hydrophobic subunits (Mw 14,300 and 13,900) that act as membrane anchors, bind one molecule of *b*-heme, and consist of two quinone binding sites, Q_A and Q_B (for reviews see ref. 7-10). Together, the two hydrophilic subunits constitute what is often referred to as succinate

dehydrogenase (SDH). The larger hydrophilic subunit contains a covalently bound flavin adenine dinucleotide (FAD) and is designated FP. The smaller subunit is designated IP; it contains the three iron-sulfur clusters, the S-1, S-2, and S-3 centers. The S-1 center is a [2Fe-2S] cluster with a spin S=1/2 in its reduced state. The S-3 center is a trinuclear [3Fe-4S] type cluster, and is an S=1/2 paramagnetic center when oxidized. The S-2 center is a [4Fe-4S] cluster; it is S=1/2 when reduced. Unfortunately, its EPR spectrum is highly anisotropic, and is therefore weak. The ESEEM spectra of the oxidized S-3 center, the reduced S-1 center, and the flavin semiquinone radical are reported in the present work.

Pulsed EPR methods have previously been applied to the study of more complex proteins, such as succinate dehydrogenase (SDH) in submitochondrial particles from *Arum maculatum* (*A. m.*) spadix,[11] the fumarate reductase (FRD) complex,[5,12] and the bovine SQR.[13] The goals of the present study are to compare the ligand environments of the metallic cofactors in FRD, SDH,and mammalian and bacterial SQR. This work is timely given the recently reported crystal structure of FRD from *E. coli*[14] and from *Wolinella succinogenes*.[15]

Experimental Setup

EPR Sample Preparation — The *P. d.* SQR used for these studies was purified as described previously.[16] Three samples were prepared each with 50 μM of protein. Initially, 165 μL aliquots of the oxidized (as isolated) protein suspension were placed in conventional quartz EPR tubes. In one of the samples, the protein was then treated with excess sodium succinate and incubated at room temperature for 45 min to obtain partial

reduction. In a second, excess sodium dithionite was also added to the protein to obtain complete reduction in a separate experiment. These samples were stored in liquid nitrogen until needed for ESEEM experiments.

Pulsed EPR Measurements — The pulsed EPR experiments at X-band were conducted on a home-built instrument.[17] Experiments were performed at 4.2 K with the resonator probe mounted in the sample space of a Janis "Super Varitemp" liquid helium dewar assembly and immersing the probe structure (and sample) in the liquid helium.

ESEEM data were collected either by the two-pulse (90° - τ - 180°) or by the stimulated echo (90°- τ - 90° - T - 90°) procedure, with values of τ in the latter method set to multiples of the proton Zeeman frequency in order to suppress modulations due to weakly coupled protons.

ESEEM Background — The spectrum of a frozen solution is a superposition of the spectra arising from all molecular orientations relative to the applied magnetic field. As will be shown later, the ESE modulations observed in this work arise from the interactions of the paramagnetic centers in SQR with ^{14}N's of the peptide. In general, the Hamiltonian used to determine the superhyperfine frequencies includes three terms: the ^{14}N nuclear Zeeman interaction ($g_n\beta_n \vec{B}_0 \cdot \vec{I}$), the electron nuclear superhyperfine interaction ($\vec{I} \cdot \overline{\overline{A}} \cdot \vec{S}$), and the nuclear quadrupole interaction ($\vec{I} \cdot \overline{\overline{P}} \cdot \vec{I}$). The nuclear quadrupole interaction (NQI) is characterized by five quantities: the electron quadrupole coupling parameter (e^2qQ), the asymmetry parameter (η), and three Euler angles (α, β, and γ) which are used to relate the principal axis system (PAS) of the NQI tensor with respect to the g-tensor. The most well defined and most intense ESEEM spectra arise at

the condition of "exact cancellation,"[18] when $\nu_i = |A_{iso}/2|$; that is, when ν_i, the nuclear Larmor frequency at the observing magnetic field is equal to half of A_{iso}, the isotropic nuclear hyperfine coupling constant. In this case, the salient spectral features for ^{14}N are three pure quadrupolar peaks (ν_0, ν_-, ν_+) in the manifold where the Zeeman and hyperfine interactions cancel.

$$\nu_0 = 1/2\ \eta\ e^2qQ\ h^{-1}, \tag{1}$$

$$\nu_\pm = 3/4\ e^2qQ\ (1 \pm \eta/3)\ h^{-1}. \tag{2}$$

The two lower components add to give the frequency of the third. A broader double-quantum peak (ν_{dq}) also arises from the other manifold (4-6 MHz).[18]

$$\nu_{dq} = 2\ (|\nu_i + |A_{iso}|/2|^2 + \xi^2\ )^{1/2}, \tag{3}$$

where $\xi = 1/4\ e^2qQ\ (3 + \eta^2)^{1/2}$. The asymmetry parameter (η) and the quadrupole coupling constant (e^2qQ) can be determined directly from the frequencies of the pure nuclear quadrupolar peaks, while the isotropic hyperfine coupling (A_{iso}) can be calculated from the double quantum line. Model calculations of ESEEM spectra from nucleus with I = 1 have shown that this analysis is applicable if $|\nu_i - A_{iso}/2| \leq 0.25\ \nu_i$, in which case the quadrupole frequencies can be obtained to within 10% accuracy.[19] When $0.25\ \nu_i < |\nu_i - A_{iso}/2| < 2/3\ (e^2qQ/4)$, the superhyperfine couplings are dominated by ^{14}N nuclear quadrupole interaction. In this case, the observed ^{14}N ESEEM are weaker but similar in appearance to those observed for exact cancellation conditions. Finally, for cases where $|\nu_i - A_{iso}/2| > 2/3\ (e^2qQ/4)$, the peaks corresponding to ν_0 and ν_- broaden

out, and typical ^{14}N ESEEM spectra show only two broad peaks corresponding to the "$\Delta m_I = 2$" transitions from each electron spin manifold.

Except for the semiquinone radical ESEEM, four lines are observed in all the ESEEM spectra obtained in this work on SQR. Thus, the limit of either (a) "exact cancellation," or (b) where $0.25\ \nu_i < |\nu_i - A_{iso}/2| < 2/3\ (e^2qQ/4)$ is applicable, and the above results can be used to analyze the spectra. Accordingly, the e^2qQ, η, and A_{iso} calculated using eqs 1-3 were used as starting values for the spectral simulations of the S-1 and S-3 centers. All of the coupling constants were subsequently refined to deduce the orientation of the PAS of the quadrupole coupling tensor and that of the A-tensor relative to the g-tensor. The semiquinone radical ESEEM at g = 2.005 was more complicated. Here, the spectra were analyzed on the basis of previous studies of flavin semiquinone radicals from other proteins.[20-22]

Analysis and Spectral Simulations — A program based on the density matrix formalism of Mims[23] was used for the analysis of the ESEEM data to obtain ^{14}N superhyperfine coupling parameters. The ESEEM simulation calculations begin by determining the molecular orientations that contribute to the EPR spectrum at a given field. This is carried out by employing the same approach originally used by Hurst, Henderson and Kreilick[24] to analyze "angle-selected ENDOR." The orientations determined from this calculation are then used to calculate the modulation function for disordered systems.[19,23,25]

As mentioned earlier, the spin Hamiltonian contains electronic and nuclear Zeeman, electron-nuclear hyperfine, and nuclear quadrupole interactions. The g-tensor of the paramagnetic species, which has been characterized in our earlier study,[16] and g_N

of ^{14}N are not adjustable in the simulations. The electron-nuclear hyperfine coupling tensor, $\overline{\overline{A}}$, is assumed to be axial, and is formulated within the point dipole-dipole approximation. An isotropic term A_{iso}, a dipole-dipole distance r_{eff}, and two angles θ_N and ϕ_N, that describe the relationship between the principal axes system (PAS) of the g-tensor and that of the hyperfine tensor, are required to describe this interaction. The nuclear quadrupole interaction is characterized by five terms: e^2qQ, η, and three Euler angles that transform the PAS of the nuclear quadrupole interaction tensor into that of the g-tensor. The computer program NANG was used to simulate the time domain modulation spectra and program FTBILL was used to perform the Fourier transform.

For the experimental and simulated ESEEM spectra in this work, the values of A_{iso}, e^2qQ and η were determined by the ESEEM frequencies. The values of the other hyperfine parameters, θ_N, ϕ_N, and r_{eff}, were adjusted to obtain the proper shifts in the superhyperfine frequencies. The Euler angles describing the PAS of the nuclear quadrupole interaction relative to that of the g-tensor were set so that the relative amplitudes of the frequency components varied properly across the spectrum. To facilitate the comparison between the simulated and experimental patterns of the time-domain modulations, the experimental data were divided by a decay function,

$$V_{decay}(T) = N \exp(-T/T_m'), \qquad (4)$$

where N is a normalizing factor and T_m' is the decay time constant.

Results and Discussion

Assignment of the ESEEM Spectral Lines

ESEEM experiments were performed on "air-oxidized," succinate-reduced, and dithionite-reduced SQR. Only the S-3 center and the *b*-heme are paramagnetic when the sample is "air-oxidized." When the sample is reduced by succinate, the S-3 center becomes reduced to a spin S = 2 state and is not observable in our ESEEM experiments. The S-1 center is also reduced, and it becomes paramagnetic. New EPR signals also arise from the FAD•, Q_A•, and Q_B•. Upon reduction of the sample by dithionite, FAD, Q_A, and Q_B become reduced further to a diamagnetic state, and ESEEM is observable only from the S-1 center. The S-2 center is also reduced by dithionite to yield a paramagnetic species, but its signal is too weak to contribute to the ESEEM.

"Air-oxidized" SQR — The three-pulse ESEEM of the S-3 center was observed at g = 2.01 on the oxidized protein at 4.2 K with a microwave frequency of 9.491 GHz. Figure 1(a) and 1(b) show the time domain spectra and the associated Fourier transform spectra, respectively. It shows a very weak modulation at low frequencies. For comparison, the normalized echo amplitude of the 3-pulse ESEEM of the S-3 center is plotted with the data of the S-1 center in Figure 1(c). It shows clearly that the modulation depth of the S-3 spectrum is less than 10% of its echo amplitude. On the other hand, the modulation depth of the signal arising from the S-1 center is more than twice larger than that from the signal of the S-3 center.

In order to observe all the possible ESEEM peaks, the ESEEM spectra were collected at two different values of τ, 209 ns (solid line in figures 1(a), 1(b)) and 279 ns (dashed line). Peaks are resolved in the frequency domain spectrum at 0.8, 2.1, 3.3, and

4.1 MHz. These features are characteristic of weakly coupled ^{14}N nuclei. A similar weak interaction between the S-3 center of bovine heart SQR and a ^{14}N nucleus in the protein backbone have previously been reported by Ackrell *et al.*[13] Slight changes in the positions and the intensity of the low-frequency components were observed upon changing the τ-value at which the ESEEM was recorded. The coupling parameters calculated from eqs 1-3 are $A_{iso} \approx 0.48$ MHz, $e^2qQ \approx 3.5$ MHz, and $\eta \approx 0.44$. Here, A_{iso} of the S-3 center is not large enough to meet the requirement of "exact cancellation" at X-band frequencies. Later, we shall verify these "estimated" parameters by spectral simulations.

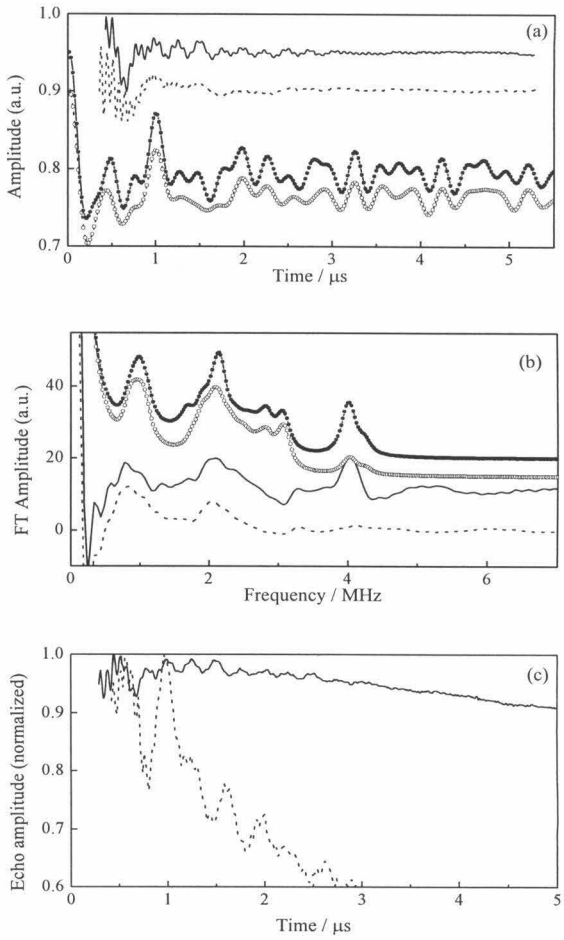

Figure 1. Three-pulse ESEEM spectra of the oxidized [3Fe-4S] (S-3) cluster of *P. d.* SQR. (a) Time-domain data of τ = 209ns (solid line) and τ = 279 ns (dashed line) plotted with the corresponding simulations of τ = 209 ns (solid circle) and τ = 279 ns (open circle). (b) Fourier transform of the ESEEM data. (c) Normalized time-domain data of the S-3 center (solid line). For comparison, the normalized data of the S-1 center (dashed line) obtained at g = 1.935 is also shown. Experimental conditions for the oxidized S-3 center: microwave frequency 9.49 GHz at 3373 G magnetic field strength (g = 2.01); pulse width, 25 ns; temperature, 4.2 K. Simulation parameters: $A_{iso} = 0.9$ MHz, $r_{eff} = 3.7$ Å, θ, φ = 45°, 20°, $e^2qQ = 3.2$ MHz, $\eta = 0.5$, and α, β, γ = 20°, 82°, 85°, for both τ = 209 ns and τ = 279 ns. See legend for Figure 2 for the corresponding experimental details in the case of the S-1 center.

Succinate-reduced SQR — Upon succinate reduction, SQR showed low frequency ESEEM at g = 1.935 and 2.005 that was distinct from that found for oxidized protein. The ESEEM at g = 1.935 corresponds to the signal from the $g_{\perp}$ of the reduced S-1 center, while the ESEEM at g = 2.005 arise from the FAD•, Q_A•, and Q_B•.

The time-domain as well as the associated Fourier transform ESEEM spectra for the succinate-reduced protein are shown as dashed lines in Figure 2(a) and 2(b), respectively. Strong low-frequency modulations arose from the reduced S-1 center at g = 1.935. The choice of τ value in the experiment was found to exert a profound effect on the relative intensities of the spectral lines, but the shifts of the line positions were negligible. Since the S-1 center will remain at the same redox state even when the enzyme is reduced by dithionite (see below), the data of the dithionite-reduced sample (solid line) are also shown here for comparison. The superhyperfine frequencies at 1.0 MHz, 1.9 MHz, 3.1 MHz, and 4.1 MHz are assigned to ν_0, ν_-, ν_+, and

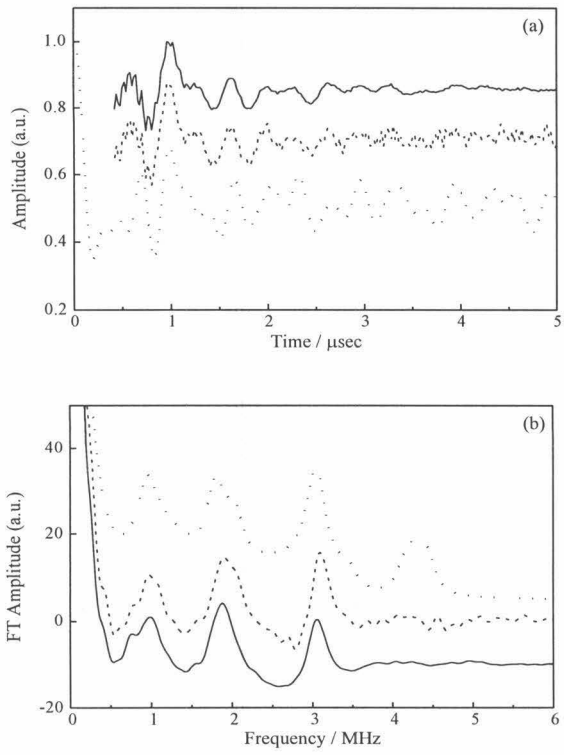

Figure 2. Stimulated ESEEM data (a) and associated Fourier transform (b) for the reduced [2Fe-2S] (S-1) cluster in the succinate-reduced (dashed line) and dithionite-reduced (solid line) *P. d.* SQR together with the corresponding simulations (dotted line). The spectra were offset for comparison. Measurement conditions were: microwave frequency, 9.24 GHz; magnetic-field strength, 3411 G (g = 1.935); pulse width, 25 ns; temperature, 4.2 K; τ value, 344 ns. Simulation parameters: A_{iso} = 1.2 MHz, r_{eff} = 3.7 Å, θ, ϕ = 77°, 30°, e^2qQ = 3.2 MHz, η = 0.6, and α, β, γ = 120°, 63°, 0°.

ν_{dq}, respectively, for the ESEEM spectrum at g = 1.935. The estimated coupling parameters are $A_{iso} \approx 0.7$ MHz, $e^2qQ \approx 3.32$ MHz, and $\eta \approx 0.6$. The magnitude of the hyperfine coupling here is somewhat larger than that deduced earlier for the S-3 center. Previous ESEEM studies of *E. coli* FRD [2Fe-2S] cluster also yielded 4-line spectra.[11] Similar results were also reported for the S-1 center in purified bovine heart SDH.[26]

The ESEEM spectrum of the semiquinone radicals (observed at g = 2.005) revealed more than 4 lines (Figure 3). Thus the analysis is more complicated than those of the S-1 and S-3 centers. Again, we repeated the experiments at two different τ values 285 ns (solid line) and 356 ns (dashed line), to ensure that all possible ESEEM peaks were observed. As mentioned in our previous study,[16] the radical signal arises primarily from the flavin semiquinone; the contribution from the two semiquinones bound to the hydrophobic peptides accounts for less than 25% of the EPR intensity.

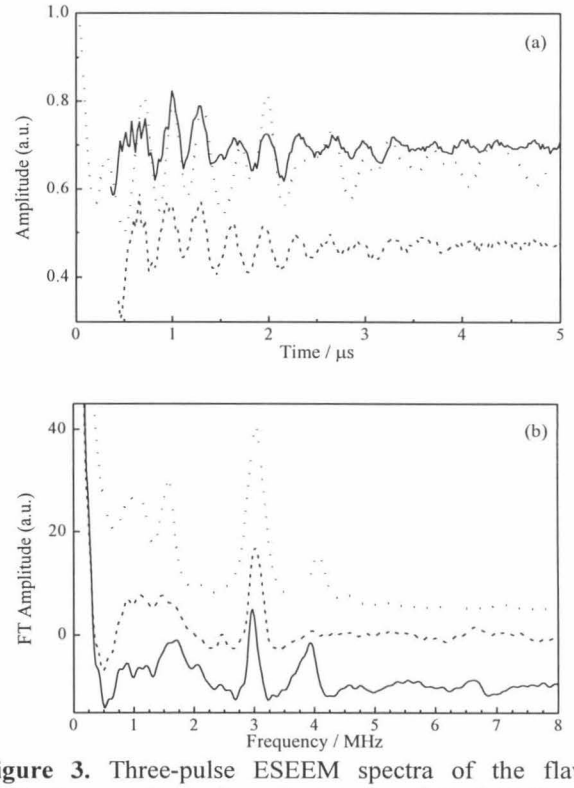

Figure 3. Three-pulse ESEEM spectra of the flavin semiquinone radical of succinate-reduced *P. d.* SQR. (a) Time-domain data of τ = 285 ns (solid line) overlaid with the corresponding simulation (dotted line) and τ = 356 ns (dashed line). (b) Fourier transform of the ESEEM data. Experimental conditions: microwave frequency 9.24 GHz at 3292 G magnetic field strength (g = 2.005); pulse width, 25 ns; temperature, 4.2 K. Simulation parameters for N(A): A_{iso} = 1.1 MHz, r_{eff} = 3.5 Å, θ, ϕ = 40 ~ 130°, 0 ~ 180°, e^2qQ = 3.1 MHz, η = 0.7, and α, β, γ = 90°, 10°, 0°. Simulation parameters for N(B): A_{iso} = 1.1 MHz, r_{eff} = 3.5 Å, θ, ϕ = 40 ~ 130°, 0 ~ 180°, e^2qQ = 3.24 MHz, η = 0.5, and α, β, γ = 10°, 90°, 0°.

Following earlier work,[22] we have attributed the observed ESEEM signals here to the two nitrogen nuclei on the flavin ring interacting weakly with the electron spin of flavin semiquinone. Tentatively, we have assigned the 0.88, 2, 2.98, and 3.93 MHz components to one ^{14}N nucleus and the 1.22, 1.71, 2.98, and 3.93 MHz components to the other. If this assignment is correct, the estimated A_{iso} (MHz), e^2qQ (MHz), and η would be 0.64, 3.24, 0.5, and 0.61, 3.14, 0.78, respectively. These ESEEM signals could not be attributed to the two nitrogens at positions 5 and 10 of the flavin ring, as high electron spin densities are predicted for these positions, and the corresponding hyperfine interaction parameters would be expected to be quite large, about 20 MHz for N(5) and 10 MHz for N(10).[22] The observed signals are more likely due to the other nitrogen nuclei in the isoalloxazine ring (positions 1 and 3), or to nitrogens of the protein that are close to the flavin ring. Flavin cofactors in the neutral semiquinone state of flavodoxin and ferredoxin-$NADP^+$ reductase (FNR) from *Anabaena* PCC 7119, and the anionic semiquinone state of cholesterol oxidase from *Brevibacterium sterolicum* have been studied previously using one- and two-dimensional ESEEM.[22] The nitrogens at positions 1 and 3 of the isoalloxazine ring were determined to have isotropic hyperfine coupling constants in the range of 1.2-1.3 and 0.7-0.8 MHz for the neutral semiquinone radicals.

Strikingly, the nuclear quadrupole coupling parameters obtained here are very close to the values of cholesterol oxidase semiquinones studied by Martínez *et al.* (e^2qQ = 3.25 MHz and η = 0.1).[22] However, the hyperfine coupling constants estimated above are somewhat smaller than the values they obtained (1.9 MHz). Further refinement of the parameters using spectral simulations will be described later.

Dithionite-reduced SQR — The dithionite-reduced enzyme revealed the EPR spectral features expected from the reduced S-1 center at $g_{\perp} = 1.935$ and $g_{||} = 2.022$, and the reduced S-2 center at $g \approx 2.27$. ESEEM measurements on this fully reduced SQR at $g = 1.935$ (solid lines in Figure 2) gave results essentially identical to the succinate-reduced protein (dashed lines in Figure 2). Therefore, we conclude that the spin density distribution at the reduced S-1 center is not affected by the electron spin at the reduced S-2 center, despite the magnetic dipolar interaction between these two spins hypothesized earlier.[16] In our previous work,[16] we observed that the reduction of the S-2 center causes a slight change to the EPR lineshape of the S-1 center, as well as an enhancement of the spin-lattice relaxation. There is clearly little or no re-organization of the ligand structure of the S-1 center upon reduction of the [4Fe-4S] cluster (S-2 center).

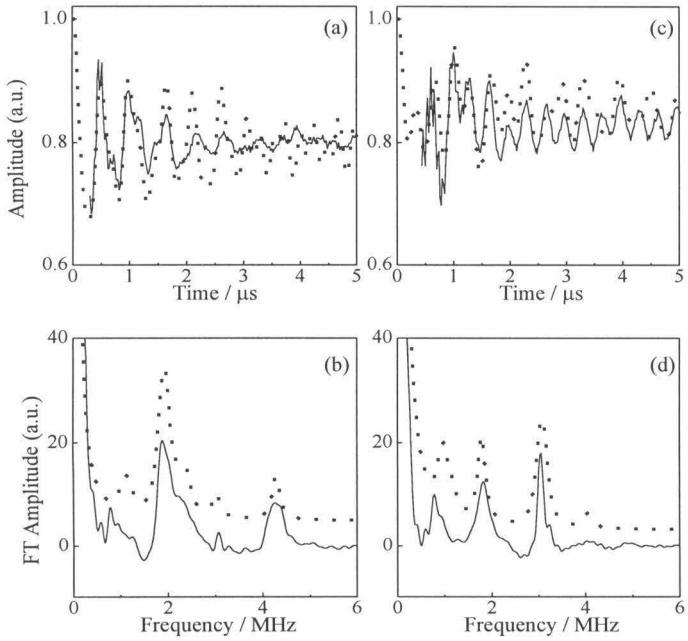

Figure 4. ESEEM spectra (solid line) and simulations (dotted line) of the dithionite-reduced [2Fe-2S] cluster at $g = 2.022$. (a) The stimulated modulation spectra and (b) the associated Fourier transform measured at $\tau = 215$ ns. (c) The stimulated modulation spectra and (d) the associated Fourier transform measured at $\tau = 359$ ns. Microwave frequency = 9.24 GHz; magnetic field = 3272 G; sample temperature = 4.2 K. Simulation parameters: $A_{iso} = 0.9$ MHz, $r_{eff} = 3.7$ Å, θ, $\phi = 0°$, 10°, $e^2qQ = 3.16$ MHz, $\eta = 0.55$, and α, β, $\gamma = 50°$, 50°, 30°.

Decreasing the magnetic field to record the ESEEM spectrum at $g = 2.022$ resulted in slight shifts of the modulation frequencies to 0.8, 1.8, 3.1, and 4.2 MHz

(Figure 4). The estimated coupling parameters A_{iso} (MHz), e^2qQ (MHz), and η are 0.85, 3.3, and 0.5, respectively. No ESEEM was observed for the reduced S-2 center because of its weak anisotropic absorption.[16] Finally, the high-frequency lines (between 5 and 8 MHz) that have been attributed to nitrogens coordinated to the Fe^{2+} site of the Rieske $[2Fe\text{-}2S]^4$ center are not observed here with SQR. This result argues against nitrogenous coordination of any one of the Fe-atom of the [2Fe-2S] cluster in SQR.

Refinement of the Superhyperfine Parameters

As indicated earlier, the values of A_{iso} for the oxidized S-3 and reduced S-1 centers and the semiquinone radicals are too small to meet the requirement for "exact cancellation." Further simulations of the spectra using the estimated hyperfine parameters as a starting point were then performed to refine the parameters within the limits of a spin Hamiltonian model and to improve our knowledge of the tensor orientations. The results are summarized in Table 1.

Table 1. ESEEM simulation parameters for oxidized S-3 center, reduced S-1 center, and flavin semiquinone in SQR from *Paracoccus denitrificans*.[a]

	e^2qQ (MHz)	η	α (deg)	β (deg)	γ (deg)	θ (deg)	ϕ (deg)	r_{eff} (Å)	A_{iso} (MHz)
Oxidized [3Fe-4S]	3.20	0.5	20	82	85	45	20	3.7	0.9
Reduced [2Fe-2S] $g_{\perp}$	3.20	0.6	120	63	0	77	30	3.7	1.2
Reduced [2Fe-2S] $g_{//}$	3.16	0.55	50	50	30	0	10	3.7	0.9
FAD• N(A)	3.10	0.7	90	10	0	40-130	0-180	3.5	1.1
FAD• N(B)	3.24	0.5	10	90	0	40-130	0-180	3.5	1.1

[a] Experimental parameters included in the simulation are specified below the figures.

S-3 Center — Values for the ^{14}N superhyperfine coupling parameters required to predict the observed modulation frequencies along with the appropriate relative amplitudes at g = 2.01 of the S-3 center and at different τ-values, are given in Table 1. A comparison of experimental and simulated ESEEM spectra is shown in Figure 1 for data collected at g = 2.01 with τ = 209 and 279 ns. S-3 time domain spectra (solid line) and the corresponding simulation (solid circles) at τ = 209 ns are shown in Figure 1(a); also shown are the corresponding experimental spectra and simulations for τ = 279 ns (dashed line and open circles). As can be seen, the modulation amplitudes decrease dramatically as τ increases from 209 ns (solid line) to 279 ns (dashed line). The associated Fourier transforms are compared in Figure 1(b).

We note here that the isotropic hyperfine constant A_{iso} obtained from the spectral simulation (0.9 MHz in Table 1) is almost twice the magnitude estimated earlier (0.48 MHz) from the condition of "exact cancellation." Thus, it is clear that "exact cancellation" was not obtained in our experiments. Nevertheless, our original estimates of e^2qQ (3.5 MHz) and η (0.44) are quite close to the values obtained by spectral simulation (e^2qQ = 3.2 MHz and η = 0.5).

S-1 Center — The results of the simulations on reduced S-1 at g = 1.935 and 2.022 are shown as dotted lines in Figures 2 and 4, respectively. The ^{14}N quadrupole parameters were determined as e^2qQ = 3.2 MHz and η = 0.5. The magnitude of A_{iso}, determined by simulation of the data at 3411 G and 3272 G (Figure 2 and 4), decreased from 1.2 to 0.9 MHz, while the quadrupole coupling parameter e^2qQ and the asymmetry parameter η remained unchanged. Also, depending on whether the data at $g_\perp$ (1.935) or $g_{||}$ (2.022) were used in the spectral simulations, a different set of values was obtained

for the angles θ and ϕ that relate the relative orientation of the nuclear hyperfine tensor to the g tensor. Physically, the two sets of data should yield the same θ and ϕ. However, the data from $g_{||}$ (2.022) is likely to be compromised by spectral interference from the reduced S-2 signal, so the θ and ϕ deduced from these data are expected to be less reliable. Simulation of the spectral data for $g_{\perp}$ yielded as best fits ~80° and 30° for θ and ϕ, respectively. The angle between the largest principal component of the electric field gradient (q) and g_z is described by the Euler angle β, which was determined to be 60° and 50° for $g_{\perp}$ and $g_{||}$, respectively.

Flavin radical — Figure 3 compares the simulated (dotted lines) and experimental spectra (solid and dashed lines) of the flavin radical in the time domain as well as the Fourier transforms of these spectra. As mentioned in the previous section, we attribute the ESEEM signals to the two nitrogens on the flavin ring, as in earlier studies on flavin semiquinone radicals. With two nitrogen nuclei, there will be more adjustable parameters in the simulations than in the case when the electron is coupled to only one nucleus. We have used the same program to simulate this ESEEM signal that was used to simulate the ESEEM of anisotropic signals discussed earlier (i.e., the signals of the S-1 and S-3 centers), even though this radical signal is rather isotropic. The g values of the radical signal used in the present simulations are 1.9828, 1.9989, and 2.00586 for g_x, g_y, and g_z, respectively. Finally, it is assumed that the unpaired electron is essentially localized on N(5) of the flavin ring (Figure 5) in the simulations. As a σ-radical, we expect only a small delocalization of the spin density onto other atoms.

The simulation results showed that the θ′s of both nitrogen nuclei range from 40° to 130°, but the ϕ′s have a wider range of acceptable values that will yield an acceptable

fit. Therefore, the ESEEM spectra of this radical are not very sensitive to the orientation of the A-tensor, as expected for an isotropic signal. The nuclear quadrupolar parameters (e^2qQ's) obtained from simulations for the two nitrogen nuclei are also similar (e^2q_AQ = 3.1 MHz, and e^2q_BQ = 3.24 MHz). However, the directions of q_A and q_B, the largest principal component of the electric field gradient, are significantly different for the two nitrogens. The angle between the orientations of q_A and q_B is roughly 90° (β_A = 10° and β_B = 90°). A possible set of parameters that would account for the observed ESEEM data is listed in Table 1. As can be seen in Figure 3, the simulated time-domain spectrum and Fourier transform are in good agreement with experiment.

The two nitrogen nuclei, N(A) and N(B) that interact with the unpaired electron spin to yield the ESEEM signal are most likely the two nitrogens indicated by arrows in Figure 5, namely N(1) and N(3). The lone pair electron on N(1) is in the plane of the flavin ring, so that q for this nitrogen should be oriented in the direction of the lone pair. In contrast, N(3) is three-coordinated, so that q here should be oriented perpendicular to the plane. Thus, the principal axis q's for these two nuclei should differ by 90°, as observed. As expected, the magnitudes of the ^{14}N nuclear quadrupolar parameters deduced for the two nitrogen nuclei are rather similar.

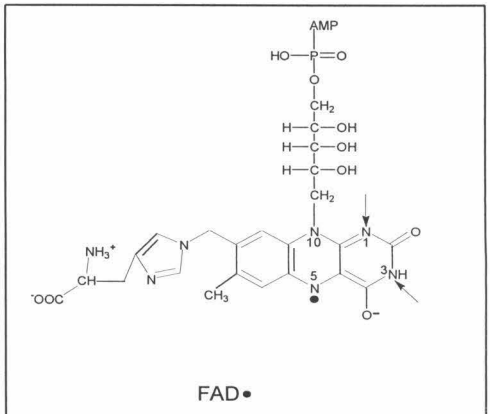

FAD•

Figure 5. Structures of 8α-[N(3)-histidyl] FAD in the anionic semiquinone state. Arrows indicate positions of the isoalloxazine ring nitrogens that interact with the unpaired spin to yield the observed ESEEM signals.

Since the ubisemiquinone radicals account for less than 25% of the total composite (FAD• plus semiquinone radicals) signal, its contribution to the ESEEM spectra was ignored in the analysis above. While we cannot rule out the possibility of some weak modulations arising from the ubisemiquinone radicals, we were able to simulate the composite spectrum successfully without their inclusion. As noted earlier, the agreement between the simulated and experimental spectra is in fact very good.

Effects of e^2qQ, η and r_{eff} on the Simulated Fourier Transforms of the ESEEM Spectra

Since the ^{14}N nuclear quadrupole interaction is stronger than the nuclear Zeeman and superhyperfine splitting interactions in the case of reduced S-1 and oxidized S-3 centers, the positions of the peaks in the ESEEM spectra are more sensitive to e^2qQ and η than the other parameters. Figure 6 shows simulations of the Fourier transforms of the ESEEM spectra in which e^2qQ, η and r_{eff} are varied independently. In Figure 6(a), we see that the higher frequency peaks (>1.5MHz) in the ESEEM spectrum scale with the value of e^2qQ, whereas

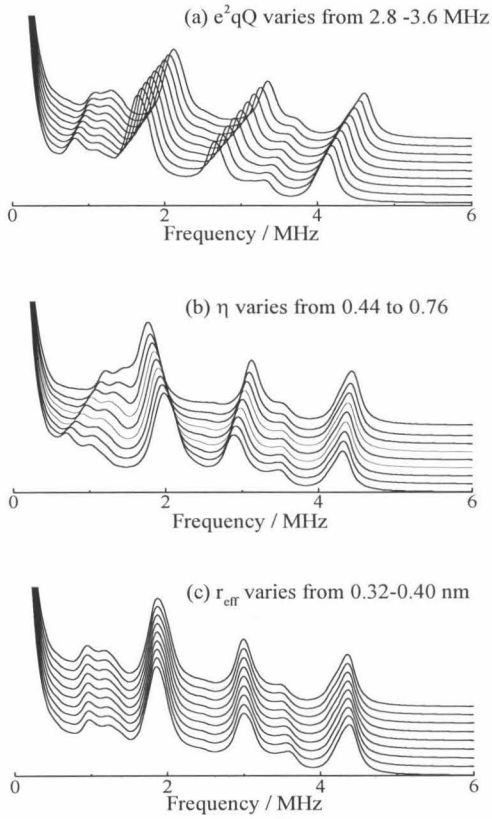

Figure 6. Effects of (a) e^2qQ (from 2.8 to 3.6 MHz), (b) η (between 0.44 and 0.76), and (c) r_{eff} (between 3.2 and 4.0 Å) on simulated Fourier transforms of three pulse echo data for the reduced S-1 center. Other parameters are given in the legend of Figure 2.

the lower frequency peaks (<1.5MHz) appear to remain stationary. As η is increased, however, the lower frequency peaks do move closer together (Figure 6(b)). These trends can be understood on the basis of eqs 1 and 2. Finally, Figure 6(c) demonstrates that the changes in r_{eff} have little effect on the spectrum except to change the apparent linewidth of the peaks.

Comparison of SQR from P. d. with A. m. SQR and E. coli FRD

Table 2 shows a comparison of the hyperfine and quadrupolar parameters of the S-1, S-3 centers, and the flavin semiquinone radical from different species. The coupling parameters (A_{iso} and e^2qQ) for *A. m.* SQR and *E. coli* FRD were previously determined from the highest frequency lines of the four-line ESEEM pattern (that is, the $\Delta m_I = 2$ transitions).[11,12]

Comparing the coupling parameters of S-1 and S-3 in *A. m.* SQR and in *P. d.* SQR, we note that these parameters, and hence the ligand structures of the S-1 and S-3 centers in the reduced and oxidized states of the protein, respectively, are very similar in the different species. Also, despite the fact that SQR and FRD are complex flavoproteins that catalyze the reverse enzymatic reactions *in vivo*, the data in Table 2 suggest only slight differences in the ligand structure of the S-1 and S-3 centers between SQR and FRD (see next section).

The hyperfine parameters of the flavin semiquinone in SQR are similar to the neutral semiquinone states of flavodoxin and ferredoxin-$NADP^+$ reductase (FNR) from cyanobacterium *Anabaena* PCC7119 (actually, one of the hyperfine parameters is similar to and the other is larger than that of the neutral semiquinone). The anionic

semiquinone state of cholesterol oxidase has a higher hyperfine parameter. However, Edmondson *et al.*[27] have suggested that the flavin radical in SQR is actually in the anionic form. In our previous CW EPR measurements,[16] we have also concluded that the linewidth of the flavin radical (12 G) is consistent with an anionic flavin radical. Since these hyperfine interactions are weak, they might not provide a good indication of the ionic states of flavin semiquinone.

Table 2. Hyperfine and quadrupolar parameters of SQR S-1, S-3 centers, and flavin semiquinone, compared with those of SDH and FRD in different species.

	A_{iso} (MHz)	e^2qQ (MHz)	η	Ref.
Reduced [2Fe-2S] $g_{1.935}$				
P. d. SQR	1.20	3.20	0.6	This work
A. m. SQR [a]	1.11	3.32	0.5 [b]	11
E. coli FRD [a]	1.06	3.41	0.5 [b]	11
E. coli FRD [a]	1.10	3.30	0.5	5
S. platensis ferredoxin	1.01	3.52	0.5 [b]	11
Oxidized [3Fe-4S]				
P. d. SQR	0.90	3.20	0.5	This work
A. m. SDH	0.82	3.24	0.5 [b]	11
E. coli FRD	0.6	3.36	0.5 [b]	11
Bovine heart SQR	0.48	nd	nd	13
Flavin semiquinone				
P. d. SQR	1.1, 1.1	3.10, 3.24	0.7, 0.5	This work
Anabaena flavodoxin	1.3, 0.8	3.32, nd [c]	0.5, nd [c]	22
Anabaena FNR	1.2, 0.7	3.32, nd [c]	0.5, nd [c]	22
B. sterolicum cholesterol oxidase	1.9, 0.7	3.32, nd	0.5 [b], nd	22

[a] Data were obtained in the fully-reduced state of the protein.
[b] The quadrupolar coupling constant (e^2qQ) was determined using a fixed asymmetry parameter of 0.5.
[c] Estimated from values obtained for cholesterol oxidase.

The e^2qQ values for S-1 and S-3 centers in SQR are almost identical to those obtained with peptide nitrogens (e^2qQ = 3.0-3.4 MHz, η = 0.4-0.5).[28,29] The only other

amino acid with an ^{14}N site with similarly large quadrupolar couplings is the imino nitrogen of histidine (e^2qQ = 3.36 MHz with η = 0.13), though the value of this coupling constant decreases upon coordination to metals[30] and the value of η is too small. Therefore the most likely assignment for the low-frequency ESEEM of SQR S-1 and S-3 centers is coupling between the cluster and a distant ^{14}N of the polypeptide chain in each case. Finally, a comparison of the experimentally obtained modulation depths with those predicted by simulations indicates that only one nitrogen may be involved.

Insights from Crystal Structure of FRD from E. coli

The IP polypeptide of SQR and FRD contains three groups of cysteine residues, which are ligands to the three iron-sulfur clusters. The N-terminal domain harbors the [2Fe-2S] (S-1/FR-1) center, which is ligated by a CxxxxCxxC.....C (C57, C62, C65, and C77 in FRD of *E. coli*) motif, although the third cysteine is not fully conserved. The C-terminal domain ligates the [4Fe-4S] (S-2/FR-2) and [3Fe-4S] (S-3/FR-3) centers and contains the cysteine residues that are arranged in the sequence as CxxCxxCxxxCP (C148, C151, C154, and C158 in FRD of *E. coli*) followed by CxxxxxCxxxCP (C204, C210, and C214 in FRD of *E. coli*). In this motif, the first three cysteines in the first group and the last cysteine in the sequence are ligands to the S-2 center, whereas the remaining cysteines are ligands to the S-3 center. The structure of IP in FRD and SQR in the various organisms seems very well conserved.

According to the 2.8 Å crystal structure data of the FRD from *E. coli*, several nitrogens are in close proximity to the two iron atoms of the FR-1. These are listed in Table 3, with the amino acids in the FR-1 from FRD and the corresponding amino acids

in the S-1 center of SQR based on sequence alignments. As can be seen here, the possible nitrogens interacting with the iron atoms of S-1/FR-1 are from the same kind of amino acids for either SQR or FRD. Therefore, the FR-1 and S-1 centers do have similar protein environments.

Table 3. The distances between proximal nitrogen atoms and the iron atoms of the [2Fe-2S] (S-1/FR-1) cluster based on the crystal structure of FRD from *E. coli*.[14]

Residues **FRD**	in **SQR**	nitrogen	Distance to Fe1 (Å)	Distance to Fe2 (Å)
S56	S78	N	5.51	4.44
C57	C79	N	5.64	3.60
R58	R80	N	4.66	3.8
		NE	8.98	8.36
		NH	9.92	9.06
		NH	10.74	9.89
M59	E81	N	5.07	4.74
A60	G82	N	4.19	4.25
I61	I83	N	5.30	4.10
C62	C84	N	5.71	3.53
G63	G85	N	4.97	3.51
S64	S86	N	4.78	4.24
C65	C87	N	4.18	5.03
G66	A88	N	5.91	7.38
L75	L97	N	6.80	9.17
A76	A98	N	5.39	8.00
C77	C99	N	4.16	6.83
K78	I100	N	5.60	8.05
		NE	8.97	10.29

In the ESEEM spectra of the reduced S-1 center, the superhyperfine coupling arises from magnetic coupling between the S-1 center and a peptide nitrogen. From a comparison of modulation depths observed experimentally and predicted by the simulations, it appears that only one nitrogen is involved in this superhyperfine interaction. From the crystal structure of FRD (Table 3), the backbone nitrogens from

Cys57, Cys62, and Gly63 (the first two cysteines in the motif and the somewhat conserved glycine) are in the closest proximity to one of the iron atoms (3.6, 3.53, and 3.51 Å, respectively). Most likely, it is the peptide ^{14}N of Gly63 that gives rise to the ESEEM spectrum.

Only a weak superhyperfine interaction is observed for the S-3 center with a peptide nitrogen, as suggested from our simulations. In the FRD crystal structure, most of the nitrogens around the FR-3 center are > 4Å away from the iron atoms, with the sole exception of the backbone nitrogen of Gly208 (3.94 Å away from one of the irons in the cluster). In SQR, this nitrogen would correspond to the backbone nitrogen of methionine 230 in SQR from *P. d.*. However, as shown in Table 4, the amino acid residues around the S-3/FR-3 center are not as well conserved as that for the S-1/FR-1 center based on our sequence alignments.

Table 4. The distances between proximal nitrogen atoms to the iron atoms of the [3Fe-4S] (S-3/FR-3) cluster based on the crystal structure of FRD from *E. coli*.[14]

Residue **FRD**	in **SQR**	nitrogen	Distance to Fe1 (Å)	Distance to Fe2 (Å)	Distance to Fe3 (Å)
C158	C179	N	6.1	7.62	5.2
P159	P180	N	6.86	7.47	5.26
Q160	S181	N	7.32	7.0	5.2
		NE	6.31	7.01	6.34
F161	Y182	N	7.65	7.44	5.26
C204	C226	N	7.66	5.27	6.34
T205	H227	N	6.64	4.49	5.79
F206	T228	N	5.64	4.16	6.04
V207	I229	N	4.78	4.44	5.36
G208	M230	N	3.94	5.04	5.47
Y209	N231	N	4.74	6.76	6.26
C210	C232	N	4.22	6.70	5.76
S211	T233	N	5.39	7.67	7.46
A221	A243	N	5.48	6.46	7.51
I224	I246	N	8.21	7.54	9.34

Clearly, the protein environments of S-1/FR-1 and S-3/FR-3 must vary with the functions of these clusters in these respective enzymes. In particular, the mid-point potentials of the respective iron-sulfur clusters must vary depending on the function of the enzyme. The S-1 center is most likely the first electron acceptor after the flavin in SQR, whereas the FR-1 must be the electron donor to the flavin in FRD. It follows then that the clusters in SQR must have a higher redox potential than those in FRD, if the redox potential of the flavin is the same in the two enzymes, which appears to be the case. However, the FR-1 and the S-1 centers appear to have similar protein environments as suggested by the ESEEM data and the crystal structure. Accordingly, their redox potentials should differ in a minor way. (The redox potential of the S-1 and FR-1 are ~0 mV and –20 mV, respectively.)[8,10,31] On the other hand, the protein environments around the S-3 center in SQR and the FR-3 center in FRD are clearly different. In line with this, the redox potentials of the S-3 (+60 mV) in SQR[10,32] and FR-3 in FRD (-50 mV)[10] are substantially different. Therefore, the chemistry is determined by the direction of the electron flow, which, in turn, is controlled by the relative redox potential between the S-1 and S-3 centers in SQR, and between the FR-3 and FR-1 centers in the case of FRD, in accordance with the function of the respective enzymes.

Conclusions

We have undertaken a detailed analysis of the ESEEM spectra of the reduced S-1 center, oxidized S-3 center, and the flavin semiquinone radical in SQR in order to deduce the ligand hyperfine and nuclear quadrupole tensors. The experiments on the S-1 and S-3 centers are intended to define the protein environments of these metallic

cofactors. A program based on the density matrix formalism of Mims was used to simulate the observed spectra. All the data were fitted reasonably well by the Mims Hamiltonian, thus providing reliable determination of the nitrogen hyperfine and quadrupole coupling parameters. The ESEEM spectra of both S-1 and S-3 centers derived from the stimulated echo envelope contain four lines, together with a modulation depth corresponding to one coupled nitrogen nucleus. The nuclear quadrupole tensors are consistent with an interaction between the unpaired electron spin of the iron-sulfur cluster and a weakly coupled peptide ^{14}N nucleus in each case.

Except for the work by Cammack *et al.*[5] on the FRD from *E. coli*, in all earlier ESEEM studies, the hyperfine and quadrupolar parameters of the [2Fe-2S] and [3Fe-4S] clusters were obtained simply by assuming that the highest frequency components of the four-line ESEEM pattern arose from the $\Delta m_I = 2$ transitions. No ESEEM spectral simulations were performed. In the present study, we have carried out thorough simulations on the ESEEM spectra of these metallic cofactors as well as on flavin semiquinone to ascertain the reliability of the analysis.

When the present results on *P. d.* SQR are compared with ESEEM studies previously reported on purified *E. coli* FRD [2Fe-2S] and [3Fe-4S] centers, *A. m.* SQR submitochondrial membrane particles [2Fe-2S] and [3Fe-4S] centers, and purified bovine heart SQR [3Fe-4S] center, similar ligand structures are suggested for both sets of metal clusters. While these conclusions seem to be supported by the recent x-ray structure of FRD from *E. coli* in the case of the [2Fe-2S] cluster, the protein environments are substantially different between the [3Fe-4S] center in *P. d.* SQR and in

E. coli FRD. Therein lies the difference in the redox potential between the [3Fe-4S] clusters and the function of the two related enzymes.

Finally, based on the ^{14}N hyperfine coupling parameters of the flavin semiquinone, the ESEEM signals are due to the interaction of nitrogens N(1) and N(3) of the flavin isoalloxazine ring with the electron spin of the flavin semiquinone.

References

(1)Tsvetkov, Y. D.; Dikanov, S. A. *Electron-spin echo - Applications to biological systems*; Sigel, H., Ed., 1987; Vol. 22, pp 207.

(2)Cline, J. F.; Hoffman, B. M.; Mims, W. B.; LaHaie, E.; Ballou, D. P.; Fee, J. A. *J. Biol. Chem.* **1985**, *260*, 3251.

(3)Telser, J.; Hoffman, B. M.; LoBrutto, R.; Ohnishi, T.; Tsai, A. L.; Simpkin, D.; Palmer, G. *FEBS Lett.* **1987**, *214*, 117.

(4)Britt, R. D.; Sauer, K.; Klein, M. P.; Knaff, D. B.; Kriauciunas, A.; Yu, C.-A.; Yu, L.; Malkin, R. *Biochemistry* **1991**, *30*, 1892.

(5)Cammack, R.; Chapman, A.; McCracken, J.; Cornelius, J. B.; Peisach, J.; Weiner, J. H. *Biochim. Biophys. Acta* **1988**, *956*, 307.

(6)Peisach, J.; Orme-Johnson, N. R.; Mims, W. B.; Orme-Johnson, W. H. *J. Biol. Chem.* **1977**, *252*, 5643.

(7)Ohnishi, T. *Curr. Top. Bioenerg.* **1987**, *15*, 37.

(8)Ackrell, B. A. C.; Johnson, M. K.; Gunsalus, R. P.; Cecchini, G. *Structure and function of succinate dehydrogenase and fumarate reductase*; Müller, F., Ed.; CRC Press: Boca Raton, 1992; Vol. III, pp 229.

(9)Hederstedt, L.; Ohnishi, T. *Progress in succinate:quinone oxidoreductase research*; Ernster, L., Ed.; Elsevier Science Publishers: Amsterdam, 1992, pp 163.

(10)Hägerhäll, C. *Biochim. Biophys. Acta* **1997**, *1320*, 107.

(11)Shergill, J. K.; Cammack, R. *Biochim. Biophys. Acta* **1994**, *1185*, 43.

(12)Shergill, J. K.; Cammack, R.; Weiner, J. H. *J. Chem. Soc., Faraday Trans.* **1993**, *89*, 3685.

(13)Ackrell, B. A. C.; Kearney, E. B.; Mims, W. B.; Peisach, J.; Beinert, H. *J. Biol. Chem.* **1984**, *259*, 4015.

(14)Iverson, T. M.; Luna-Chavez, C.; Cecchini, G.; Rees, D. C. *Science* **1999**, *284*, 1961.

(15)Lancaster, D. R. D.; Kroeger, A.; Auer, M.; Michel, H. *Nature* **1999**, *402*, 377.

(16)Waldeck, A. R.; Stowell, M. H. B.; Lee, H. K.; Hung, S.-C.; Matsson, M.; Hederstedt, L.; Ackrell, B. A. C.; Chan, S. I. *J. Biol. Chem.* **1997**, *272*, 19373.

(17)Sturgeon, B. E.; Britt, R. D. *Rev. Sci. Instrum.* **1992**, *63*, 2187.

(18)Flanagan, H. L.; Singel, D. J. *J. Chem. Phys.* **1987**, *87*, 5606.

(19)Reijerse, E. J.; Keijzers, C. P. *J. Magn. Reson.* **1987**, *71*, 83.

(20)Medina, M.; Cammack, R. *J. Chem. Soc., Perkin Trans.* **1996**, *2*, 633.

(21)Medina, M.; Vrielink, A.; Cammack, R. *FEBS Lett.* **1997**, *400*, 247.

(22)Martínez, J. I.; Alonso, P. J.; Gómez-Moreno, C.; Medina, M. *Biochemistry* **1997**, *36*, 15526.

(23)Mims, W. B. *Physical Review B* **1972**, *5*, 2409.

(24)Hurst, G. C.; Henderson, T. A.; Kreilick, R. W. *J. Am. Chem. Soc.* **1985**, *107*, 7294.

(25)Cornelius, J. B.; McCracken, J.; Clarkson, R. B.; Belford, R. L.; Peisach, J. *J. Phys. Chem.* **1990**, *94*, 6977.

(26)LoBrutto, R.; Haley, P. E.; Yu, C. A.; Ohnishi, T.; Leigh, J. S. *Biophys. J.* **1986**, *49*, 327a.

(27)Edmondson, D. E.; Ackrell, B. A. C.; Kearney, E. B. *Arch. Biochem. Biophys.* **1981**, *208*, 69.

(28)Edmonds, D. T.; Speight, P. A. *Phys. Lett.* **1971**, *34A*, 325.

(29)Hunt, M. J.; Mackay, A. L. *J. Magn. Reson.* **1976**, *22*, 295.

(30)Ashby, C. I. H.; Cheng, C. P.; Brown, T. L. *J. Am. Chem. Soc.* **1978**, *100*, 6057.

(31)Bonomi, F.; Pagani, S.; Cerleti, P.; Giori, C. *Eur. J. Biochem.* **1983**, *134*, 439.

(32)Ohnishi, T.; Lim, J.; Winter, D. B.; King, T. E. *J. Biol. Chem.* **1976**, *251*, 2105.

Chapter 5:

The Trinuclear Copper(II) Clusters of the Particulate Methane Monooxygenase from Methanotrophic Bacteria: Electron Paramagnetic Resonance Spectral Simulations

Abstract

The particulate methane monooxygenase from *Methylococcus capsulatus* contains 15 reduced copper ions, and it has been proposed that these copper ions are arranged in the form of trinuclear clusters. Two of these clusters have been referred to as C-clusters, and have been implicated in dioxygen activation and alkane hydroxylation. The remaining three clusters are called E-clusters, and it appears that they provide a buffer of reducing equivalents to replenish the electrons at the C-clusters following dioxygen activation at the C-clusters during turnover. When the copper ions are oxidized, they exhibit a nearly isotropic EPR signal centered near g = 2.1. It has been argued that this EPR signal corresponds to ferromagnetically exchange-coupled trinuclear Cu(II) clusters with $J \approx 20$ cm^{-1} and $D \leq 0.05$ cm^{-1}. Toward confirming these results, several triangular model complexes, both antiferromagnetically and ferromagnetically coupled, and with well-defined structural and ligand information, were reviewed to gain insights into magneto-structural correlations. Spectral simulations of the pMMO cluster EPR signal were then performed based on the structural and spectroscopic information provided by the ferromagnetic model complexes. We show that only Cu(II) ions with proper g-tensors and appropriate relative orientations between them can give rise to the unique EPR signal observed for the E- and C-clusters in pMMO.

Introduction

Many multicopper-containing oxidases and monooxygenases are known in nature. The best characterized oxidases include laccase,[1-4] ceruloplasmin,[5] and ascorbate oxidase,[6,7] where the x-ray structures have been determined and a good deal of information is known about structure and function. Considering each oxidase, the oxidation of an organic substrate is linked to the reduction of dioxygen. The latter chemistry involves a cluster of three reduced copper ions, although other copper ions, particularly blue copper(s) are often also involved in shuttling reducing equivalents from the substrate to the trinuclear copper cluster(s). Among the monooxygenases, tyrosinase perhaps is the best understood.[8] The active site here involves only a pair of reduced copper ions, which not only activates molecular oxygen but also mediates the ultimate transfer of one of the oxygen atoms to the tyrosine substrate to form the catechol at the catalytic center. Recently, similar chemistry has also been suggested at the catalytic site of the membrane-bound (particulate) methane monooxygenase (pMMO).[9-13] Here, a pair of reduced trinuclear copper clusters are implicated: dioxygen chemistry takes place at both cluster; however, the oxo-transfer chemistry is thought to involve insertion of an "oxene" into the C-H bond during the conversion of methane to methanol at one of the copper clusters. Thus, the dioxygen chemistry in pMMO appears to mimic that of the multi-copper oxidases whereas the oxo-transfer chemistry mimics that of tyrosinase.

Although all of the above oxidases and the methane monooxygenase seem to involve trinuclear copper clusters in the activation of dioxygen at the active site, the details of the chemistry mediated appear to be very different. In the case of the oxidases, the copper cluster catalyzes the conversion of dioxygen to two water molecules. In the

case of methane monooxygenase, two trinuclear copper clusters are apparently involved. One of the copper clusters catalyzes the oxo-transfer to a C-H bond, and the reduction of the second oxygen atom forms a water molecule. The other copper cluster appears to mediate dioxygen chemistry only, with the fourth electron originating apparently from the C-cluster where the alkane hydroxylation occurs. Accordingly, the details of the trinuclear copper clusters need not be the same. As a matter of fact, the catalytic site(s) in the case of methane monooxygenase appears to involve fairly symmetrical trinuclear copper(I) clusters.[9-11] On the other hand, in the case of the multicopper oxidases, the copper cluster has been shown to involve a reduced type 2 copper site in close proximity to a reduced type 3 binuclear copper site.[6-8] In other words, the geometrical disposition of the three copper ions is intrinsically different at the active site(s) between the two types of enzymes.

It has been proposed that when the trinuclear copper clusters of methane monooxygenase are fully oxidized, each of the oxidized clusters consists of three type 2 copper centers that are mutually weakly ferromagnetically coupled ($J \approx 20$ cm^{-1}).[9] In contrast, when the copper ions in the corresponding cluster of laccase, ascorbate oxidase, or ceruloplasmin are oxidized, one observes a type 2 copper(II) site that is at most weakly coupled to a pair of type 3 copper ions that are strongly antiferromagnetically coupled through a bridging hydroxyl ligand. Thus, variations in catalytic activity may have origin in the detailed ligand structures of the copper ions in the cluster.

Electron paramagnetic resonance (EPR) spectroscopy has proven to be one of the most powerful tools in classifying the various copper sites in multicopper oxidases, and similarly EPR is proving to be useful in defining the various copper sites in pMMO.

Unfortunately, in the case of pMMO, there are far too many copper ions, and they all seem to be grouped into trinuclear clusters of rather similar structure. Accordingly, in the fully oxidized enzyme, the EPR spectrum of the copper ions is a composite of heterogeneous contributions from several trinuclear copper clusters at the same time. This general picture has been confirmed by magnetic susceptibility measurements on the fully oxidized protein. Some progress has also been made by exploiting the differential reactivity of the C-clusters and E-clusters toward dioxygen and NO as followed by EPR characterization of the reaction products formed at the C-clusters while the E-cluster copper ions remain reduced. Nevertheless, further insights could be derived from the EPR if the correlation of the motions of the spins associated with the copper ions in the oxidized clusters could be understood in structural and electronic terms.

This paper focuses on the EPR of the C-clusters in the pMMO, namely the two trinuclear copper clusters that are involved in dioxygen activation and alkane hydroxylation. Since the biological activity of pMMO is rather unique, and there is certainly no precedent for the EPR spectrum that we have observed for the oxidized pMMO Cu clusters in metalloenzymes, we have decided to appeal to model compounds of trinuclear copper(II) clusters with well-defined ligand structures and geometry that have already been reported in the literature. Specifically, we shall compare the EPR spectra observed for the C-clusters of pMMO with those of model trinuclear copper(II) clusters and use this exercise to derive some insights into the possible ligand structures present within the trinuclear copper clusters in pMMO. We shall fine tune the spin Hamiltonian parameters for the copper ions in these clusters via computer simulations.

Finally, we conclude this study with some computer simulations of the E-clusters as well.

Cluster Models

The chemistry of trinuclear copper(II) complexes has drawn considerable interest following their identification as the active sites of oxidases and oxygenases.[1-10,12] Over the years, however, there has also been much interest in these complexes for the development of new inorganic materials showing molecular ferromagnetism.[14-16] Thus, many triangular Cu_3 complexes have been reported.[17-37] Examples of some equilateral triangular copper clusters are shown in Figure 1. Depending on the coordination geometry of the copper ions in the clusters and the degree of potential "overlap" of the

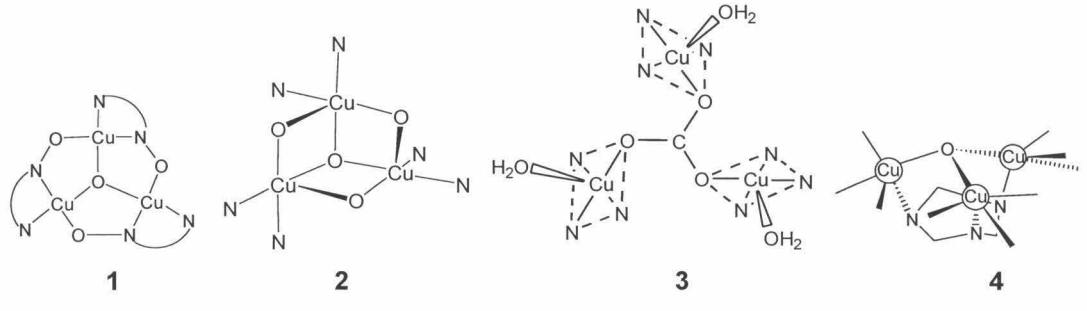

Figure 1. Molecular structures of equilateral triangular Cu(II) clusters: **1** taken from ref. 19; **2** taken from ref. 22; **3** taken from ref. 36; and **4** taken from ref. 32.

d-orbitals containing the unpaired electron spins, these complexes exhibit varying degrees of exchange interaction, both antiferromagnetic and ferromagnetic. Thus, the model complexes **1**[18,19] and **2**[22,23] in Figure 1 exhibit antiferromagnetic interactions among the Cu(II) ions, whereas complex **3** and **4** show ferromagnetic interactions.[32,36] In **1** and **2**, the Cu(II) ions adopt square pyramidal coordination with the $(d_{x^2-y^2})^1$ ground "hole" states. The strong antiferromagnetic interaction ($J = -61$ to -500 cm^{-1}) in **1** is due

to the effective overlap of the magnetic $d_{x^2-y^2}$ orbitals arising from the coplanarity of the coordination planes of the three subunits. Compound **2** displays a much weaker magnetic interaction (J = –12 to –15 cm^{-1}) than **1**. In **2**, bridging O atoms coordinate pairs of penta-coordinated copper atoms in an axial-equatorial arrangement, and a central O (or OH) bridge constrains the coordination planes to be orthogonal to each other. Thus, the overlap of the magnetic orbitals, either through the pairwise bridging O ligands or the central O bridge, is weaker.[22,23] It is evident that the magnitude of the magnetic coupling in these triangular Cu(II) complexes strongly depends on the overall degree of coplanarity of the ligand frameworks associated with each of the copper ions.

Compound **3** belongs to the class of trinuclear Cu(II) clusters where a carbonate anion serves as a tridentate bridge.[35-38] Here, the coordination environment of each copper ion is also square pyramidal so that each copper ion has the $(d_{x^2-y^2})^1$ ground "hole" states, as those in **1** and **2** (squares are drawn by dashed line in Figure 1). However, the interaction among the Cu(II) ions is weakly ferromagnetic, and the complex exhibits a S = 3/2 quartet ground state, similar to that proposed for the C-cluster in pMMO. According to Khan,[39] the exchange coupling constant J can be expressed as a sum of both ferromagnetic (J_F) and antiferromagnetic (J_{AF}) contributions $J = J_F + J_{AF}$. Both the antiferromagnetic and ferromagnetic contributions become attenuated when the metal ions are bridged by extended polyatomic ligands. However, the antiferromagnetic contribution is typically only important when there is direct overlap between the magnetic orbitals centered on nearest-neighbor metal ions, where it is then proportional to the square of the overlap integral between magnetic orbitals. In **1** and **2**, the exchange coupling is provided by a single bridging O, and the Cu-O-Cu pathway offers efficient

overlap of magnetic orbitals on adjacent Cu(II) ions to mediate a strong antiferromagnetic exchange interaction. In **3**, the *syn-anti* arrangement of the O atoms in the carboxylate anion predisposes the 2p-orbitals of the oxygen atoms on the bridging carboxylate to an unfavorable overlap.[36] In addition, the CuN_3O planes are tilted with respect to the practically planar CO_3Cu_3 fragment by an average dihedral angle of 61.5° so that the equatorial planes of adjacent copper ions form average dihedral angles of 80.9°. This non-coplanarity is expected to decrease the overlap of the magnetic orbitals in the bridging region further and to lower the antiferromagnetic interaction. Accordingly, the ferromagnetic contribution becomes more dominant (J = 6 to 8 cm^{-1}), as revealed by magnetic susceptibility measurements.

On the other hand, the ligand geometry of each Cu(II) ion in compound **4** is best described as a distorted trigonal bipyramid, which leads to a d_{z^2} ground "hole" state.[32] The Cu-O-Cu angles in this complex (112–113°) are also larger compared to those of the other two complexes. A fairly strong ferromagnetic interaction (J = 54.5 cm^{-1}) among the copper ions in compound **4** was concluded from magnetic susceptibility measurements. However, an analysis of the superexchange pathway(s) that might lead to the observed ferromagnetic coupling among the copper ions is not straightforward.

Trinuclear Cu(II) complexes exist also as isosceles triangular complexes. Most show the doublet ground state, and only one complex has been shown to exhibit the quartet ground state. Figure 2 shows two examples of such model complexes. Complex **5** exhibits a total spin S = 1/2 for the ground state,[25] while complex **6** has a quartet ground state.[28,40] In both complexes the environment around the Cu(II) ions is distorted square pyramidal so that the magnetic orbitals centered on the Cu(II) ions have

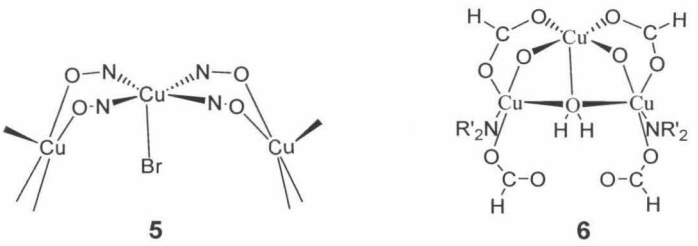

5 6

Figure 2. Structures of isosceles triangular Cu(II) model complexes: **5** taken from ref. 25; and **6** taken from ref. 28.

predominantly $d_{x^2-y^2}$ character. In the case of complex **5**, the observed strong antiferromagnetic coupling ($J = -448$ cm^{-1}) could be accounted for in terms of a superexchange mechanism operating via the Cu-N_2O_2-Cu linkage. However, such bridging networks are not coplanar, which should diminish the overlap between the magnetic orbitals. Thus, the unusual large spin exchange interaction in this complex was suggested to involve the electronic structure of the bridging ligand with a σ-orbital exchange pathway, which is independent of the angles between the basal planes of Cu(II) ions. On the other hand, the noncoplanarity of the mixed-bridge system in complex **6** results in a ferromagnetic exchange interaction of ~ 26 cm^{-1} between the central and terminal Cu(II) ions, while the exchange coupling constant between the terminal copper ions is ~ 0 cm^{-1}. Based on the results of a SCF-CI calculation of a dimeric model molecule constructed from the crystal structure of **6**, the exchange coupling changes from antiferromagnetic to ferromagnetic exchange coupling as the dihedral angle between the basal planes of central and terminal Cu(II) increases, i.e., from coplanar structure to folded structure. Similar results have also been obtained in a study of the ferromagnetism of binuclear copper clusters with small Cu-O-Cu angles (< 97.5°). Therefore, the magneto-structural correlation of polynuclear copper clusters

could be understood in terms of the exchange interactions of their binuclear building blocks, which are already quite well established experimentally and theoretically.[41]

A Cluster Model for the C-clusters of pMMO

Of the various cluster models discussed in the previous section, complex **6** probably offers the most likely comparison to the C-clusters in pMMO, particularly given the ligand types that are available for the copper ions in a protein environment. Nevertheless, we have undertaken EPR simulations on two of the ferromagnetically exchange-coupled trinuclear Cu(II) model complexes highlighted in the previous section, namely, **3** and **6,** to allow comparisons with the experimentally EPR spectra reported for these complexes. Unfortunately, no EPR spectrum was reported for complex **4**. Second, in our attempts to simulate the EPR spectrum observed for the copper clusters in oxidized pMMO, we consider both the trigonal bipyramidal coordination of the Cu(II) ion in complex **4** as well as the square pyramidal coordination in complex **3** and **6** in order to ascertain the effects of local coordination geometry on the EPR spectrum.

Obviously, in each case, the observed g values and directions must refer to the individual g-tensors of the three copper ions in the complex. The relative orientation between the g-tensors of the Cu(II) ions as well as the strength of ferromagnetic interactions vary with the geometrical disposition and the coordination geometry of the Cu(II) ions. The g-tensor orientation of individual Cu(II) ions for **3**, **4**, and **6** are depicted in Figure 3(a), (b), and (c), respectively. In each case, the principal axes of the local coordinate system for the individual Cu(II) ions are labeled as x*, y*, and z* for

the g-tensor. For either square pyramidal coordination in **3** and **6** or trigonal bipyramidal coordination in **4**, the equatorial plane defines the x*-y* plane whereas the z* axis lies along the apical (axial) direction. Although distortions from ideal coordination geometry might occur, these distortions will be neglected and the g-tensors are assumed to align with the idealized geometry.

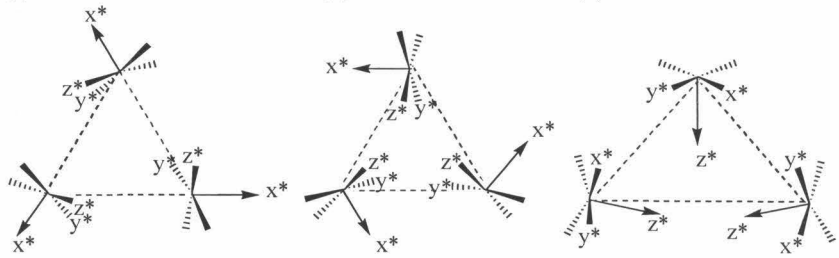

Figure 3. The orientations of the local g-tensors for compounds 3, 4, and 6. ((a), (b), and (c), respectively.)

The Spin Hamiltonian and Energy Levels of the Trinuclear Cu(II) Cluster

The spin Hamiltonian appropriate to describe the three interacting paramagnetic copper ions within a trinuclear Cu(II) complex can be written as the sum of the spin Hamiltonians for the individual spin centers and the spin Hamiltonian describing the exchange interaction (eq 1):

$$\begin{aligned} H = {} & \beta_e \cdot \mathbf{B} \cdot \mathbf{g}_A \cdot \mathbf{S}_A + \beta_e \cdot \mathbf{B} \cdot \mathbf{g}_B \cdot \mathbf{S}_B + \beta_e \cdot \mathbf{B} \cdot \mathbf{g}_C \cdot \mathbf{S}_C \\ & - 2 \cdot J_{AB} \cdot \mathbf{S}_A \cdot \mathbf{S}_B - 2 \cdot J_{BC} \cdot \mathbf{S}_B \cdot \mathbf{S}_C - 2 \cdot J_{CA} \cdot \mathbf{S}_C \cdot \mathbf{S}_A \\ & + \mathbf{S}_A \cdot \mathbf{D}_{AB} \cdot \mathbf{S}_B + \mathbf{S}_B \cdot \mathbf{D}_{BC} \cdot \mathbf{S}_C + \mathbf{S}_C \cdot \mathbf{D}_{CA} \cdot \mathbf{S}_A \end{aligned} \qquad (1)$$

Here, the three Cu(II) ions are labeled as A, B, and C, respectively. $\mathbf{g}_i$, J_{ij}, and $\mathbf{D}_{ij}$ denote the Zeeman g-tensor of spin centers i, the isotropic (or scalar) exchange interaction between interacting centers i and j, and zero field splitting tensor (anisotropic part of the

exchange and dipolar interaction) between the interacting spin centers i and j, respectively. For the trinuclear Cu(II) complex, each Cu(II) ion has S = 1/2 and I = 3/2. The overall zero-field splitting is taken into account when the total electron spin is ≥ 1. **D** will be used to describe the anisotropic part of the overall magnetic dipole-dipole interactions. Normally, two energy parameters, D and E, representing the axial and rhombic parameters, respectively, are used to describe the overall zero-field splitting. The D value refers to 3/2 of the $D_{||}$ or D_{zz} component in the D-tensor, and E is defined as $(D_{\perp} - D_{\perp'})/2$, or $(D_{xx} - D_{yy})/2$. Here, x, y, and z denote the principal axes of the D tensor in the plane and perpendicular to the triangular plane in the case of an equilateral complex.

The most common approximation is to consider the isotropic exchange as the leading term in the above equation. J_{ij} can be any value ranging from a few wave numbers to hundreds of wave numbers. For normal operating frequencies, the Zeeman energy is in the range of 0.3 – 1.2 cm^{-1}. Hyperfine interactions not formulated in the above equation are normally much smaller than the Zeeman energy, and the anisotropic exchange terms hardly exceed 1 cm^{-1}. In any case, these hyperfine interactions are typically averaged due to electron exchange narrowing for S > 1/2 systems. Therefore, we can first obtain the energies of the spin levels in the strong exchange limit. The predicted EPR spectrum will be just the superposition of the spectra observed for the different total spin states that are populated at the temperature of the experiment. The spectra can thus be described by one or more S spin Hamiltonians of the form:

$$H = \beta_e \mathbf{B} \cdot \mathbf{g}_S \cdot \mathbf{S} + \mathbf{S} \cdot \mathbf{D}_S \cdot \mathbf{S} + \sum_k \mathbf{I}^k \cdot \mathbf{A}_s^k \cdot \mathbf{S}, \qquad (2)$$

where $\mathbf{D}_s$ and $\mathbf{A}_s$ denote the zero-field splitting tensor and the hyperfine tensor of spin S.

The three Cu(II) ions in the cluster are ferromagnetically coupled to each other with $J \leq 20$ cm^{-1}.[9,10] It should be noted that the sign convention used throughout this report corresponds to positive values of J signifying ferromagnetic coupling. In this strong exchange coupling limit, we can label the spin levels of the cluster according to the eigenvalues of $\mathbf{S}^2$ and S_z. These operators commute with the isotropic part of eq 1. Since there are more than two spins in the system, the eigenstates of S_z and $\mathbf{S}^2$ are not uniquely determined by the spin quantum numbers M_s and S; thus, a number of additional quantum numbers are required according to the different "coupling schemes" of the interacting spins. Considering, for example, the simplest case of the coupling of three spins S_i (i = A, B, C), the total spin can be obtained by coupling spins S_A and S_B first to give $S_{AB} = S_A + S_B$ and then S_{AB} and S_C to give $S = S_{AB} + S_C$. The resulting states will be conveniently labeled using the eigenvalues of the commuting observables $\{\mathbf{S_A}^2, \mathbf{S_B}^2, \mathbf{S_{AB}}^2, \mathbf{S_C}^2, \mathbf{S}^2, S_z\}$, namely, $|S_A, S_B, S_{AB}, S_C, SM_s\rangle$. In the case of three Cu(II) spins 1/2, we obtain the quartet ground state and two excited doublets as the total spin states. The latter doublet states are degenerate in the case of an equilateral complex.

$$\begin{aligned} &\left|\tfrac{1}{2}\tfrac{1}{2}1\tfrac{1}{2},\tfrac{3}{2}\mathrm{M}\right\rangle \quad -\tfrac{3}{2} \leq M \leq \tfrac{3}{2} \cdots \text{quartet state;} \\ &\left|\tfrac{1}{2}\tfrac{1}{2}1\tfrac{1}{2},\tfrac{1}{2}\mathrm{M}\right\rangle \quad -\tfrac{1}{2} \leq M \leq \tfrac{1}{2} \cdots \text{doublet state;} \\ &\left|\tfrac{1}{2}\tfrac{1}{2}0\tfrac{1}{2},\tfrac{1}{2}\mathrm{M}\right\rangle \quad -\tfrac{1}{2} \leq M \leq \tfrac{1}{2} \cdots \text{doublet state.} \end{aligned} \tag{3}$$

The energy levels in the absence of the zero-field splitting (D = 0) and anisotropic contribution of the exchange interaction are shown in Figure 4(a), for the

case in which the magnetic field is parallel to the z direction. The other parameters used in the calculations are given in the figure caption.

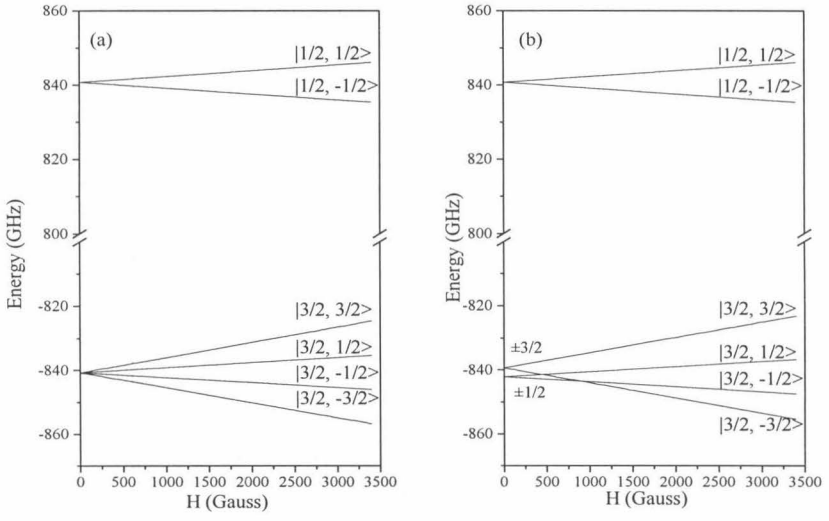

Figure 4. Field dependence of the energy levels calculated using eq 1 with g_x, g_y, and g_z = 2.0, 2.05, and 2.25 respectively; J = 200000 Gauss (~ 20 cm^{-1}). (a) D = 0 and (b) D = 500 Gauss. The energy levels are labeled by $|S, M_S>$.

To consider the effects of an axial zero-field splitting (E = 0), the energy levels in the case of a small D can also be calculated within the same formulation, since the zero-field splitting can be treated as a perturbation for |D| « |J|. The results for D = 500 Gauss are presented in Figure 4(b). The zero-field splitting is apparent at H = 0 and corresponds to the energy difference between the ±3/2 doublets (higher) and ±1/2 Kramers doublets (lower in energy). There are two places where energy level crossings occur: between $\left|\frac{3}{2},-\frac{3}{2}\right\rangle$ and $\left|\frac{3}{2},\frac{1}{2}\right\rangle$ at around 420 Gauss, and between $\left|\frac{3}{2},-\frac{3}{2}\right\rangle$ and $\left|\frac{3}{2},-\frac{1}{2}\right\rangle$ at around 880 Gauss. When the D-tensor is not axial, the eigenvectors cannot be labeled as mentioned above, since they become linear combinations of the basic vectors (eq 3). However, E is typically small.

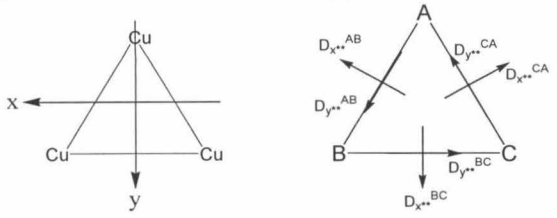

Figure 5. (a) Principal axes of the universal coordination system used in the EPR simulations. (b) Relative orientation of the D-tensors for each interacting Cu(II) pair in the trinuclear Cu(II) cluster complexes.

Each Cu(II) ion in the trinuclear cluster can be represented by a g-tensor. The principal axes of the universal reference frame throughout the course of the present study are shown in Figure 5(a). The local g-tensors are not necessary diagonal in this reference frame, but they are diagonal in their local coordinate systems (see Figure 3). Therefore, these local g-tensors have to be transformed to the reference frame. In the case of the zero-field splitting, the major contributions are from the magnetic dipolar interaction and the spin-orbit coupling between adjacent copper ions. Thus, the principal axes of the D-tensor of each interacting pair in the trinuclear cluster cannot be explicitly determined. In the present study, the relative orientation of the D-tensors is depicted in Figure 5(b), in which the z^{**}-axis of each D-tensor is chosen to be perpendicular to the Cu_3 plane. When the D-tensors are axial (E = 0), the tensors do not change (remains diagonal) upon rotation about their own z^{**}-axes, which are parallel to the z-axis.

It is well known that the g-tensor of exchange-coupled systems ($\tilde{g}_{S,S_{AB}}$) can be expressed as a linear combination of the local g-tensors.[42] For symmetric triads of S = 1/2 centers, the relations of the g-tensors is given below:

$$\tilde{g}_{3/2,1} = 1/3\ (\tilde{g}_A + \tilde{g}_B + \tilde{g}_C),$$

$$\tilde{g}_{1/2,1} = -1/3\ \tilde{g}_A + 2/3\ \tilde{g}_B + 2/3\ \tilde{g}_C, \qquad (4)$$

$\tilde{g}_{1/2,0} = \tilde{g}_A$.

Comparison of Simulated Spectra with EPR Observed for Models 3 and 6

The EPR spectrum of the equilateral triangular compound **3** reported at 4 K is shown in Figure 6. The signal is rather isotropic with three "deconvoluted" signals at g = 2.130, 2.116, and 2.089.[36] At higher temperatures, the spectrum consists of a sharp band centered at g = 2.114. Other similar trinuclear Cu(II) model complexes also exhibit a rather sharp and isotropic signal (linewidth ≤ 150 G) as a result of exchange narrowing.[35,38] The reported g-value ranges from 2.10 to 2.12 and was found to be almost constant from 4K to room temperature. The zero-field splitting of the quartet state was found to be zero or very small. Typically, a square pyramidal geometry Cu(II) center exhibits a g-tensor of $g_{\|}$ (~2.25) > $g_{\perp}$ (~2.05), similar to that of a type 2 copper site. The local $g^*_{x,y,z}$ chosen for **3** that describe the spectrum best are 2.05,

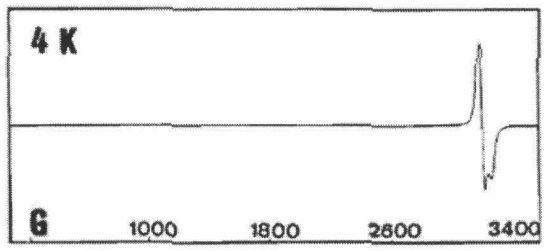

Figure 6. EPR spectrum of compound **3** at 4 K (reproduced from Figure 2 in ref. 36).

Scheme 1. The g-tensors for **3**.

$$\tilde{g}_A = \begin{bmatrix} 2.1659 & 0.0669 & -0.0726 \\ & 2.0886 & -0.0419 \\ & & 2.0955 \end{bmatrix}$$

$$\tilde{g}_B = \begin{bmatrix} 2.1659 & -0.0669 & 0.0726 \\ & 2.0886 & -0.0419 \\ & & 2.0955 \end{bmatrix} \qquad \tilde{g}_C = \begin{bmatrix} 2.05 & 0.0 & 0 \\ & 2.2045 & 0.0839 \\ & & 2.0955 \end{bmatrix}$$

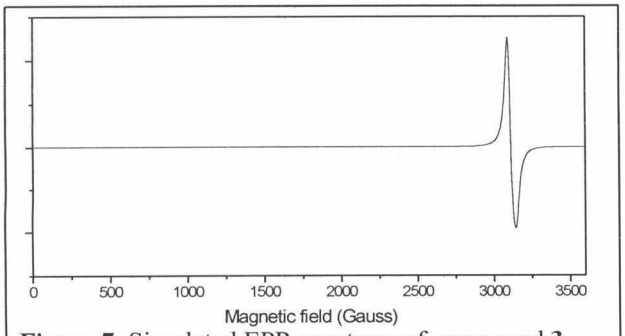

Figure 7. Simulated EPR spectrum of compound **3** using the parameters listed in **Scheme 1**.

2.05, 2.25. These $\tilde{g}$*'s were transformed to the universal reference frame, and the resultant tensor sets of **3** used in the simulations are listed in **Scheme 1**. The EPR spectrum simulated without considering the zero-field splitting is shown in Figure 7, which matches the experimental data quite well with a resultant effective g-value of 2.116. However, the signal at higher field (g~2.09) is not well resolved from the rest of the spectrum in the simulations. When certain linewidth anisotropy is introduced, this higher field feature could be resolved, reproducing the observed spectrum shown in Figure 6 (data not shown).

Similarly, the EPR spectra of **6** were simulated based on the structural and exchange coupling information provided. The local g-tensors used for the individual Cu(II) ions were also (2.05, 2.05, 2.25). The g-tensors and D-tensors, which were transformed to the universal reference frame and used in simulating the EPR signal of **6,** are listed in **Scheme 2,** and the results of the simulation are shown in Figure 8. Because of the large zero-field splitting (D ~ 1.4 cm^{-1} and E = 0.075), the calculated spectrum of **6** is composed of a major signal at g ~ 4.07 and a minor signal at (g ~ 2.04), as expected for a quartet state with a sufficiently large D. The experimental spectrum is not shown here, as it is

Scheme 2. EPR simulation parameters for **6** . The unit for D-tensors is gauss.

$$\tilde{g}_A = \begin{bmatrix} 2.05 & 0.0 & 0.0 \\ & 2.25 & 0.0 \\ & & 2.05 \end{bmatrix}$$

$$\tilde{D}_{AB} = \begin{bmatrix} -12022 & 2245.0 & 0 \\ & -10280 & 0 \\ & & 22302 \end{bmatrix} \qquad \tilde{D}_{CA} = \begin{bmatrix} -12022 & -2245.0 & 0 \\ & -10280 & 0 \\ & & 22302 \end{bmatrix}$$

$$\tilde{g}_B = \begin{bmatrix} 2.2405 & 0.0426 & 0.0 \\ & 2.0595 & 0.0 \\ & & 2.05 \end{bmatrix} \qquad \tilde{g}_C = \begin{bmatrix} 2.2405 & -0.0426 & 0.0 \\ & 2.0595 & 0.0 \\ & & 2.05 \end{bmatrix}$$

$J_{AB} = J_{CA} = 270000$ G; $J_{BC} = 0$.

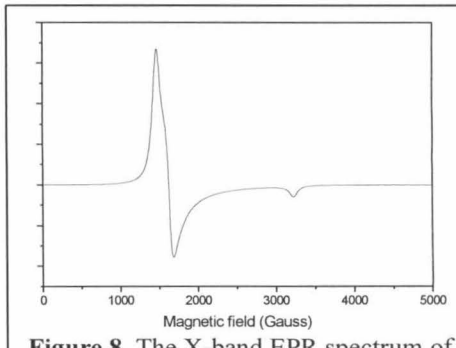

Figure 8. The X-band EPR spectrum of complex **6** simulated within the framework of the spin Hamiltonian

complicated and compromised by intermolecular effects.[43] The inclusion of such effects in the spectral simulation of compound **6** would be beyond the scope of this study.

EPR signals associated with the oxidized E- and C-clusters of pMMO

The EPR signal associated with the oxidized C-clusters and E-clusters was first reported by Nguyen et al.[9] Unlike EPR signals from type 1 or type 2 copper sites, this signal could not be saturated even at relatively high microwave powers. The spectrum in Figure 9(a) was obtained by fully oxidizing all the copper sites in purified pMMO with ferricyanide. When the pMMO is oxidized in this manner, the resultant ferrocyanide forms adducts with two of the E-clusters, each involving a ferrocyanide anion and one of the oxidized E-clusters located on the exposed domains of the protein.[13] Thus, the observed spectrum is expected to be even more heterogeneous than the composite

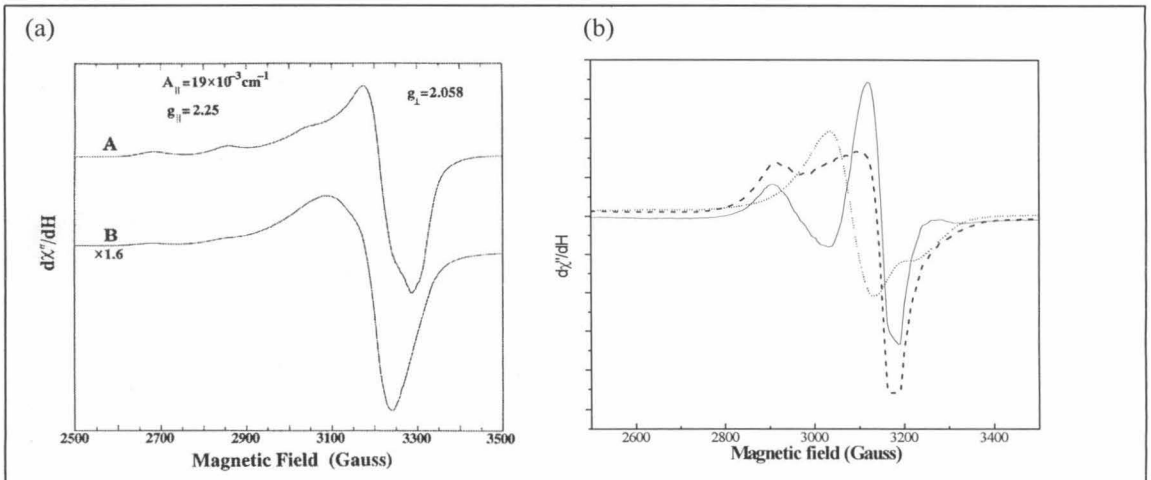

Figure 9. (a) The EPR spectra of oxidized membrane fractions from *M. capsulatus* (Bath) cells. **A**: Spectrum obtained with microwave power of 0.2 mW (data taken from Figure 3 in ref. 9); **B**: microwave power 40 mW (data taken from Figure 3 in ref. 9). (b) EPR signal of the C-clusters at g ~ 2.1 (solid line) obtained when the ferrocyanide-Cu(II) adduct contribution (dotted line) was subtracted from the spectrum of the fully oxidized pMMO (dashed line). See text for detail (taken from Figure 3-3 in ref. 13).

spectrum from the five clusters without adduct formation, as there is no reason to assume that the two C-clusters and three E-clusters are similar in structure, ligand geometry, and exchange interaction to begin with. On the other hand, it is relatively straightforward to assign the relatively broad but nearly isotropic signal at g ~ 2.1 to the $-1/2 \rightarrow 1/2$ transition within the S = 3/2 quartet manifold of a trinuclear Cu(II) cluster (Figure 4(b)). As expected, only about 40% of the EPR intensity anticipated from the number of oxidized copper centers was observed based on EPR spin count (although all the copper ions are oxidized). For a sufficiently large D, the $-3/2 \rightarrow -1/2$ and $1/2 \rightarrow 3/2$ transitions are strongly anisotropic and become part of the background. Differences in the g, D, and E (if the clusters depart from equilateral symmetry) no doubt contribute to the breadth of the EPR spectrum and the smearing out of the background.

More recently, this laboratory has used a series of chemical (EDTA and ferricyanide) and proteolytic treatment on the pMMO to distinguish different copper sites.[13] It is now clear that the copper sites are distributed within the soluble domain and the "buried" domain. Remnants of a non-specific copper-ferrocyanide adduct can be subtracted away from an EPR spectrum observed following exhaustive proteolytic and ferricyanide treatment on pMMO membranes, thereby obtaining a spectrum that can be ascribed to the oxidized C-clusters deeply buried within the protein-membrane complex (Figure 9(b)).[13] The signal for these oxidized copper ions is centered near $g \approx 2.1$, as expected for a ferromagnetically coupled trinuclear Cu(II) clusters, but it also contains a positive feature at g = 2.24 to lower magnetic fields and a weak negative feature around 1.95 toward higher fields. It is this spectrum that we have assigned to the oxidized C-

clusters of pMMO, and in the following EPR spectral simulations, we shall be comparing the results of the computer simulations to this signal.

Simulations of the pMMO Spectrum

In this section, we present the results of our efforts to simulate the EPR signals for the oxidized C- and E-clusters of pMMO. Calculations on equilateral clusters will first be performed, and the local coordination geometry of the copper ions and their relative geometrical disposition within the cluster will be taken to be similar to that in model complexes **3** and **4**. Deviations from the symmetric triad will be then considered, including both the isosceles arrangement and the general triad. Compound **6** is representative of an isosceles triangular model for a trinuclear cluster, and our simulations will be built on this model. The calculations will include variations over a range of zero-field splitting (D) in the case of equilateral triad, but the effects of E, in addition to D, will also be explored in the case of the less symmetric clusters. Finally, we conclude with a simulation of the EPR signal for the ferrocyanide-$Cu(II)_3$ adduct.

Equilateral Clusters

Figure 10 summarizes the results of our EPR simulations of the cluster signal in pMMO for equilateral clusters. These calculations were performed using the g-tensor arrangements derived from the coordination geometry of **3** and **4** and the spin Hamiltonian parameters (J and D) previously reported from the magnetization measurements.[9] From the temperature dependence of the magnetic moment for the fully oxidized pMMO sample, Nguyen et al. have deduced estimates of 15 – 20 cm^{-1} and ≤

0.05 cm^{-1} (531 Gauss) for the exchange interaction J and the axial zero-field splitting D, respectively.[9]

Scheme 3 lists the transformed local g-tensors ($g^*_{x,y,z}$) used for each of the three Cu(II) ions in the cluster, and the interspin D-tensors between pairs of Cu(II) ions, for the two coordination geometries. These local g-tensors differ in a minor way from the original sets reported for complex **3** and **4**, as some of the values were adjusted slightly to improve the fit between the simulated and the experimental spectrum. Even though various g-values could be chosen to fit the EPR spectrum of the C-clusters, the degree of variation in the coordination geometry at the individual copper ion places a limit on the local g-tensor (diagonal in local coordinate system).

Scheme 3. The g-tensors for EPR simulations of pMMO based on the structures of **3** and **4** are shown in **a** and **b**, respectively. The D-tensors for the case of D = 531 G are also listed.

a

$$\tilde{g}_A = \begin{bmatrix} 2.1534 & 0.0885 & -0.0726 \\ & 2.0511 & -0.0419 \\ & & 2.0955 \end{bmatrix}$$

$$\tilde{D}_{AB} = \tilde{D}_{BC} = \tilde{D}_{CA} = \begin{bmatrix} -354 & 0 & 0 \\ & -354 & 0 \\ & & 708 \end{bmatrix}$$

$$\tilde{g}_B = \begin{bmatrix} 2.1534 & -0.0885 & 0.0726 \\ & 2.0511 & -0.0419 \\ & & 2.0955 \end{bmatrix} \qquad \tilde{g}_C = \begin{bmatrix} 2.00 & 0.0885 & 0 \\ & 2.2045 & 0.0839 \\ & & 2.0955 \end{bmatrix}$$

b

$$\tilde{g}_A = \begin{bmatrix} 2.20 & 0.0 & 0.0 \\ & 2.0401 & -0.0566 \\ & & 2.1799 \end{bmatrix}$$

$$\tilde{D}_{AB} = \tilde{D}_{BC} = \tilde{D}_{CA} = \begin{bmatrix} -354 & 0 & 0 \\ & -354 & 0 \\ & & 708 \end{bmatrix}$$

$$\tilde{g}_B = \begin{bmatrix} 2.08 & -0.0693 & 0.0491 \\ & 2.16 & 0.0283 \\ & & 2.1799 \end{bmatrix} \qquad \tilde{g}_C = \begin{bmatrix} 2.08 & 0.0693 & -0.0491 \\ & 2.16 & 0.0283 \\ & & 2.1799 \end{bmatrix}$$

For a symmetric triad, $\tilde{D}_S = \frac{1}{6}(\tilde{D}_{AB} + \tilde{D}_{BC} + \tilde{D}_{CA})$, so $D_{\|} = D_{zz} = 354$ Gauss for a D of 531 Gauss or 0.05 cm^{-1} (D= 3/2 $D_{\|}$ or 3/2 D_{zz}). To yield a D = 531 Gauss in $\tilde{D}_S$, $D^{zz}_{AB} = D^{zz}_{BC} = D^{zz}_{CA} = 708$ G so that $D_{\|} = \frac{1}{6}(708\times3) = 354$ Gauss and D = 3/2 $D_{\|}$ = 531 G.

Although we have assumed that the exchange coupling constant between pairs of Cu(II) ions in the cluster is 20 cm^{-1}, the outcome of the simulations is not sensitive to the

exact value of J, so long as J is sufficiently large that the strong exchange limit is obtained. For ferromagnetic coupling, the energy levels of the ground quartet state are insensitive to the magnitude of J within this limit.

In the strong exchange limit, only the transitions within the ground quartet states are thermally accessible at low temperatures (see Figure 4). In the presence of zero-field splitting, the details of the observed EPR signal are strongly dependent on the relative

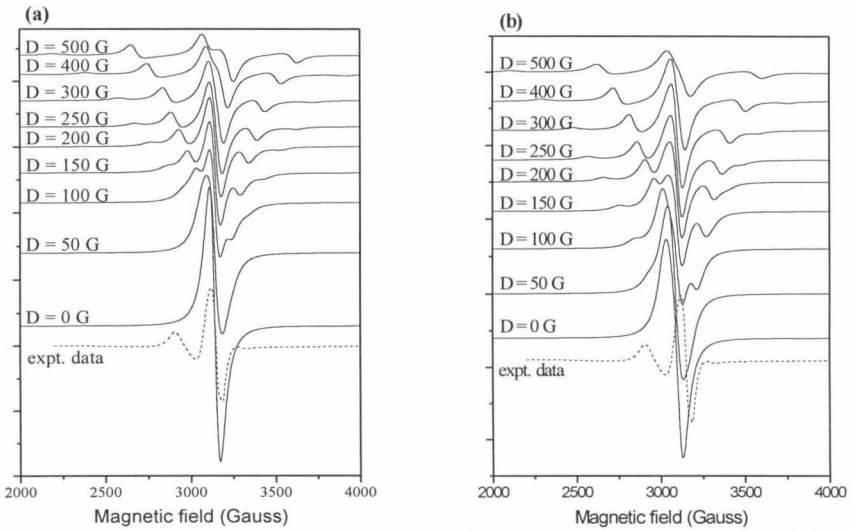

Figure 10. The simulated EPR signal of the C-clusters in pMMO. Simulations (a) and (b) are based on the equilateral structural model of compounds **3** and **4**, respectively. The g-tensors are listed in **Scheme 3**. For comparison, the "experimental" spectrum is shown as the dashed line.

magnitude of the zero-field splitting and the frequency of the microwaves used to excite the spins in the spectrometer. When $g\beta H \gg D$, the spectrum is centered about $g \sim 2$, although the resonance fields for the $-3/2 \rightarrow -1/2$ and $1/2 \rightarrow 3/2$ transitions are not coincident with the $-1/2 \rightarrow 1/2$ transition. As D becomes progressively larger in magnitude, the $-3/2 \rightarrow -1/2$ and $1/2 \rightarrow 3/2$ transitions begin to appear to lower and higher resonance fields. For sufficiently large D's, these transitions become highly anisotropic and often become part of the baseline or background. For even larger D's,

only the transitions within the $-1/2 \rightarrow 1/2$ Kramer's doublet are observable and the spectrum centered at $g \sim 2$ becomes progressively heterogeneously broadened. Additional features are often distinguishable at lower g's, and higher g's as well. For $D \gg g\beta H$, the spectrum for the $-1/2 \rightarrow 1/2$ Kramer's doublet degenerates into that of the quartet state depicted in Figure 8, with the overall integrated intensity associated with the entire Kramer's doublet accounting for $0.4 \times 3 = 1.2$ copper ions per cluster based on EPR spin count.

Variations of the trinuclear cluster EPR spectrum with axial zero-field splitting D from D = 0 through 500 Gauss are illustrated in Figure 10 for the two equilateral representative coordination geometries noted earlier. The C-cluster signal from pMMO (dotted line in Figure 9(b)) is included with the simulated spectra for comparison in each case. While direct comparisons of the intensities of the simulated spectra are meaningful, the observed C-cluster signal for pMMO has been scaled to fit into the Figure and absolute experimental intensities are not implied.

The relative contributions of the three transitions to the composite spectrum of the quartet state are illustrated in Figure 11. It is evident that for small D values, of the order of 50 Gauss, the $-3/2 \rightarrow -1/2$ and $1/2 \rightarrow 3/2$ transitions contribute mainly to the center of the EPR signal, resulting in an overall signal that remains relatively isotropic but with a larger linewidth. For a cluster with three Cu(II) ions with coordination geometry similar to that in the model complex **3**, the center of these EPR spectra can be readily explained by $\tilde{g}_{3/2,1}$ in eq 4, with an effective g value corresponding to $g_{avg} \sim 2.1$ (= 1/3 (Tr $\tilde{g}^*$)). In the case of model **4**, all the composite spectrum is shifted to

somewhat lower fields, corresponding to the average g value of 2.14 for trigonal bipyramidal coordination.

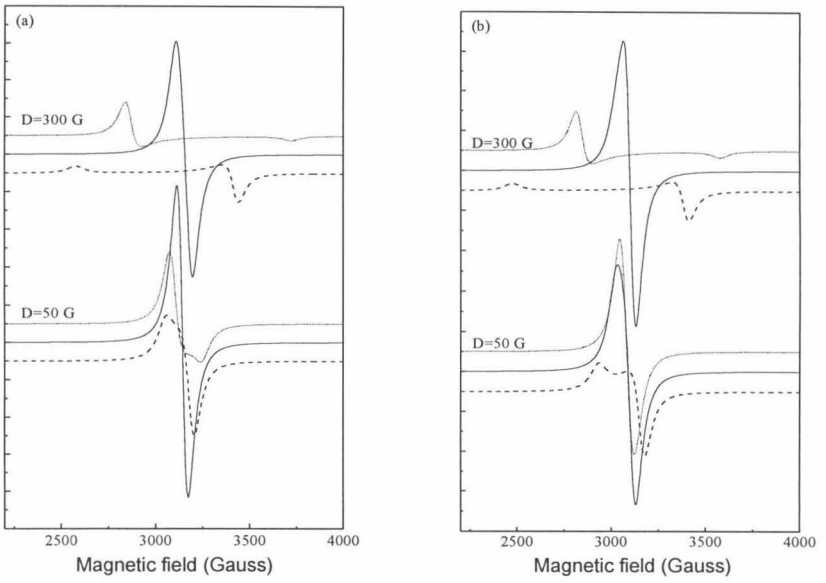

Figure 11. Relative contributions of the three transitions to the composite spectrum of the quartet state. In each panel, dashed line, solid line, and dotted line represent the $-3/2 \rightarrow -1/2$, $-1/2 \rightarrow 1/2$, and $1/2 \rightarrow 3/2$ transitions, respectively. The simulations of (a) and (b) are based on the structural model of compounds **3** and **4**, respectively. The g-tensors are listed in **Scheme 3**.

In the case of fully oxidized pMMO, we expect the presence of the five trinuclear copper clusters to complicate the composite further by "g" dispersion and "D" dispersion. In addition, we need to include "g" and "D" strain in the spectrum for each cluster. Spectral simulations including a gaussian distribution of D values of the order of 10% - 20% result primarily in the broadening of the composite spectrum without altering the overall spectral features (data not shown).

Deviation from equilateral clusters

In general, there are three possibilities of triangular arrangement for a trinuclear cluster: equilateral, isosceles, and the general triad. Since each spin interacts with the

adjacent ones, the strength of these interactions determines the magnetic geometry of the triad. In the most general case when no two J_{ij} values are equal, then states with the same S value can be admixed, and the corresponding g-tensors are given by

$$\tilde{g}_{3/2,1} = 1/3\,(\tilde{g}_A + \tilde{g}_B + \tilde{g}_C),$$

$$\tilde{g}_{1/2,1} = -(1/3 - 4/3\sin^2\lambda)\,\tilde{g}_A + 2(1/3 - 1/3\sin^2\lambda - 1/\sqrt{3}\sin\lambda\cos\lambda)\,\tilde{g}_B + 2(1/3 - 1/3\sin^2\lambda + 1/\sqrt{3}\sin\lambda\cos\lambda)\,\tilde{g}_C, \quad (5)$$

$$\tilde{g}_{1/2,0} = (1 - 4/3\sin^2\lambda)\,\tilde{g}_A + 2\,(1/3\sin^2\lambda + 1/\sqrt{3}\sin\lambda\cos\lambda)\,\tilde{g}_B + 2\,(1/3\sin^2\lambda - 1/\sqrt{3}\sin\lambda\cos\lambda)\,\tilde{g}_C,$$

$$\lambda = 1/2\tan^{-1}[3^{1/2}(J_{AB} - J_{AC})/(2J_{BC} - J_{AC} - J_{AB})].$$

Thus, the transitions within the two doublet states vary with the magnetic geometry of the triad. Note, however, that $\lambda = 0°$ for both the equilateral and isosceles magnetic geometry, and the result for the symmetric triad is obtained.

For a ferromagnetically coupled trinuclear cluster in the strong exchange limit, the observed EPR spectra are dominated by the transition within the quartet states, namely $\tilde{g}_{3/2,1}$, and the observed g-values for the quartet do not vary with the shape of the triangle. The contributions from the two

Scheme 4. The g-tensors for EPR simulations of pMMO based on the structures of **6**. The D-tensors for the case of D = 531 G are also listed.

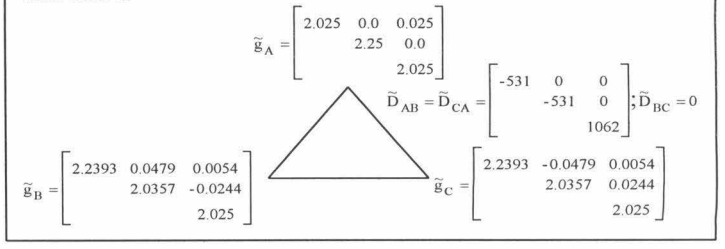

doublet states can only be observed at rather elevated temperature (depending on the magnitude of the exchange coupling).

Compound **6** is representative of an isosceles triangular model for the trinuclear clusters in pMMO. The local g-tensors ($g^*_{x,y,z}$) used for each of the three Cu(II) ions in the cluster and the interspin D-tensors between pairs of Cu(II) ions are listed in **Scheme 4**. In this case, the exchange interactions between the terminal copper ions are negligible;[28,40] accordingly, both J_{BC} and D_{BC} were set to zero in the simulations. Spectral simulation results obtained with the axial zero-field splitting D varying from D = 0 through 500 Gauss are illustrated in Figure 12(a). Here, we find that the "central"

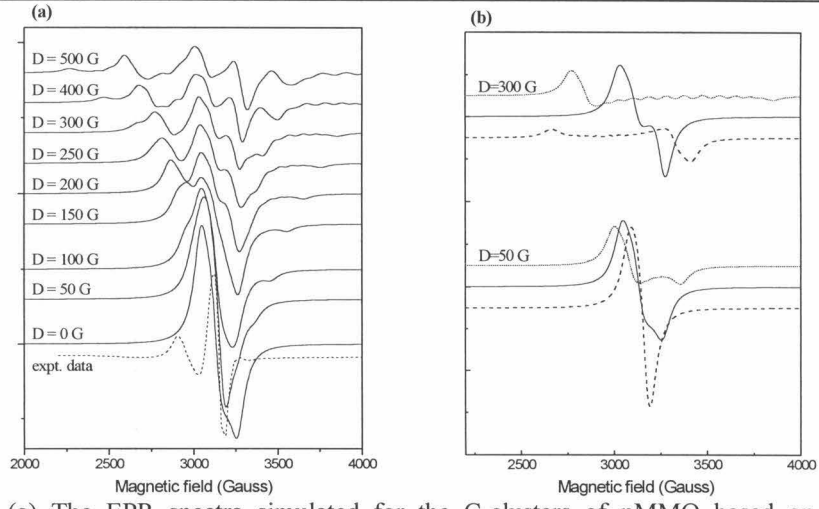

Figure 12. (a) The EPR spectra simulated for the C-clusters of pMMO based on the isosceles structural model of compound **6**. Details of the spin Hamiltonian are given in **Scheme 4**. For comparison, the "experimental" spectrum is shown as the dashed line. (b) Contributions of the three transitions, $-3/2 \rightarrow -1/2$ (dashed line), $-1/2 \rightarrow 1/2$ (solid line), and $1/2 \rightarrow 3/2$ (dotted line) within the quartet state are depicted separately in this panel.

feature in the spectrum is significantly more sensitive to D than those seen in Figure 10, so that the spectrum exhibits greater anisotropy and weaker intensity. In Figure 12(b), the contribution of the three transitions within the quartet state are shown for D = 50 and 300 G. It is clear that the resonance fields for the $-3/2 \rightarrow -1/2$ and $1/2 \rightarrow 3/2$ transitions

move away from the g = 2 region and manifest themselves towards lower and higher magnetic fields even for relatively smaller D's, as compared to the case of the equilateral triangular clusters.

The general triad

As the triangular arrangement of a trinuclear cluster departs from the symmetric triad, the rhombic zero-field splitting becomes important. In order to ascertain the effects of the rhombic zero-field splitting parameter E on the EPR signal of the trinuclear cluster, non-zero E values were introduced in the EPR simulations of the cluster signal based on the g-tensors of **6** (**Scheme 4**). Some simulations are presented in Figure 13 for the representative coordination geometries employed in this study, and varying D over the range of 50 – 500 Gauss, and E/D over the range of 0.01 to 0.3. As expected, the cluster spectra do not exhibit significant changes for small D values and small E/D's. However, for sufficiently large D's, the inclusion of a non-zero E leads to the smearing out of the features arising from $-3/2 \rightarrow -1/2$, and $1/2 \rightarrow 3/2$ transitions. The $-1/2 \rightarrow 1/2$ transition giving rise to the central feature of the spectra remains relatively unchanged even at relatively large D and E values although the anisotropy of this signal is increased with increasing E.

On the basis of these simulations, it is clear that the C-cluster signal from pMMO could be reproduced by an equilateral of three ferromagnetically coupled square pyramidal Cu(II) ions with an overall zero-field splitting of the order of 50 – 300 Gauss. There is no reason to expect that the two C-clusters are perfectly symmetric triads, but

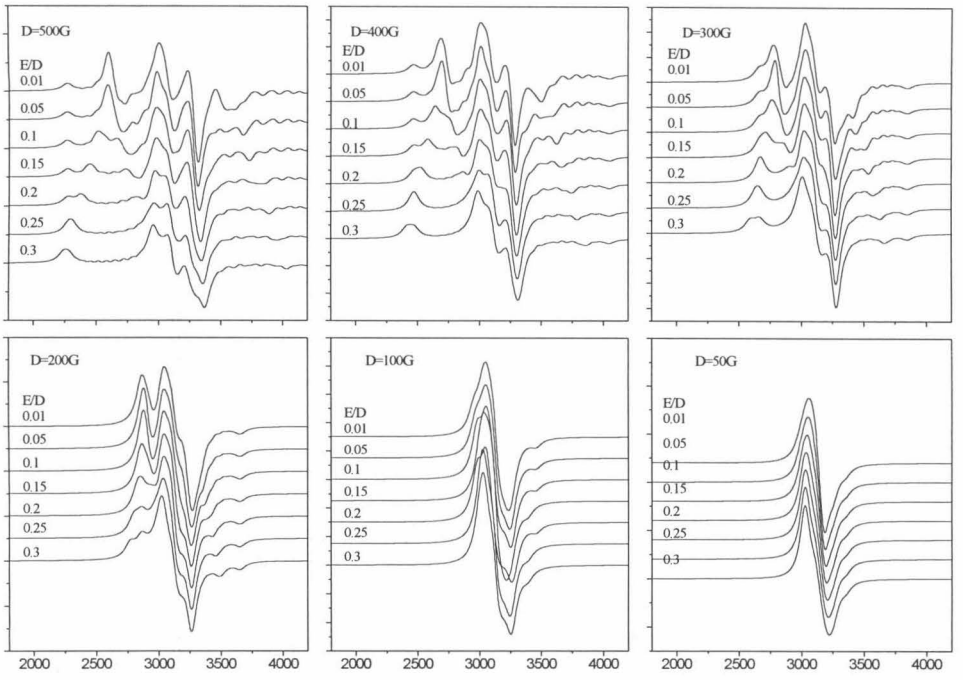

Figure 13. The effects of a rhombic distortion in the zero-field splitting on the simulated spectrum of the C-clusters for pMMO based on the isosceles structural model of compound **6** at different axial zero-fielding splittings ($50 \leq D \leq 500$ Gauss).

large deviations from equilateral seem rather unlikely. Since an intensity anomaly is observed when the intensity of the EPR of the copper ions in the fully oxidized pMMO is compared with the intensity expected by the number of Cu(II) ions and EPR spin count, it follows that several of the clusters, most likely the C-clusters, have D values at the higher end of the 50 – 300 Gauss range. At this juncture, we can say little about the E-clusters, except that the D values might be smaller for them.

The ferrocyanide-Cu_3 adduct

As mentioned earlier, it is possible to oxidize all the copper ions in pMMO by the addition of ferricyanide to the protein. At essentially stoichiometric proportions of ferricyanide to protein, 2:1 ferrocyanide-pMMO adducts are formed.[10,13] Evidence for

the 2:1 adduct has come from Fe and Cu K-edge and associated EXAFS,[13] and the designation of the iron oxidation state as Fe(II) from IR spectroscopy of the coordinated cyanides.[44] The EPR of this limiting ferrocyanide-Cu_3 adduct gave a strong isotropic signal at g = 2.14, in agreement with related synthetic model compounds.[13] Note that in this limiting species, only the copper ion directly coordinated to the ferrocyanide is oxidized, the remaining copper ions staying reduced and therefore not contributing to the EPR signal observed. Addition of increasing amounts of ferricyanide leads to progressively increased oxidation of the copper ions in the protein, until all 15 copper ions are oxidized eventually. Presumably, the oxidation of the protein copper ions occur via an outer sphere electron transfer mechanism to ferricyanide in solution, as the stoichiometry of the adduct remains unchanged, namely 1 Fe to 8 Cu, or 2 Fe to 15 Cu.

The initial ferrocyanide-Cu_3 adducts with its isotropic EPR at g = 2.14 is consistent with formation of the heteronuclear adduct Fe(II)-CN-Cu(II)Cu(I)Cu(I), as obtained by coordination of a ferricyanide to one of the Cu(I) ions within a reduced E-cluster followed by transfer of an electron from the Cu(I) to the $Fe(CN)_6^{3-}$. With further oxidation of the E-cluster, the isotropic EPR signal shifts to a g of 2.12, as expected with the conversion of the heteronuclear adduct from Fe(II)-CN-Cu(II)Cu(I)Cu(I) to Fe(II)-CN-Cu(II)Cu(II)Cu(II). To verify this expectation, we have also simulated the EPR spectrum of the Fe(II)-CN-Cu(II)Cu(II)Cu(II) complex in the same manner as before, simply by replacing the g-tensor for one of the copper ions. For this calculation, we chose the tensor set given by **Scheme 3a** and replaced one of the g-tensors with an isotropic g set at 2.14. The simulated spectrum (bold line) for this adduct is shown in Figure 14. Aside from the fact that the calculated spectrum is more anisotropic, and the

g value is somewhat higher, this spectrum shows general resemblance to the spectra simulated earlier for the symmetric triad with D = 0. Agreement between the simulated spectrum and the experimental spectrum obtained from incubation of the pMMO with 0.5 mM ferricyanide (solid line in Figure 14) is also remarkable, considering that the experimental spectrum most certainly includes contribution from an oxidized E-cluster with a slightly lower g-value.

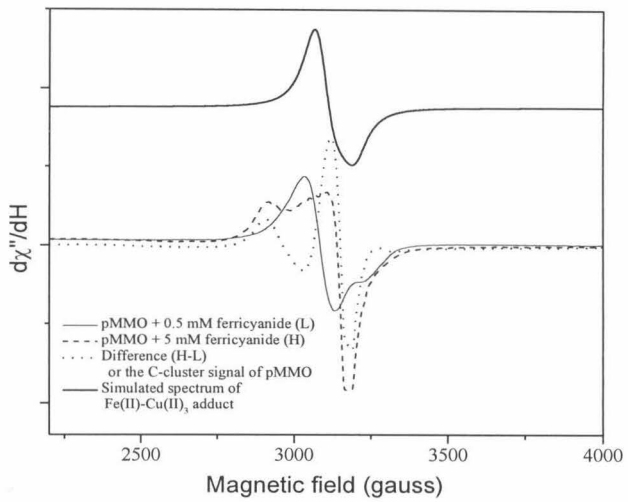

Figure 14. The simulated EPR spectrum of the ferrocyanide-$Cu(II)_3$ adduct (bold line). Details of the simulation are described in the text. Shown for comparison are the EPR spectra of pMMO oxidized by 0.5 mM ferricyanide (solid line) and 5 mM ferricyanide (dashed line). The C-cluster signal of pMMO is also included for reference (dotted line).

On the other hand, upon incubation of the pMMO with higher concentration of ferricyanide (5 mM), a signal at g = 2.24 appears (dashed spectrum). Under these conditions, the C-clusters should become oxidized, and we have tentatively assigned this feature to these clusters as we have done earlier.

Nuclear hyperfine and superhyperfine interactions

Due to the fast electron exchange among the copper ions within the cluster, we do not anticipate to observe nuclear hyperfine or superhyperfine interactions for a trinuclear Cu(II) cluster, and in fact, none has been observed. Such hyperfine

interactions have only been seen in isolated type 2 Cu(II) species derived from the clusters with EPR signals that are readily saturable at moderate microwave powers.[9] Nevertheless, it would be useful to consider the effect of these hyperfine interactions on the EPR spectrum should the electron exchange be sufficiently slow to allow these interactions to manifest themselves.

Copper hyperfine interaction – We can assume that the nuclear hyperfine interaction at each copper nucleus within the cluster to be similar to that of an "isolated" type 2 copper ion. That is, there is no electron spin density redistribution upon the formation of the trinuclear copper cluster. The overall hyperfine interactions of the trinuclear copper cluster can be calculated from the hyperfine coupling tensors $\widetilde{A}^*$ of the three type 2 copper ions ($A_{\|} \sim 180 \times 10^{-4}$ cm^{-1}, $A_{\perp} \sim 32 \times 10^{-4}$ cm^{-1}). If these $\widetilde{A}^*$ tensors have the same principal axes as the g-tensors (Figure 3), they can be transformed to the universal reference frame similarly, based on the structure assumed for the cluster. If we let $\widetilde{A}^1$, $\widetilde{A}^2$, and $\widetilde{A}^3$ be the single ion hyperfine tensors, the hyperfine tensors $\widetilde{A}^i_{3/2}$ for the coupled trinuclear copper can be defined as $\widetilde{A}^1_{3/2} = \frac{1}{3}\widetilde{A}^1, \widetilde{A}^2_{3/2} = \frac{1}{3}\widetilde{A}^2$, and $\widetilde{A}^3_{3/2} = \frac{1}{3}\widetilde{A}^3$ for the quartet state.

The overall spin Hamiltonian of the nuclear hyperfine interactions is:

$$H_{SI} = \sum_i \mathbf{I}^i \cdot \widetilde{A}^i_S \cdot \mathbf{S}, \qquad (6)$$

where $\mathbf{I}^i$ and $\widetilde{A}^i$ denotes nuclear spin and nuclear hyperfine tensor (from type 2 copper

site) for nucleus i, respectively, and $\mathbf{S} = S_A + S_B + S_C$ for the trinuclear copper cluster. The nuclear hyperfine interaction of each individual copper ion, say nucleus 1 and electron spin S_A, is expressed as $I^1 \cdot \tilde{A}^1 \cdot S_A$, while the interaction between I^1 and S_B or S_C is assumed to be negligible. Finally, in the coupled trinuclear system, the ^{63}Cu nuclear hyperfine interaction is determined by the projection of the nuclear hyperfine tensors of each individual ion on the total spin. In the limit where electron Zeeman interaction is dominant, we can rewrite the total spin Hamiltonian as

$$H = g\beta_e B \cdot M_s - g_n\beta_n \mathbf{B}^T_{\mathbf{hf,A}} \cdot \hat{\mathbf{I}}^1 - g_n\beta_n \mathbf{B}^T_{\mathbf{hf,B}} \cdot \hat{\mathbf{I}}^2 - g_n\beta_n \mathbf{B}^T_{\mathbf{hf,C}} \cdot \hat{\mathbf{I}}^3, \qquad (7)$$

where $\mathbf{B_{hf}}$ is the total magnetic field acts on the nuclear magnetic moment, or

$$\mathbf{B}_{\mathbf{hf,i}} = \frac{-M_s}{g_n\beta_n} \tilde{\mathbf{A}}^{iT} \cdot \mathbf{n} \qquad (8)$$

Here, $\tilde{\mathbf{A}}^{iT}$ is the transpose of A^i-tensor and $\mathbf{n}$ denotes the unit vector along $\mathbf{B}$. Therefore, the projection of the hyperfine field along $\mathbf{B}$ is proportional to $\mathbf{n}^T \cdot \tilde{\mathbf{A}}^i \cdot \mathbf{n}$, and the magnitude of the hyperfine interaction is proportional to $\left(\mathbf{n}^T \cdot \tilde{\mathbf{A}}^i \cdot \tilde{\mathbf{A}}^{iT} \cdot \mathbf{n}\right)^{1/2}$. By solving the spin Hamiltonian, the energy levels for this system are found to be

$$U_{M_S,M_I} = g\beta_e B M_S + \sum_i (\mathbf{n}^T \cdot \tilde{\mathbf{A}}^i \cdot \tilde{\mathbf{A}}^{iT} \cdot \mathbf{n})^{1/2} |M_S| M_I^i \qquad (9)$$

Thus, according to this analysis, one should expect relatively large ^{63}Cu and ^{65}Cu nuclear hyperfine splittings were it not for electron exchange.

Summary

Toward understanding the nature of the ferromagnetically coupled trinuclear Cu(II) clusters in oxidized pMMO and the EPR spectra associated with these clusters, we have undertaken a review of the model triangular Cu(II) clusters that have been synthesized and characterized in the literature. Among the over 100 trinuclear copper clusters (including linear clusters) that have been reported so far, only a few show ferromagnetic exchange coupling. Nevertheless, these complexes exhibit sufficient variation in local ligand coordination geometry and structural arrangements of the copper ions to allow us to build on these magneto-structural frameworks for the purpose of the present study. We find that it is possible to simulate the EPR observed for the C-cluster(s) of pMMO on the basis of an essentially symmetric triad of type 2 Cu(II) ions with an axial zero-field splitting of 50 – 300 Gauss. Unfortunately, at this juncture, we know much less about the E-clusters. However, the same formulation has also allowed us to simulate the EPR of the heteronuclear Fe(II)-CN-Cu(II)Cu(II)Cu(II) adducts that are formed upon incubution of the protein with controlled amounts of ferricyanide. The results are in apparently good agreement with experiment.

References

(1)Allendorf, M. D.; Spira, D. J.; Solomon, E. I. *Proc. Natl. Acad. Sci. U. S. A.* **1985**, *82*, 3063-3067.

(2)Cole, J. L.; Clark, P. A.; Solomon, E. I. *J. Am. Chem. Soc.* **1990**, *112*, 9534-9548.

(3)Cole, J. L.; Tan, G. O.; Yang, E. K.; Hodgson, K. O.; Solomon, E. I. *J. Am. Chem. Soc.* **1990**, *112*, 2243-2249.

(4)Sundaram, U. M.; Zhang, H. H.; Hedman, B.; Hodgson, K. O.; Solomon, E. I. *J. Am. Chem. Soc.* **1997**, *119*, 12525-12540.

(5)Zaitseva, I.; Zaitsev, V.; Card, G.; Moshkov, K.; Bax, B.; Ralph, A.; Lindley, P. *JBIC* **1996**, *1*, 15-23.

(6)Messerschmidt, A.; Ladenstein, R.; Huber, R.; Bolognesi, M.; Avigliano, L.; Petruzzelli, R.; Rossi, A.; Finazziagro, A. *J. Mol. Biol.* **1992**, *224*, 179-205.

(7)Messerschmidt, A.; Luecke, H.; Huber, R. *J. Mol. Biol.* **1993**, *230*, 997-1014.

(8)Solomon, E. I.; Sundaram, U. M.; Machonkin, T. E. *Chem. Rev.* **1996**, *96*, 2563-2605.

(9)Nguyen, H.-H. T.; Shiemke, A. K.; Jacobs, S. J.; Hales, B. J.; Lidstrom, M. E.; Chan, S. I. *J. Biol. Chem.* **1994**, *269*, 14995-15005.

(10)Nguyen, H.-H. T.; Nakagawa, K. H.; Hedman, B.; Elliott, S. J.; Lidstrom, M. E.; Hodgson, K. O.; Chan, S. I. *J. Am. Chem. Soc.* **1996**, *118*, 12766-12776.

(11)Nguyen, H. H.; Elliott, S. J.; Yip, J. H.; Chan, S. I. *J. Biol. Chem.* **1998**, *273*, 7957-66.

(12)Elliott, S. J.; Zhu, M.; Tso, L.; Nguyen, H.-H. T.; Yip, J. H.-K.; Chan, S. I. *J. Am. Chem. Soc.* **1997**, *119*, 9949-9955.

(13)Elliott, S. J.; California Institute of Technology: Pasadena, 2000.

(14)Kahn, O. *Angew. Chem. Int. Ed. Engl.* **1985**, *24*, 834-850.

(15)Miller, J. S.; Epstein, A. J. *Angew. Chem. Int. Ed. Engl.* **1994**, *33*, 385-415.

(16)Stumpf, H. O.; Ouahab, L.; Pei, Y.; Bergerat, P.; Kahn, O. *J. Am. Chem. Soc.* **1994**, *116*, 3866-3874.

(17)Beckett, R.; Hoskins, B. F. *J. Chem. Soc., Dalton Trans* **1972**, 291-295.

(18)Baral, S.; Chakravorty, A. *Inorg. Chim. Acta* **1980**, *39*, 1-8.

(19)Butcher, R. J.; O'Connor, C. J.; Sinn, E. *Inorg. Chem.* **1981**, *20*, 537-545.

(20)Hulsbergen, F. B.; tenHoedt, R. W. M.; Verschoor, G. C.; Reedijk, J.; Spek, A. L. *J. Chem. Soc., Dalton Trans.* **1983**, 539-545.

(21)Comarmond, J.; Dietrich, B.; Lehn, J. M.; R., L. *J. Chem. Soc., Chem. Commun.* **1985**, 74-76.

(22)Costes, J. P.; Dahan, F.; Laurent, J. P. *Inorg. Chem.* **1986**, *25*, 413-416.

(23)Kwiatkowski, M.; Kwiatkowski, E.; Olechnowicz, A.; Ho, D. M.; Deutsch, E. *Inorg. Chim. Acta* **1988**, *150*, 65-73.

(24)Agnus, Y.; Louis, R.; Metz, B.; Boudon, C.; Gisselbrecht, J. P.; Gross, M. *Inorg. Chem.* **1991**, *30*, 3155-3161.

(25)Chaudhuri, P.; Winter, M.; DellaVedova, B. P. C.; Bill, E.; Trautwein, A.; Gehring, S.; Fleischhauer, P.; Nuber, B.; Weiss, J. *Inorg. Chem.* **1991**, *30*, 2148-2157.

(26)Chaudhuri, P.; Karpenstein, I.; Winter, M.; Butzlaff, C.; Bill, E.; Trautwein, A. X.; Florke, U.; Haupt, H. J. *J. Chem. Soc., Chem. Commun.* **1992**, 321-322.

(27)Adams, H.; Bailey, N. A.; Dwyer, M. J. S.; Fenton, D. E.; Hellier, P. C.; Hempstead, P. D.; Latour, J. M. *J. Chem. Soc., Dalton Trans.* **1993**, 1207-1216.

(28)Gehring, S.; Fleischhauer, P.; Paulus, H.; Haase, W. *Inorg. Chem.* **1993**, *32*, 54-60.

(29)Meenakumari, S.; Tiwary, S. K.; Chakravarty, A. R. *Inorg. Chem* **1994**, *33*, 2085-2089.

(30)Cole, A.; Root, D.; Mukherjee, P.; Solomon, E.; Stack, T. *Science* **1996**, *273*, 1848-1850.

(31)Spiccia, L.; Graham, B.; Hearn, M. T. W.; Lazarev, G.; Moubaraki, B.; Murray, K. S.; Tiekink, E. R. T. *J. Chem. Soc., Dalton Trans.* **1997**, 4089-4097.

(32)Suh, M. P.; Han, M. Y.; Lee, J. H.; Min, K. S.; Hyeon, C. *J. Am. Chem. Soc.* **1998**, *120*, 3819-3829.

(33)Bernhardt, P. V.; Sharpe, P. C. *J. Chem. Soc., Dalton Trans.* **1998**, 1087-1088.

(34)Kodera, M.; Tachi, Y.; Kita, T.; Kobushi, H.; Sumi, Y.; Kano, K.; Shiro, M.; Koikawa, M.; Tokii, T.; Ohba, M.; Okawa, H. *Inorg. Chem.* **2000**, *39*, 226-234.

(35)Kolks, G.; Lippard, S. J.; Waszczak, J. V. *J. Am. Chem. Soc.* **1980**, *102*, 48324833.

(36)Escuer, A.; Vicente, R.; Penalba, E.; Solans, X.; Fonte-Bardia, M. *Inorg. Chem.* **1996**, *35*, 248-251.

(37)Springborg, J.; Glerup, J.; Sotofte, I. *Acta Chem. Scand.* **1997**, *51*, 832-838.

(38)Bazzicalupi, C.; Bencini, A.; Bencini, A.; Bianchi, A.; Corana, F.; Fusi, V.; Giorgi, C.; Paoli, P.; Paoletti, P.; Valtancoli, B.; Zanchini, C. *Inorg. Chem.* **1996**, *35*, 5540-5548.

(39)Girard, J. J.; Charlot, M. F.; Kahn, O. *Mol. Phys.* **1977**, *34*, 1063.

(40)Fleischhauer, P.; Gehring, S.; Saal, C.; Haase, W.; Tomkowicz, Z.; Zanchini, C.; Gatteschi, D.; Davidov, D.; Barra, A. L. *J. Magn. Magn. Mater.* **1996**, *159*, 166-174.

(41)Ruiz, E.; Alemany, P.; Alvarez, S.; Cano, J. *J. Am. Soc. Chem.* **1997**, *119*, 1297.

(42)Bencini, A.; Gatteschi, D. *EPR of exchange-coupled systems*; Springer: Berlin, 1990.

(43)Tomkowicz, Z.; Fleischhauer, P.; Haase, W.; Baran, M.; Szymczak, R.; Zaleski, A. J.; Jablonski, R. *J. Magn. Magn. Mater.* **1997**, *172*, 128-138.

(44)Nguyen, H.-H. T. ; California Institute of Technology: Pasadena, 1997.